Magma / Suspension Rheology

Stephan Kolzenburg, Oryaëlle Chevrel, Donald B Dingwell

MAGMA / SUSPENSION RHEOLOGY

Stephan Kolzenburg 1,2,3, Magdalena O. Chevrel 4, Donald B. Dingwell 2

1. Department of Geology
University at Buffalo
126 Cooke Hall
Buffalo, NY 14260-4130, U.S.A.

2. Department of Earth and Environmental Sciences
Ludwig-Maximilians-University Munich
Theresienstr. 41 / III
80333, Munich, Germany

2. Department of Earth and Planetary Sciences
McGill University
3450 University Street
Montreal, H3A 0E8, Quebec, Canada

4. Laboratoire Magmas et Volcans,
Université Clermont Auvergne, CNRS, IRD, OPGC,
6 Avenue Blaise Pascal
f-63000, Clermont-Ferrand, France

stephank@buffalo.edu; oryaelle.chevrel@ird.fr; dingwell@lmu.de

1. THEORETICAL CONSIDERATIONS

When considering the rheology of a suspension the fundamental physical aspect to be quantified is the redistribution of strain between the deformable matrix fraction of the physical mixture and the suspended phase or phases. For the case of solid particle suspensions in magma and lava the suspended crystalline phases will generally be devoid of significant internal strain during flow. With some exceptions (Cordonnier et al. 2009; Kendrick et al. 2017), the stresses driving the magmatic deformation and flow, are generally not high enough to induce significant crystal deformation (see however below). Thus, the primary task becomes one of defining the geometry of the suspended phases and their potential redistribution and reorientation during viscous flow. For the case of significantly deformable suspended phases (e.g., gas-filled vesicles, immiscible oxide or sulfide melts as well as enclaves suspended during magma mixing) the distribution of the strain between the matrix liquid and the vesicular gas or suspended fluid inclusions must be dealt with using the concept of the deformability of the bubble or inclusion shape (Taylor 1932; Stein and Spera 1992). Taken together, the rheology of a multiphase liquid-supported lava or magma can then be seen as the trivial but not simple task of quantifying strain partitioning between the vesicles and melt together with the quantification of the distribution of all suspended phases and the shape consequences of the vesicle deformation.

Generally, in particle (i.e., crystal) suspension rheology the distribution of the non-deformable space associated with the suspended crystalline phase is parameterized in terms of crystal fraction, size, shape, orientation, and their respective distributions. Beyond this more or less classical treatment of suspension rheology lie however further considerations which are specific to the case of a silicate magma or lava from which the crystalline phases are growing during flow.

Firstly, in any protracted crystallization scenario between liquidus and solidus, the composition of the liquid matrix must evolve with crystallization. Given the sensitivity of silicate melt viscosity to composition and its growing importance with decreasing temperature, a very precise control on the matrix liquid composition is required in any study of silicate melt suspension rheology in order to distinguish the chemical effects from the physical effects of crystallization on rheology. Fortunately, for systems which quench naturally or which can be quenched in experiments to a glassy matrix, the shift in viscosity due to the shift in chemistry of the melt phase can be easily determined via scanning calorimetry using the principle of a shift factor between melt viscosity and melt calorimetric glass transition temperature. The groundwork for this technique has been well laid (Gottsmann et al. 2002; Giordano et al. 2005) and it has been applied in previous studies of suspension rheology involving microlites (Stevenson et al. 1996, 2001).

Somewhat more challenging is the case of potential chemical melt gradients. If crystal growth is driven by diffusion-controlled processes, then crystal growth will lead to chemical compositional gradients in the immediate vicinity of the growing crystal–melt interfaces. For crystal growth we may expect that the shift in SiO_2 content due to the generally anticipated non-eutectic crystal growth may lead to significant viscosity gradients around growing crystals. For the case of growing vesicles, it is the water content that may vary in cases where the vesicle growth is diffusion controlled by water (Hurwitz and Navon 1994; Humphreys et al. 2008; McIntosh et al. 2014). These water gradients should generate very substantial viscosity gradients and in general this effect should become more extreme with decreasing pressure and thus total water contents of the system.

Finally, we must not forget volume relaxation effects (Dingwell and Webb 1989; Bagdassarov and Dingwell 1993a,b) or non-Newtonian melt viscosity effects (Li and Uhlmann 1970; Dingwell and Webb 1989). For vesicle-free suspensions, volume relaxation will only be relevant in frequency domain rheology measurements where the total strain on the system is very low. For vesicle-rich systems, the rheological description of the suspension must take into account the compressibility and/or decompressive growth of vesicles and the resulting volume deformation contributions.

For melt rheology (i.e., pure liquids), prediction of the occurrence of non-Newtonian behavior is straightforward if the stress distribution is known and the strain rate can be observed. The general rule of 2.5 log units distant from the calculated stress relaxation time of the Newtonian liquid via the Maxwell law is a good predictor. The challenge may however lie in the determination of stress distribution in multiphase samples where the stress may accumulate in the liquid phase in local restrictions and therefore drive non-Newtonian response in a spatially localized manner (Caricchi et al. 2007; Lavallée et al. 2007; Ishibashi 2009; Deubelbeiss et al. 2011); see also Lavallée and Kendrick (2022).

2. CONVENTIONAL DESCRIPTIONS OF RHEOLOGICAL DATA

The shear viscosity of pure silicate melts has been described over a large compositional and temperature range (see Russell et al. 2022, this volume). It has been documented that silicate melts behave as Newtonian fluids as long as the inverse strain rate remains smaller than the melt's structural relaxation timescale τ, which is described by the Maxwell relationship; $\tau = \eta_0/G_\infty$, where η_0 is the shear viscosity at zero frequency and G_∞ is the melt's shear modulus at infinite frequency. Thus, τ describes the timescale at which the melt's microstructure can respond to accommodate strain and identifies the transition between relaxed flow and unrelaxed fracture. Dingwell and Webb (1989) and Webb and Dingwell (1990b) describe that the onset of non-Newtonian flow occurs when:

$$\tau = \frac{10^{-3} G_\infty}{\eta_0} \tag{2.1}$$

with the assumption that $G_\infty = 10^{10}$ Pa for silicate melts, which has proven to accurately reproduce the rheological behavior of most silicate melts (Dingwell and Webb 1989). All data and models reviewed below concern strain-rate regimes where the melt phase of the suspension remains in the Newtonian regime and any non-Newtonian effects derive from the presence of the suspended particles (crystals) and/or bubbles.

Parameterization of the rheology of any suspension requires establishing the relationship between the imposed shear stress ($\dot{\varepsilon}$) and the resulting deformation rate (i.e., shear strain-rate), or *vice versa*. To assess the material's flow behavior, the imposed stress is plotted against strain rate, producing flow curves (Lenk 1967). Examples of common flow curves are shown in Figure 2.1 and all variables used in this chapter are defined in Table 1.1. The flow regime is defined as Newtonian when shear stress (σ) is proportional to strain rate ($\dot{\varepsilon}$):

$$\sigma = \eta\dot{\varepsilon} \tag{2.2}$$

where η defines the Newtonian viscosity. Relaxed silicate melts display Newtonian viscosity that is independent of strain-rate but usually strongly dependent on other variables (e.g., temperature, composition, redox—see Russell et al. 2022, this volume). However, the presence of a solid or a gas phase can cause the viscous flow behavior of a suspension to deviate from that of its liquid component as well as introduce non-Newtonian behavior and thus requires more complex parameterization strategies. The flow regime is non-Newtonian (see Fig. 2.1) when shear stress is not proportional to strain rate (shear thinning or thickening behavior), when a minimum stress is required before viscous flow initiates (Bingham regime) or when both behaviors are combined (Herschel–Bulkley model), the latter of which is expressed as:

$$\sigma = \tau_y + K\dot{\varepsilon}^n \tag{2.3}$$

where τ_y is the yield stress that is to be overcome in order to initiate flow; K is the flow consistency and n the flow index; describing the degree of non-Newtonian behavior. For Newtonian materials $\tau_y = 0$, $n = 1$ and $K = \eta$; for shear-thickening ($n > 1$) and for shear-thinning materials ($n < 1$) (Herschel and Bulkley 1926).

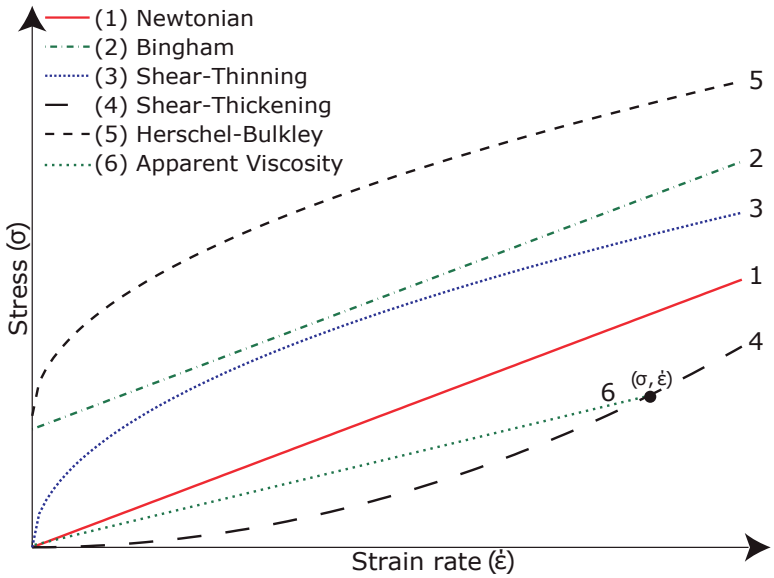

Figure 2.1. Flow curve examples: **1.** Newtonian $\sigma = \eta\dot{\varepsilon}$. **2.** Bingham $\sigma = \eta_B\dot{\varepsilon} + \tau_y$ with τ_y being the yield stress and η_B the Bingham viscosity. **3.** Shear thinning $\sigma = K\dot{\varepsilon}^n$ with n, the flow index, < 1 and K the consistency. **4.** Shear thickening $\sigma = K\dot{\varepsilon}^n$ with $n > 1$. **5.** Herschel–Bulkley $\sigma = \tau_y + K\dot{\varepsilon}^n$ plotted as shear thinning (i.e., $n > 1$). **6.** Apparent viscosity $\eta_{app} = \sigma/\dot{\varepsilon}$, is the slope of a line from the origin to a specific point along any flow curve in σ–$\dot{\varepsilon}$ space (i.e., the momentary observation at a set of experimental conditions). Every flow curve is constructed from multiple such measurements of apparent viscosity.

Table 1.1. Table of symbols.

Parameter	Unit	Description	Equation
		Section 2: Conventional Decriptions of Rheological Data	
τ	s	Timescale at which the melt's microstructure can respond to accommodate strain	2.1
η_0	Pa s	Shear viscosity at zero frequency	2.1
G_∞	10^{10} Pa	Melt's shear modulus at infinite frequency	2.1
σ	Pa	Stress	2.2
$\dot{\varepsilon}$	s^{-1}	Strain rate	2.2
η	Pa s	Newtonian viscosity of a pure silicate liquid	2.2
τ_y	Pa	Yield stress	2.3
K	Pa s	Consistency	2.3
n	–	Flow index	2.3
η_B	Pa s	Bingham viscosity	Fig. 2.1
η_r	–	Relative viscosity	2.5
η_{app}	Pa s	Apparent viscosity	2.4
η_{eff}	Pa s	Effective viscosity	2.5
η_{bulk}	Pa s	Bulk Viscosity	2.6
η_v	Pa s	Volume Viscosity	2.6
η_s	Pa s	Shear Viscosity	2.6
		Section 3: Analogue Experiments	
Re_p	–	Particle Reynolds number	3.1
St	–	Stokes number	3.2
Pe	–	Péclet number	3.3
T	K	Temperature	3.3
Sc	–	Schmidt number	3.4
η_l	Pa s	Viscosity of the liquid	3.1
ρ_l	kg/m^3	Density of the liquid	3.1
ρ_p	kg/m^3	Density of the particle	3.2
a_p	m	Particle radius	3.1
a_b	m	Bubble radius	3.1
κ	–	Characteristic length scale of the particle	3.2
k	$J\ K^{-1}$	Boltzmann constant	3.3
Ca	–	Capillary number	3.5
Γ	$N\ m^{-1}$	Bubble surface tension	3.5
		Section 4: High Temperature Experiments	
Ω	rad/s	Angular velocity	4.1
R_o	m	Outer radius, i.e., radius of the crucible	4.1
R_i	m	Inner radius, i.e., radius of the spindle	4.1

Parameter	Unit	Description	Equation
M	N m	Torque	4.2
l	m	Effective immersed length of the spindle	4.2
$\dot{\varepsilon}_e$	–	Engineering strain rate	4.3
F	N	Force	4.4
h	m	Sample height	4.4
Δ_h	m	Sample height variation	4.4
Δ_t	s	Time variation	4.4
V	m^3	Sample volume	4.4
S_{eff}	m^2	Effective surface area	4.6
Φ_b	Fraction (0–1)	Bubble volume fraction	4.8
S_{abs}	m^2	Absolute surface area	4.8
V_0	m^3	Initial sample volume	4.9
t	s	Time	4.9
k	–	Coefficient to track the porosity loss	4.9
ϕ_i	Fraction (0–1)	Initial sample porosity	4.9
ϕ_f	Fraction (0–1)	Final sample porosity	4.9
t_f	s	Final time	4.9
ε_T	–	Observed strain	4.11
α	–	Fitting constant	4.11
d	m	Sample diameter	4.14
E	Pa	Young's modulus	4.11
η_{0x}	Pa s	Viscosity of the deposit at zero porosity	4.11
G^*	Pa	Complex shear modulus	4.12
ε_r	–	Strain at any radius r	4.14
O	rad	Angle of deflection	4.14
j	$\sqrt{-1}$	Constant	4.12
σ_0	Pa	Stress amplitude	4.12
ε_0	s^{-1}	Strain amplitude	4.12
ℓ	s	Phase lag	4.12
η^*	Pa s	Complex viscosity	4.13
$\dot{O}$	rad/s	Twist rate	4.13
ω	Hz	Angular frequency	4.13
$\dot{\varepsilon}_r$	–	Strain-rate at any given radius	4.15
ω	rev/s	Twist rate	4.15
r	m	Radius of the sample	4.18

Parameter	Unit	Description	Equation
		Section 5: Field Rheology	
F	N	Force of penetration (viscous drag)	5.1
u	m/s	Speed of penetration	5.1
R_{eff}	m	Effective radius of the vane	5.1
		Section 6: Parameterization Strategies	
Φ	Fraction (0–1)	Particle volume fraction	6.1
B	–	Einstein coefficient	6.1
Φ_m	Fraction (0–1)	Maximum packing fraction	6.5
β	–	Fitting coefficient	6.11
Φ_*	Fraction (0–1)	Critical particle fraction at the onset of the exponential increase of viscosity	6.14
δ, γ, ξ	–	Empirical parameters that vary with strain-rate and particles shape	6.14
η_r (max)	–	Relative viscosity of the suspension at complete solidification i.e., $\Phi = 1$	6.15
k, n	–	Fitting parameters shaping of the sigmoidal function.	6.15
η_f	Pa s	Viscosity of a suspension with fine particle	6.16
η_c	Pa s	Viscosity of a suspension with coarse particle	6.16
$\Phi_c, \gamma_c, \xi_c, \Phi_{*c}$	–	Fitting parameters for coarse particles	6.17
$\Phi_f, \gamma_f, \xi_f, \Phi_{*f}$	–	Fitting parameters for fine particles	6.17
r_p	–	Particle aspect ratio	6.20
Φ_{ml}	Fraction (0–1)	Maximum packing fraction for equant particles and given as 0.656 for smooth and 0.55 for rough particles	6.20
b	–	Fitting parameter: 1.08 for smooth and 1 for rough particles	6.20
Φ_{m0}	–	Φ_{m0} represents Φ_m for a monomodal suspension derived from Equation 6.19	6.22
ϱ	Fraction (0–1)	Polydispersity (tends to 0 for polydisperse size distribution and tends to 1 for monodisperse suspension)	6.22
S_p	–	Ratio of the specific surface area of a polydisperse system	6.23
S_m	–	Ratio of the specific surface area of a monodisperse system	6.23
r	m	Particle radius	6.23
K_r	–	Relative consistency	6.24
n_{min}	–	Flow index at $\Phi = \Phi_m$	6.30
Φ_C	Fraction (0–1)	Critical particle fraction for yield stress that is determined experimentally	6.34
D_p	feet	Particle diameter	6.35
$\eth$		Shape factor (ratio of the surface area of a sphere of equivalent volume to the surface area of the particle)	6.35
σ_g		Geometric standard deviation for particle diameter; σ_g 2.02	6.35
A, Φ_C, m		Fitting parameters = 0.848; 0.1978, 0.8364, respectively	6.35
τ_c	Pa	Characteristic stress (or inter-particle cohesion)	6.37

Parameter	Unit	Description	Equation
τ^*	Pa	Yield stress coefficient; a fitting parameter that tends to increase with particle aspect ratio	6.39
λ_b	s	Bubble relaxation timescale	6.40
K_b	–	Characteristic stress (or inter-particle cohesion)	6.40
Cd	–	Dynamic capillary number	6.41
$\ddot{\varepsilon}$	s	Change in strain-rate	6.41
η_{r0}	–	Relative viscosity of the suspension at the low Ca limit	6.51
$\eta_{r\infty}$	–	Relative viscosity of the suspension at high Ca limit	6.51
C_X	–	Capillarity which captures the combined effect of shear and flow steadiness	6.52
Φ_t	–	Total suspended phases volume	6.54
Φ_b	–	Volume fraction occupied by bubbles	6. 54
Φ_c	–	Volume fraction occupied by particles (crystals)	6. 54
Φ_l	–	Volume fraction occupied by liquid phase	6. 54
$\eta_b(\Phi_b)$	Pa s	Viscosity of the bubble suspension (bubble + liquid)	6.59
$\eta_{r,b}(\Phi_b)$	–	Relative viscosity of bubbles suspension	6.59
$\eta_c(\Phi)$	Pa s	Viscosity of the crystal suspension (crystal + liquid)	6.62
$\eta_{r,c}(\Phi)$	–	Relative viscosity of crystals suspension	6.63

Magmatic suspensions, once exceeding the dilute regime (particle fractions $\lesssim 30$ vol%), in most cases have a strain-rate dependent viscosity and their flow behavior is best described by a flow curve rather than a single Newtonian viscosity value. The common practice, when preforming rheological experiments, is to construct these flow curves via systematic measurement of a set of apparent viscosity (η_{app}) values, which are the momentary σ–$\dot{\varepsilon}$ observations (i.e., the ratio of a given stress to a given strain-rate; 6 in Fig. 2.1) at varying experimental conditions:

$$\eta_{app} = \frac{\sigma}{\dot{\varepsilon}} \tag{2.4}$$

This apparent viscosity is, however, different from the Newtonian viscosity of a fluid even though both have the same dimension. The apparent viscosity is only valid for a specific subset of deformation conditions and varies with strain-rate. Hence it only represents a singular point on the whole flow curve but does not provide an exhaustive description of the fluid's rheology. Yet, it is useful in many cases to discuss rheological data in terms of apparent viscosity as long as it is clearly identified as such.

The presence of a suspended phase can cause the viscous flow behavior of a suspension to deviate from that of its liquid component as well as introduce non-Newtonian behavior. To describe the rheological behavior of a suspension, the term relative viscosity, η_r, is frequently employed. The relative viscosity is the ratio of the viscosity of the suspension, also called the effective viscosity (Petford 2009), to the Newtonian viscosity, η, of the suspending liquid:

$$\eta_r = \frac{\eta_{eff}}{\eta} \tag{2.5}$$

Parameterization strategies for magmatic suspensions thus aim to describe either the relative viscosity or the stress–strain-rate response of a suspension in the form $\eta_r = f(\Phi)$ or $\sigma = f(\varepsilon)$, where Φ is the volume fraction of the suspended phase (particles (crystals) or bubbles).

A further consideration to be made is that liquids and multiphase suspensions may deform under a variety of stress environments. In magmatic suspensions, shear deformation is by far the most common deformation environment, but tensile, compressive and oscillatory stresses may also become relevant for example during unloading in a volcanic flank collapse scenario or when seismic waves pass through a magma storage system. Tensile or compressive stresses may cause effects of volume viscosity to become important in addition to shear viscosity. In such cases, a bulk (or longitudinal viscosity) (η_{bulk}) is defined that is the product of volume (η_v) and shear viscosity (η_s):

$$\eta_{bulk} = \eta_v + \frac{4}{3}\eta_s \tag{2.6}$$

For the sake of brevity, the term viscosity refers to shear viscosity in this chapter unless otherwise specified. Bulk and volume viscosities become important when studying compressible materials such as bubble bearing suspensions, as it will become apparent later in this chapter for the case of parallel plate and oscillatory viscometry on bubbly melts. As an example: in parallel plate measurements, at high porosity, vesicular melts may behave in pure uniaxial compression (i.e., no bulging or sample translation) and in this case, the measured viscosity is equivalent to the samples' longitudinal viscosity. Therefore, while simple parallel plate rheometry is operationally attractive, separate determination of either shear or volume viscosity is required to completely resolve the samples' rheology, a caveat that rotational and torsional measurements avoid.

3. EXPERIMENTS ON ANALOGUE MATERIALS

Understanding the rheological behavior of magma is critical to determining magma ascent rates, force balances, flow structures as well as lava flow velocities and runout distances and even magma failure. Flow rates and internal force balances, in turn, are core parameters driving gas exsolution and crystallization. During crystallisation, the growth of solid crystals as well as the evolution of the interstitial liquid causes the transfer of components from the liquid into the crystal population. Similar transfer processes occur during degassing, i.e., bubbles form as volatiles are exsolving from the liquid into the bubble. Thus, there is an intimate feedback between a magmas textural and chemical evolution and its rheology. The technical challenges presented by measurements under natural conditions and high temperature experimentation, combined with the motivation to systematically explore texture dependent variations in the rheology of two- and three-phase suspensions have inspired a wealth of experiments on analogue materials.

The largest part of analogue studies investigates two phase suspensions of either liquid and particles (simulating crystal bearing magma) or liquid and bubbles (simulating exsolved volatiles). The central goal of these studies is to mimic the flow of natural magmas and lavas and to derive constitutive equations describing their rheology. Analogue experiments are advantageous because they allow simplification of the rheological characterization of multiphase suspensions since they do not involve the need for high temperature or pressure equipment. The sample texture (i.e., solid and/or bubble content, size and distribution) can be precisely controlled because no (or only previously anticipated) chemical interactions occur. As a result, analogue experiments are often more reproducible than experiments with natural silicate liquids and single process parameters can readily be isolated and investigated. Oftentimes, transparent materials can be used, allowing assessment of the 3D and 4D (i.e., 3D plus time) systematics of the process. Heterogeneities of natural systems can be removed, allowing an investigation of the fundamental physical behavior of suspensions. Questions arising from field relations can be simplified and

geometric relations reproduced to identify and map the process guiding parameters. As a result, these types of experiments can often reveal processes or process-systematics that may not be readily evident in natural scenarios. However, there are also a number of caveats when employing analogue materials to derive a physical understanding of magma rheology. The complexity of natural processes (geometries, dimensions, pressurization, crystallization and degassing) is difficult to recreate, requiring simplification of the process for experimentation. The necessary simplifications made during experiment design and monitoring frequently exclude the important chemical and physical feedback mechanisms that arise in natural systems, outlined above. To date, few analogue experiments have attempted to reproduce transient processes occurring in natural multiphase suspensions (e.g., crystallization and degassing).

While any experimental dataset allows to derive models describing its physical behavior, validation of the derived models cannot simply rest on further experimentation but must involve expansion and testing of the model in flow situations relevant to natural scenarios. However, application of the derived models for natural scenarios requires careful scaling of experiment size and process parameters (e.g., energy and/or forces) and validation of the derived constitutive equations on field examples can be very difficult. One of the most important considerations when carrying out analogue experimentation is therefore to precisely constrain what the experiment is set out to model. This is almost exclusively done via characterization of natural materials and/or field observations in concert with dimensional analysis. Doing so is critical since it is the only way that the derived results and constitutive equations have relevance to the natural environment.

Analogue experiments that aim to understand natural phenomena must ensure that the physical relationships of the simulated interactions compare to those of the natural system. The choice of the employed analogue material is of paramount importance in order to accurately mimic the physical behavior of natural material. Dimensional analysis is routinely employed to ensure accurate scaling of the investigated process. Below, we review the most relevant nondimensional parameters for analogue modeling of particle and bubble suspensions and present a brief overview of common experimental materials and strategies.

Particle suspension analogues

The core nondimensional parameters for analogue crystal suspensions of magmas are:

1) The particle Reynolds number, which describes the ratio of inertial forces to viscous forces of a particle within a fluid:

$$\mathrm{Re}_\mathrm{p} = \frac{\rho_\mathrm{l} a_\mathrm{p}^2 \dot{\varepsilon}}{\eta_\mathrm{l}} \tag{3.1}$$

where ρ_l and η_l are the density and the viscosity of the liquid phase, respectively and a_p is the particle mean radius. This ratio describes whether the particles' behavior falls in the non-inertial and laminar regime ($\mathrm{Re}_\mathrm{p} \ll 1$) or in the inertial and turbulent regime ($\mathrm{Re}_\mathrm{p} \gg 1$). Magmatic flow is commonly restricted to low particle Reynolds numbers (i.e., the laminar regime).

2) The Stokes number describes the coupling between the solid particles and the liquid phase as the ratio of the characteristic time of the motion of a particle subject to viscous drag and inertia, to the characteristic time of flow of the suspension:

$$\mathrm{St} = \frac{\rho_\mathrm{p} a_\mathrm{p}^3 \dot{\varepsilon}}{\kappa \eta_\mathrm{l}} \tag{3.2}$$

where κ is a the characteristic length scale of the particle, which is proportional to its radius (Coussot and Ancey 1999) but further depends on its shape, size and orientation and ρ_p is the mean particle density. This ratio allows distinguishing whether the fluid–particle coupling is

weak for St > 1; i.e., solid and fluid phases move independently and particles behave separated from the fluid; or whether the fluid coupling is strong for St ≪ 1; i.e., solid and fluid phase do not move independently and the particles behave as part of the fluid mixture.

3) The Péclet number, which relates the effects of diffusion (Brownian motion; i.e., the random motion of particles suspended in a fluid resulting from their collision with the thermal movement of molecules in the fluid) to advection (flow forces within the liquid):

$$\mathrm{Pe} = \frac{6\pi\eta_l a_p^3 \dot{\varepsilon}}{kT} \tag{3.3}$$

where k is the Boltzmann constant (1.38×10^{-23}J K^{-1}) and T is the temperature (in Kelvin). Brownian effects dominate at Pe < 10^3 (Stickel and Powell 2005), disturbing the particle alignment and thus enhancing viscous dissipation.

In the space of these three nondimensional parameters, the regime relevant to magmatic flow is hydrodynamic at (Pe ≫ 10^3), viscous ($\mathrm{Re_p} \ll 10^{-3}$) and strongly-coupled (St ≪ 1). If the particle Reynolds number is small ($\mathrm{Re_p} < 10^{-3}$) and the Péclet number is large (Pe > 10^3), both Pe and $\mathrm{Re_p}$ can be neglected, and the viscosity is a unique value at every particle concentration. The suspension thus behaves Newtonian, for a specific set of conditions of shear rates defined by values of a_p, η_l, and ρ_l. The size of this "window" scales according to the Schmidt number:

$$\mathrm{Sc} = \frac{\mathrm{Pe}}{\mathrm{Re_p}} = \frac{6\pi\eta_l^2 a_p}{\rho_l kT} \tag{3.4}$$

A suspension may behave Newtonian for greater ranges of shear rate as particle size and fluid viscosity increase, such that Sc ≫ 1. Thus, the Schmidt number may be used to anticipate the regime in which non-Newtonian effects may become important.

Bubble suspension analogues

The capillary number is the main non-dimensional parameter relevant for analogue bubble suspensions in flow scenarios where stress and strain rate are constant. It reflects the balance between the deforming, viscous, force acting on a bubble and the restoring force of the bubble's surface tension:

$$\mathrm{Ca} = \frac{\eta_l a_b \dot{\varepsilon}}{\Gamma} \tag{3.5}$$

where a_b is the radius of the spherical bubble and Γ is the surface tension at the bubble–melt interface.

While the melt viscosity is predominantly controlled by temperature and composition (Giordano et al. 2008a; Russell et al. 2022, this volume), the dependence of surface tension on temperature and composition of the melt is much weaker (Walker and Mullins 1981; Bagdassarov et al. 2000).However, the surface tension of silicate melts can vary strongly as a function of melt water content, varying from ~ 0.05 Nm^{-1} for hydrous melts (Mangan and Sisson 2005) to around 0.3 Nm^{-1} for dry melts (Bagdassarov et al. 2000).

The effect of increasing bubble volume fraction on suspension viscosity depends strongly on Ca. When surface tension dominates deformation, Ca is small and bubble shapes are spherical, whereas when the deforming stress dominates, Ca is high, and the bubbles are highly elongated. This changepoint is important because the contribution of a bubble or bubble-population to the viscosity of the bulk suspension drastically varies with shape. The effect of increasing bubble volume fraction on the suspension viscosity thus depends strongly on Ca. At low capillary number,

bubbles act to increase suspension viscosity since "rigid" spherical bubbles represent an obstacle to the flow field. At constant bubble volume, this effect decreases with increasing bubble elongation. At high capillary number, bubbles are highly elongate and flow line distortion is small. Thus, bubbles at high Ca act to decrease suspension viscosity by introducing free slip surfaces in the liquid (Rust and Manga 2002). Considerable research effort has been devoted to the parameterization of the deformation behavior of bubbles in steady and unsteady flow conditions. These are reviewed in the "*Parameterization strategies"* section in this chapter.

Experimental materials and measurement strategies

Depending on the application and level of complexity, a variety of analogue materials have been used to investigate multiphase rheology. Early works used materials such as sugar solutions in water (Einstein 1906), aqueous solutions of lead nitrate and glycerol (Ward and Whitmore 1950), latex (Maron and Levy-Pascal 1955), xylene, bromonaphthalene, or glycerine (Gay et al. 1969; Wildemuth and Williams 1985). The various liquids were largely chosen either for their viscosity at measurement conditions or for varying density at constant viscosity. However, many of these proved difficult to work with because their properties are hard to scale for application to magmatic and volcanic flows. There is a range of suitable liquids that have been used to simulate specific scenarios or rheological behaviors, which are not reviewed in detail here. Instead, the reader is referred to the work of Kavanagh et al. (2018) where the authors present a comprehensive overview over methods and properties of materials used in analogue modeling of volcanic processes. A further valuable resource is the online compilation of analogue materials for volcanology compiled by A. Rust (https://sites.google.com/site/volcanologyanalogues/home). This database provides information on a wide range of materials that have been used in volcanology. The online catalogue describes their properties and applications, while also discussing their respective limitations. The most commonly employed suspending liquids over the past decades are corn- or golden-syrup (Llewellin et al. 2002b; Rust and Manga 2002; Bagdassarov and Pinkerton 2004; Soule and Cashman 2005; Castruccio et al. 2010; Mueller et al. 2011; Jones and Llewellin 2021) and silicon oils (Sumita and Manga 2008; Mueller et al. 2010; Cimarelli et al. 2011; Del Gaudio et al. 2013, 2014; Moitra and Gonnermann 2015; Spina et al. 2016; Klein et al. 2018). The advantage of corn- or golden-syrup is that it can be mixed with water in any desired proportion. Increasing the amount of water reduces the viscosity of the suspending liquid, thus allowing to simulate, for example, varying composition and/or temperature of a magma. This does, however, make them susceptible to drying out over long experimental timescales or to take up water in very humid climates. Silicon oils on the other hand are advantageous because they exist over a very wide range of viscosities (~0.1–10000 Pa s), are generally inert and do not take up or loose humidity.

Using these liquids as suspending phase, analogue suspensions for rheological investigations are commonly prepared as two-phase suspensions: bubbles in liquid (such as in Rust and Manga 2002, Llewellin et al. 2002b), or particles in liquid (such as in Mueller et al. 2010, Moitra and Gonnermann 2015); and rarely as three-phase suspensions (bubbles and particles in a liquid); see Truby et al. (2015) for an example. This is largely owing to the complexity of interactions in three phase suspensions, which require detailed characterization of two-phase flow prior to attempting parameterization of three-phase suspensions. The most common material used to simulate spherical particles are glass beads of varying sizes, whereas glass and mineral fibres are commonly used as prolate particles (aspect ratio > 1) and particles such as mineral and glass flakes or glitter are used as oblate particles (aspect ratio < 1). Preparation of these suspensions can be challenging and time consuming because, for example, air is frequently entrained during the preparation of particle suspensions and can be difficult to remove. Further, once a homogenized particle suspension is prepared, there is a finite amount of time for which it remains homogenous since the particles begin to settle (or float) through

the suspending liquid, a process that is accelerated when aiming to remove bubbles using a centrifuge. The most common gasses to introduce bubbles in the suspending liquid are air or inert gasses such as nitrogen and argon. Preparation of bubbly suspensions can be equally challenging, since bubbles tend to rise rapidly through the suspending liquid, and it is difficult to attain a homogenous bubble size distribution. Thus, introducing bubbles in a controlled fashion requires elaborate experimental devices such as pre-measurement frothing machines used in Llewellin et al. (2002b) or *in situ* bubble supply as used in Rust and Manga (2002).

Rheometry on these analogue suspensions is for the most part performed in one of three types of rotational viscometers 1) concentric cylinder, 2) cone and plate or 3) rotating parallel plate. These techniques allow for essentially infinite strain and are thus optimal for experiments aimed at systematically mapping the rheological response of a suspension. In order to accurately measure a samples' stress–strain-rate response at varying shear rates or shear stresses it is crucial to allow for the sample to reach textural and mechanical equilibrium. It has been noted that achieving an equilibrium state requires some "pre-shear treatment" (i.e., deformation to large strains prior to measurement) because particles that are, initially, randomly oriented require a finite amount of strain before reaching equilibrium orientation distributions. This pre-shear treatment reportedly requires total strains of ~50–200 until the measurement reaches a steady value; see Figure 7a in Mueller et al. (2010). The data and parameterization strategies derived from analogue experimentation are reviewed, together with those of high temperature experimentation on natural materials in the section "*Parameterization Strategies"* later in this chapter.

Published measurements on the rheology of analogue suspensions are, to date, almost exclusively performed on non-reactive materials and in textural equilibrium. These have been critical to developing a basic understanding of the effect of crystals and bubbles on rheological properties of natural melts and magmas at steady conditions. Their application to natural environments is, however, limited since most magmatic and volcanic processes are reactive and/or operate under disequilibrium conditions, where variations in the deformation- and cooling-rates can affect both crystallization and degassing processes. These, in turn, alter the texture and rheology of the magma or lava. Recently, however, Cimarelli et al. (2011) used a slowly solidifying epoxy resin to simulate matrix crystallization of a particle suspension and Spina et al. (2016) exploited the solubility of Ar gas in silicon oil to study the vesiculation dynamics of analogue suspensions of varying particle concentrations. These experiments highlight the vast potential that still remains to be explored in studies on analogue material suspensions. Nonetheless, due to the complexity and potentially unforeseen dynamics of natural systems, combination of analogue and high temperature experimentation on natural materials is critical to generate a holistic understanding of magma transport processes.

4. EXPERIMENTS ON HIGH TEMPERATURE SILICATE MELT SUSPENSIONS

Over the past decades, considerable effort was devoted to studying the rheology of magmatic suspensions at temperatures relevant to natural processes. Due to the complexity of the problem and the technical challenges associated with high temperature experimentation, advances in the study of natural magmatic suspensions or silicate melt analogues are closely coupled to the development of new experimental machinery or methods. Most experiments to date consider the rheology of two-phase suspensions (either silicate melt and crystals or silicate melt and bubbles). Measurements on three-phase suspensions (melt–crystal–bubble) at magmatic conditions are only recently starting to become more numerous. Experimental methods for high temperature suspension rheology vary drastically depending on the nature of the investigated sample and the measurement conditions (temperature, pressure, redox conditions). This is because the viscosity of magmatic suspensions can span over 12 orders of magnitude and may involve both Newtonian and non-Newtonian behavior. A complete rheological characterization

of a magmatic suspension therefore requires a combination of several experimental methods. Owing to these challenges, most studies present data for a specific sub-set of conditions that are accessible by the employed apparatus. Further, *in situ* textural observations (as available for some suspension rheology measurements on analogue materials) are not yet possible during high temperature experimentation because the samples are housed in furnaces and often require containment in containers that are opaque to visible light and X-rays. However, some promising tomographic methods are beginning to become available (Dobson et al. 2020) and will likely fill this gap in the coming years (see the section "*Technological Advances*" in this chapter).

The most frequently used methods for high temperature suspension rheometry are concentric cylinder, rotational viscometry (Dingwell and Virgo 1987; Spera et al. 1988), parallel plate, uniaxial compression viscometry (Bagdassarov and Dingwell 1992; Hess et al. 2007) and torsion viscometry in Paterson-type devices (Paterson and Olgaard 2000; Rutter et al. 2006; Caricchi et al. 2007). Schematics of the devices and geometries are shown in Figure 4.1.

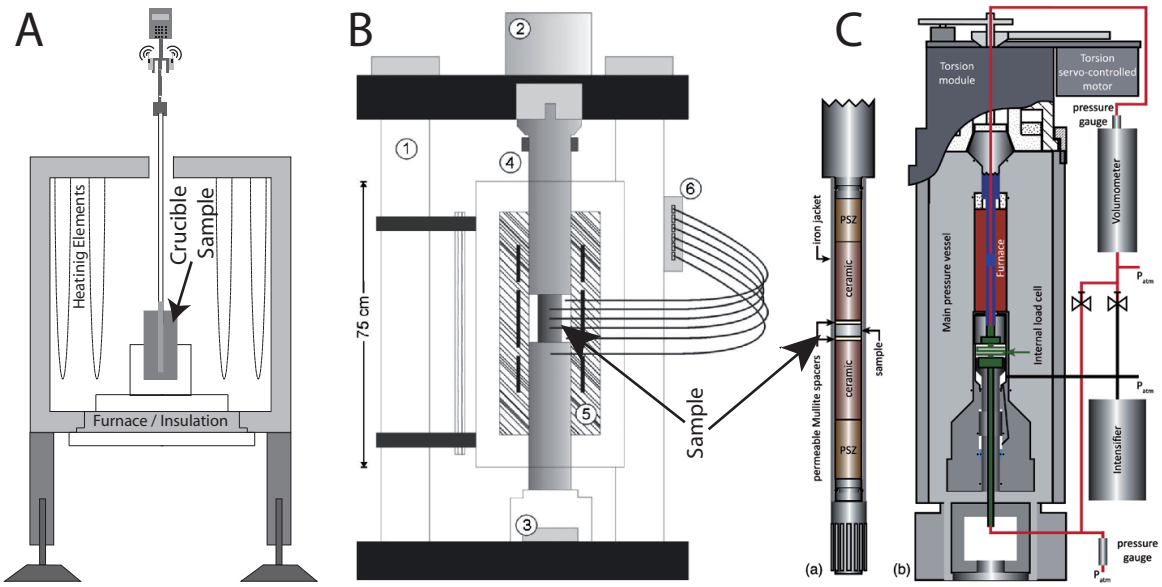

Figure 4.1 Schematics of the most common experimental devices for rheometry of magmatic suspensions. **A)** Concentric cylinder device for rotational viscometry; re-drawn from Kolzenburg et al. (2016); see also Dingwell (1986); **B)** Parallel plate device for uniaxial compression viscometry; reproduced from Hess et al. (2007), with the permission of AIP publishing; **C)** Paterson apparatus (Paterson and Olgaard 2000) for torsion viscometry; reproduced from Kushnir et al. (2017), with permission of Elsevier.

Limitations in the experimental parameters accessible by the respective devices (i.e., temperature, stress, strain-rate and oxygen fugacity) broadly divide the available data into two categories:

1. Low viscosity suspensions (commonly below ~10^4 Pa s) measured via concentric cylinder viscometry and at low degrees of undercooling (i.e., near the liquidus). The bulk compositions used in this approach usually span silica contents between ~35 to 55 wt. % SiO_2, i.e., Basalts and Foidites to Andesites (Fig. 4.2). This is because of their relatively low viscosity and comparatively fast crystallization kinetics, which allow steady state conditions in texture and suspension viscosity to be reached on the timescales of hours to days and permit quenching of the samples for textural characterization. The fast kinetics also allow for experimentation at near natural conditions (i.e., in thermal, textural and chemical disequilibrium).
2. High viscosity suspensions (commonly above ~10^6 Pa s) measured via parallel plate viscometry in uniaxial compression or via torsion viscometry. The bulk

compositions used in this approach are usually > 60 wt. % SiO_2 (i.e., Andesites to Rhyolites) with only a few examples of measurements at lower silica contents (Fig. 4.2). These experiments are typically performed just above the melt's glass transition temperature (i.e., in the supercooled liquid state). This is because these high viscosity systems have comparatively slow crystallization and vesiculation kinetics, which allows negligible textural and or chemical change of the sample over the course of the experiment and to maintain a steady state suspension viscosity over the measurement timescales (minutes to hours).

Other rheometric methods such as fibre elongation (Li and Uhlmann 1970; Webb and Dingwell 1990a), falling body viscometry (Mackenzie 1956; Kushiro et al. 1976) or three point bending (McBirney and Murase 1984), that have proven useful to investigate for example the influence of pressure on melt viscosity or non-Newtonian effects in unrelaxed, high viscosity melts have largely been abandoned for suspension rheology. The same is true for centrifuge experiments that were initially attempted for two and three phase rheometry by Roeder and Dixon (1977). Micro-penetration, that simulates the geometry of a falling sphere experiment (Hess and Dingwell 1996) has proven inadequate for determination of suspension rheology in the laboratory since it probes a comparatively small volume of melt adjacent to the indenter rather than the bulk of the sample. However, the penetration method is well suited when scaled for field measurements, where the penetrating rod is much larger than the average crystal (see "*Field Rheology*" section later in this chapter). Since both method and apparatus place tight constraints on measurement conditions, we review the advances in magma suspension rheometry grouped by the three most common experimental methods 1) concentric cylinder, 2) parallel plate and 3) torsion.

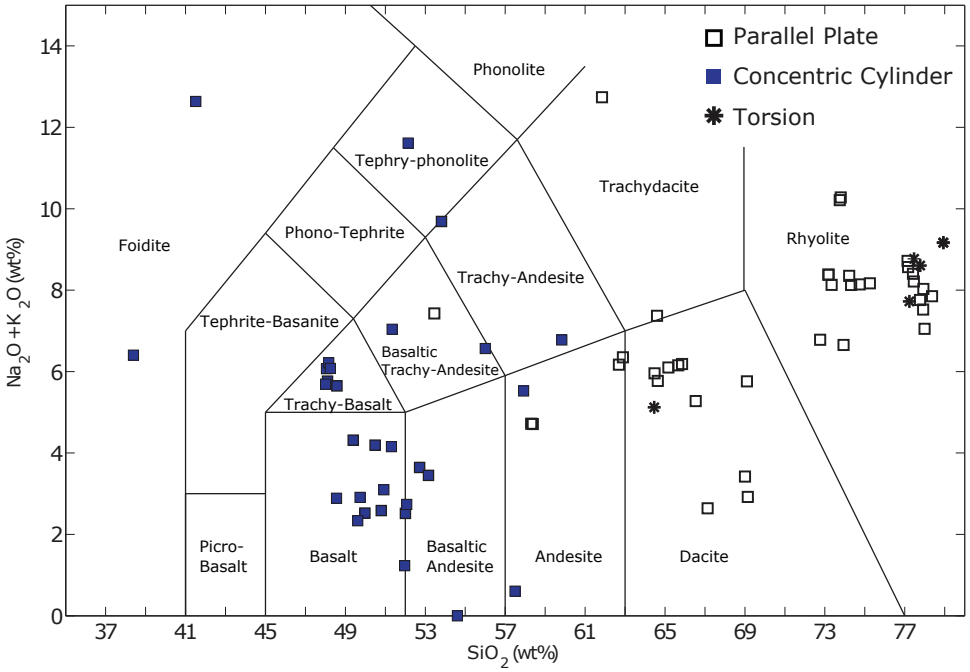

Figure 4.2. Total alkali versus silica diagram showing the compositions of published multiphase rheology measurements on lavas. Measurements of low viscosity suspensions (Foidite to Basaltic Andesite) are performed exclusively via concentric cylinder methods, whereas high viscosity magmas (Andesite to Rhyolite) are almost exclusively performed via parallel plate and torsional viscometry.

Concentric cylinder experiments

Concentric cylinder viscometry has long been a go-to technique for measuring the viscosity of silicate melts at super-liquidus temperatures (Shaw 1969; Cukierman et al. 1972;

Dingwell and Virgo 1987; Spera et al. 1988). It is commonly employed in combination with viscosity measurements near the glass transition temperature, e.g., via micro-penetration viscometry (Hess and Dingwell 1996) or estimation of the melt viscosity by application of shift factors to calorimetric data (Stevenson et al. 1995; Gottsmann et al. 2002; Giordano et al. 2005, 2008b) to interpolate the theoretical temperature-dependent viscosity of the pure melt across the crystallization interval (Tammann and Hesse 1926). This theoretical curve of the temperature–viscosity relationship of the crystal free melt is required to quantify the contribution of crystals and/or bubbles on the rheology of the bulk sample. The temperature range covered by concentric cylinder viscometry spans from 800 to 1700 °C. Theoretically, concentric cylinder viscometry allows imposing a vast range of strain rates but, in practice, the range of accessible strain rates is largely limited by the rheometer used for measurement and the method of sample containment. In current experimental geometries, the strain-rate limit is defined by either the torque limit of the rheometer or by the strength of the coupling between sample container and its holder, as the sample container may start slipping at high torque. Strain rates imposed in published data range from ~0.005 s^{-1} to ~9 s^{-1}. (Dingwell and Virgo 1988; Stein and Spera 1998; Vona and Romano 2013; Kolzenburg et al. 2018b, 2020)

In most experiments, temperature is not measured directly in the suspension because insertion of a thermocouple would disturb flow within the sample and thus affect the rheological measurement. Instead, the furnace control temperature is calibrated to the measured temperature of a non-crystalizing melt that is measured directly via insertion of a thermocouple (commonly platinum–rhodium alloys; type S or B). Concentric cylinder measurements are usually performed at atmospheric pressure and in air but experimentation under controlled atmospheres (e.g., more reducing conditions) is possible (Dingwell and Virgo 1987; Chevrel et al. 2014; Kolzenburg et al. 2018c, 2020). The importance of measurements at varying oxygen fugacity is increasingly recognized due its effect on melt viscosity (for example by reduction of Fe^{3+} to Fe^{2+}) and on the onset of crystallization as well as phase equilibria. To date, no apparatus exists that allows for concentric cylinder viscometry under pressure, a key component affecting crystal phase assembly and bubble nucleation and growth dynamics in magmatic systems but there are active efforts to expand concentric cylinder measurement capacity in that direction (see section "*Technological Advances*" later in this chapter).

For concentric cylinder experiments, the sample is melted in a cylindrical container and housed in a box or tube furnace. A cylindrical spindle is then inserted into the melt, generating the concentric cylinder measurement geometry (Fig. 4.1A). All parts in contact with the melt are commonly made of Pt–Rh alloys to withstand the high experimental temperatures and to avoid reaction between the melt and the container or spindle. More cost-effective materials, such as alumina ceramics, Pt–Rh alloys sheathed alumina ceramics or graphite, that allow for extraction of the entire sample without disturbing sample texture have been used with limited success. Alumina ceramics have proven inadequate for experiments involving low viscosity melts and high temperatures since they are soluble in the melt and induce contamination. Such contamination changes the melt composition and, with that, its viscosity, phase relations and crystallization kinetics. Nonetheless, ceramics are promising candidates for experimentation with high viscosity melts and at relatively low temperatures, which would result in negligible contamination during experimentation for durations of several days due to the much lower diffusivities in high viscosity systems and at low temperature. Graphite containers and spindles require low oxygen fugacity to avoid combustion during the experiment, which would in turn induce changes in the measurement geometry or, at worst, result in crucible failure and leakage into the furnace.

Concentric cylinder measurements quantify the torque exerted by the magmatic liquid or suspension on the rotating spindle immersed into the sample. This torque is proportional to the apparent viscosity of the sample at the imposed experimental conditions.

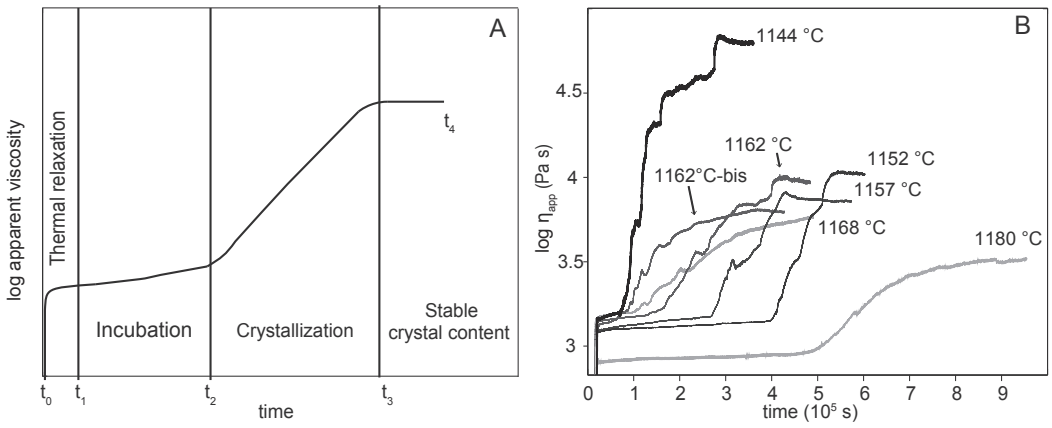

Figure 4.3 A) Schematic viscosity-time path of crystallization experiments, after Vona and Romano (2013) and Chevrel et al. (2015). As a general trend, four regions can be recognized with increasing time (*t*): 1) t_0–t_1: viscosity increase due to thermal equilibration of the melt to the experimental temperature; 2) t_1–t_2: "incubation time" time-invariant viscosity of the metastable liquid before crystallization. 3) t_2–t_3: viscosity increase due to crystallization; 4) t_3–t_4: time-invariant viscosity of the crystal–melt suspension with a constant crystal content (thermodynamic and textural equilibrium). **B)** Sample Dataset of the time and temperature dependence of the evolution of apparent viscosity during experiments at constant sub-liquidus temperature and constant shear rate; from Chevrel et al. (2015).

Experiments can be performed at either constant strain rate (i.e., torque is measured while the spindle is rotated at a constant rate) or constant stress (i.e., rotation rate is measured while the spindle is rotated at a constant torque). Standard concentric cylinder viscometry aims to achieve a linear velocity profile across the liquid (i.e., between inner and outer cylinder). However, linear velocity profiles are only achieved when the gap between the two cylinders is narrow, a geometry which does not lend itself to the study of particle suspensions. Therefore, most experiments on natural silicate melts are performed in wide gap geometries, where the flow velocity field is non-linear. This method can be employed to study silicate melt suspensions since it allows sufficient space to accommodate crystals and/or bubbles in the gap between cylinder and spindle while returning accurate viscosity measurements. Further, the concentric cylinder geometry allows for continuous viscosity measurement as a function of varying experimental conditions or textural changes in the sample, and infinite strain. This makes it more flexible than other methods that have limitations in total achievable strain (e.g., parallel plate viscometry). Following Couette theory, the shear stress (σ) and shear strain-rate ($\dot{\varepsilon}$) measured at the inner cylinder are described by:

$$\dot{\varepsilon} = \frac{2\Omega}{n\left(1-\left(\frac{R_\mathrm{i}}{R_\mathrm{o}}\right)^{\frac{2}{n}}\right)} \tag{4.1}$$

$$\sigma = \frac{M}{2\pi r R_\mathrm{i}^2 l} \tag{4.2}$$

where Ω is the angular velocity, M the measured torque, R_i and R_o the radii of the inner and outer cylinder, respectively, l is the effective immersed length of the spindle and n is the flow index. The value of the flow index (n) is determined as the slope of M vs. Ω in log-log space. From Equations (4.1) and (4.2) the sample's flow curve (σ vs. $\dot{\varepsilon}$; Fig. 2.1) can be constructed to describe the rheological behavior of the measured suspension. As apparent from Equation (4.1), the wide gap setup has the disadvantage that the shear strain-rate depends on both the measurement geometry and the flow index value (n).

Alternatively, the torque-viscosity relationship can be calibrated against materials of known viscosity over the desired range of torque and rotation rate, as routinely done for viscometry of pure silicate melts. The most frequently used standards for calibration are glasses from either the National Institute of Standards and Technology (NIST; formerly National Bureau of Standards, NBS) or from the Deutsche Glas Gesellschaft (DGG) for which the temperature viscosity relationships are accurately known. Using linear fits to the calibration data, a torque measurement at a certain rotation rate corresponds to the apparent viscosity of an unknown suspension.

Tying sample texture to the rheological response of a suspension fundamentally relies on accurate quantification of textural parameters including crystal or bubble content, shape (aspect ratio) and size-distribution, and particle surface roughness (see also the "*Parameterization Strategies"*section later in this chapter). Recovering these data in combination with rheological measurements lies at the heart of the motivation for most available measurements of concentric cylinder suspension rheometry.

The vast majority of studies address the effect of crystals on suspension rheology and only few concentric cylinder experiments measure bubble bearing melts. This is because concentric cylinder measurements are commonly performed near the melt's liquidus temperature (i.e., at low viscosities), where the large density differential between bubbles and melt allow for bubble percolation (i.e., buoyant separation of the exsolved gas phase) over the course of the experiment and, thus, thermomechanical equilibrium cannot be achieved for most magma compositions. The much lower density differential between common crystals and silicate melts allows maintaining textural homogeneity (i.e., constant crystal contents and shapes) over timescales sufficiently long for experimentation (hours to days). Hence, concentric cylinder viscometry is an ideal method to study magmatic low viscosity melt–particle suspensions. In the following, we review measurements of melt + crystals suspensions under equilibrium and disequilibrium conditions and their use for mapping of the full rheological behavior of crystallising lava. We also include a review of the few measurements of melt + bubble suspensions employing this experimental approach.

Crystal-bearing suspensions at equilibrium conditions. For experimentation at equilibrium conditions, the sample is first molten at super liquidus temperatures to determine the viscosity of the crystal free melt. Subsequently, the sample is cooled to sub-liquidus temperatures at which crystallization is expected to occur. The environmental parameters (temperature, oxygen fugacity and shear-rate) are then maintained constant and the rheological response of the sample is monitored as a fuction of time. Some of the first experiments of this type were inspired by and combined with field measurements, which are reviewed later in this chapter. These were performed on lavas from Hawaii (Shaw 1969) and Etna (Gauthier et al. 1973). Both studies note profound sub-liquidus deviations from the liquid viscosity trend as well as from Newtonian behavior at deformation rates relevant to lava flows. Subsequent studies, such as Ryerson et al. (1988) and Pinkerton and Stevenson (1992), began to focus on systematic laboratory experimentation, and the combination with field measurements was discontinued after the work of Pinkerton and Norton (1995); see the "*Field Rheology*" section later in this chapter. While the aforementioned studies attempted connecting measurements of crystal contents to the rheological data using complementary petrological experiments, none of them present systematic textural analyses of the experimental samples themselves. This combination was introduced by Sato (2005) who highlighted the need for more detailed experimentation by documenting a profound discrepancy between the rheology of elongate plagioclase bearing suspensions with respect to suspensions of spherical particles (Marsh 1981) (see section "*Parameterization strategies*" later in this chapter for more details). Efforts to recover textural data and crystallization kinetics of the experimental samples were developed only later (Ishibashi and Sato 2007, 2010; Ishibashi 2009). These studies provided unprecedented detail on the non-Newtonian effects of magmatic suspensions including thixotropy, shear thinning and apparent yield stress. Some other studies (Sonder et al. 2006; Hobiger et al. 2011) present systematic mapping of shear rate effects on magmatic suspensions at various temperatures but omit textural data, thus impeding parameterization.

Continuous temporal monitoring of the viscosity evolution from super liquidus to steady state sub-liquidus conditions, which allows commenting on the process kinetics, combined with systematic mapping of shear rate effects and analysis of textural features of the sample were first presented about a decade ago (Vona et al. 2011) but are starting to become more numerous in recent years (Vetere et al. 2013, 2017, 2019; Vona and Romano 2013; Sehlke et al. 2014; Chevrel et al. 2015; Sehlke and Whittington 2015; Campagnola et al. 2016; Soldati et al. 2016, 2017; Liu et al. 2017; Morrison et al. 2020). Figure 4.3 shows the schematic temporal evolution of viscosity in this type of experiment. The data show a profound time dependence and follow a characteristic four stage evolution:

1. During the initial temperature drop from super-liquidus temperatures to the experimental sub-liquidus temperature, the measured viscosity increases rapidly due to the temperature dependence of melt viscosity (thermal relaxation).
2. A period of constant, or very slowly increasing, viscosity, commonly termed "incubation time", which has been shown to range from minutes to days. The duration is a function of both the degree of undercooling (i.e., temperature difference between sample temperature and liquidus temperature) and melt-viscosity. The detailed kinetics of this incubation period remain poorly understood and incubation times are poorly reproducible in experiment. Nonetheless, systematic changes are documented and, generally speaking, increasing undercooling decreases incubation time, whereas increasing viscosity increases incubation time.
3. A relatively sharp increase in viscosity that is a result of the effect of crystal growth throughout the sample. It has been shown that crystallisation is often not homogeneous but propagates through the crucible from the walls of both the crucible and the spindle toward the sample center, a result of increased nucleation efficiency at both surfaces (Chevrel et al. 2015; Kolzenburg et al. 2018). This increase of viscosity gradually decelerates until reaching thermodynamic equilibrium (i.e., constant crystal content) and mechanical equilibrium (i.e., homogenous crystal alignment within the flow field).
4. A plateau in the measured viscosity, which represents the apparent viscosity of the suspension after reaching thermodynamic and textural equilibrium (i.e., sample temperature, crystal content and torque measurement are constant). When reaching this plateau, it is common to vary the shear rate to investigate the non-Newtonian behavior of the suspension. At the end, the measurement is stopped, and the sample is quenched for textural analyses.

Attaining this equilibrium state (t_4 onward) prior to any further rheological investigation of the sample (such as variations in shear rate) or quenching of the sample for textural analyses is important because the sample temperature is not measured directly. Constant thermal conditions as well as cessation of crystal growth are assumed to be achieved once a steady torque reading is reached. The time required to reach this steady state depends strongly on the sample composition and the melt viscosity since both affect the crystallization kinetics. In this type of experiment, the equilibrium state can be reached within few hours for low viscosity samples (Vona et al. 2011), while it may take several days for higher viscosity samples (Chevrel et al. 2015). Detailed studies on this incubation time are few and mostly provide measurements of nucleation delay in the absence of deformation (Swanson 1977; Couch et al. 2003; Hammer 2004). These studies also provide quantitative descriptions of nucleation and growth rates and note that the incubation time varies systematically as a function of proximity to the melt liquidus (i.e., degree of undercooling), where a lower degree of undercooling results in longer incubation times. Systematic understanding of the nucleation delay requires extensive experimental efforts coupled with thermodynamic modeling. Recently, Rusiecka et

al. (2020) have performed such work and developed a model predicting the nucleation delay of olivine, plagioclase, and clinopyroxene in basaltic melts, and alkali feldspar and quartz in felsic melts that is based on classical nucleation theory and benchmarked with experimental data from experiments performed in the absence of deformation in a piston cylinder apparatus.

Since the sample reaches a quantifiable textural equilibrium in these experiments, the data allow establishing the relationships between texture and rheology as it is commonly done in experiments on analogue materials (see "*Analogue Materials*" and "*Parameterization Strategies*" sections later in this chapter). Systematic experimentation has, however, shown that the sample texture attained in the steady state is heavily dependent on the thermal- and deformation-history of the sample in the stages before reaching thermomechanical equilibrium (Kouchi et al. 1986; Vona and Romano 2013; Kolzenburg et al. 2018b). As such, the recovered experimental data are pertinent to making quantitative ties between texture and rheology but data from the rheological evolution of the sample on the path to the equilibrium state, are tightly restricted to the specific experimental conditions. Further, strain accommodation in the sample may vary from being homogenously distributed to being heavily localized. Therefore, a complete analysis requires the textures to remain undisturbed during quench. In an effort to do so, Chevrel et al. (2015) employed a new kind of spindle, where an alumina ceramic is wrapped in thin Pt-foil, allowing to maintain the entire sample undisturbed during quench without sacrificing much precious metal lab ware. Their results show strong textural organization and crystal alignment during the crystallisation stage ($t3$).

All available concentric cylinder measurements at equilibrium conditions are performed on relatively low silica content and low viscosity melts (Fig. 4.2), where the fast crystallization kinetics allow experimentation over manageable timeframes. Further, they are dominantly measured in air and at atmospheric pressures. Therefore, most data are acquired and interpreted with respect to the emplacement of lava flows. With decreasing temperature (i.e., increasing degree of undercooling) all studies observe increasing effective viscosity as a result of increasing crystal fraction. The onset of non-Newtonian, shear thinning, behavior is documented at crystal contents above ~5 vol% and becomes more pronounced as undercooling, and therewith crystal content, increases. While some studies comment on the potential existence of thixotropy (Sato 2005; Ishibashi and Sato 2007, 2010; Campagnola et al. 2016) in the measured magmatic suspensions, conclusive evidence is not available to date. This is likely because strain-dependent changes in the textural configuration of the experimental sample impede reproducing previous textural states that would be required to ascertain thixotropic behavior (Barnes 1997).

Overall, the available data highlight that detailed knowledge of magma and lava undercooling, as well as strain and strain-rate dependent effects on the crystallization kinetics, is required to assess the resulting changes in rheology and, therewith, flow velocity of magmas and lavas. This outlines the necessity of incorporating the complex feedback mechanisms between flow environment (i.e., slope for lavas and pressure differential for magma plumbing), flow velocity and lava rheology into transport models of magmatic suspensions.

Crystal-bearing suspensions at disequilibrium conditions. The experimental efforts reviewed above are dedicated to understanding the multiphase rheology of lava at constant environmental and textural conditions. This is because this type of experiment provides the data required to derive empirical rheologic laws from the experimental data (see section "*Parameterization Strategies*" for details later in this chapter). However, the conditions of subsurface magma migration and flow of lava on the surface of Earth and other Planets are inherently dynamic and induce disequilibrium. Measured and modelled cooling rates of basaltic lavas during flow and ascent range from 0.01 to 20 °C/min (Huppert et al. 1984; Flynn and Mouginis-Mark 1992; Hon et al. 1994; Cashman et al. 1999; Witter and Harris 2007; La Spina et al. 2015, 2016; Kolzenburg et al. 2017). These values are mostly representative of conduit wall contacts and lava flow crusts and can, therefore, be taken as maximum values

that are expected to be lower in the interior of well insulated systems. Decompression during ascent is another factor promoting crystal growth and influencing its kinetics (Hammer and Rutherford 2002; Blundy et al. 2006; Arzilli and Carroll 2013). In addition, shear-rates during viscous transport in volcanic plumbing systems can range from ~70 s^{-1} in Plinian eruptions (Papale 1999) to as low as 10^{-9} s^{-1} in slowly convecting magma chambers (Nicolas and Ildefonse 1996) and effusion-rates for basaltic eruptions range between 1–1000 m^3s^{-1} (Harris and Rowland 2009; Coppola et al. 2017). For common lava flow geometries (thickness between 2 and 10 m; widths between 200–1000 m) this translates to shear-rates between ~0.001–2.5 s^{-1}. Further, magmas are generated at low oxygen fugacities (fO_2) and then transported and erupted on Earth's surface, moving towards increasingly oxidizing environments. The effect of oxygen fugacity on the viscosity and structure of silicate melts relevant to natural compositions has been investigated for a range of compositions (Hamilton et al. 1964; Mysen and Virgo 1978; Mysen et al. 1984; Dingwell and Virgo 1987; Dingwell 1991; Herd 2003; Liebske et al. 2003; Sato 2005; Vetere et al. 2008; Chevrel et al. 2013a; Kolzenburg et al. 2018). Oxygen fugacity also strongly affects the stability of Fe-bearing phases, the onset of crystallization and degassing, as well as the melts crystallization-path and -kinetics and glass transition temperature (T_g) under both static (i.e., constant T and P) and dynamic (decreasing P and T) conditions (Hamilton et al. 1964; Sato 1978; Toplis and Carroll 1995; Bouhifd et al. 2004; Markl et al. 2010; Arzilli and Carroll 2013; La Spina et al. 2016; Kolzenburg et al. 2020). Therefore, evaluating the influence of the evolving environmental parameters on the transport and emplacement dynamics of magmatic suspensions requires systematic characterization of their rheological properties at non-isothermal and non-equilibrium conditions.

The importance of disequilibrium effects on crystal growth has been recognized for decades (Walker et al. 1976; Pinkerton and Sparks 1978; Coish and Taylor 1979; Gamble and Taylor 1980; Lofgren 1980; Long and Wood 1986; Hammer 2006; Arzilli and Carroll 2013; Vetere et al. 2015; Arzilli et al. 2018; Kolzenburg et al. 2020) and has inspired experimental studies investigating the cooling- and shear-rate dependence of the dynamic rheology of crystallizing silicate melts at conditions near those of natural emplacement scenarios (Kouchi et al. 1986; Ryerson et al. 1988; Giordano et al. 2007; Vona and Romano 2013; Kolzenburg et al. 2020). The number of published rheological studies at disequilibrium conditions is, however, low and systematic mapping of the effects of cooling rate (Giordano et al. 2007; Kolzenburg et al. 2016, 2017, 2019; Vetere et al. 2019), shear rate (Kolzenburg et al. 2018b) and oxygen fugacity (Kolzenburg et al. 2018c, 2020) as well as their interdependence is only beginning in recent years. This is largely because disequilibrium experimentation does, to date, not allow for textural characterization of the sample during experimentation, which would be necessary for standard rheological parameterization (see the "*Parameterization Strategies*" section later in this chapter). Diffusion and crystal growth are very rapid at the high degrees of undercooling reached in constant cooling disequilibrium experiments and it is therefore not possible to extract and quench the experimental charges sufficiently fast to investigate their textures. Quantification of textures during disequilibrium experiments would require data at high spatial and temporal resolution, such as *in situ* tomographic data, as it is starting to become available for analogue materials (Dobson et al. 2020). Further, variations in the thermal inertia of the experimental apparatus induce characteristic thermal paths in the investigated melts which require *in situ* thermal monitoring of the sample. This was hindered in concentric cylinder viscometry, as hard-wired data transmission compromises the highly sensitive torque measurements for accurate viscosity determination. In temperature-stepping experiments this can be overcome by calibrating the sample against the furnace temperature (Dingwell 1986). At disequilibrium, however, the release of latent heat of crystallization (Settle 1979; Lange et al. 1994; Blundy et al. 2006), redox foaming (i.e., liberation of oxygen gas bubbles during reduction of Fe_2O_3 to FeO; see also Dingwell and Virgo (1987)), heat advection and changing heat capacity may also influence the samples' thermal state. Further, temperature calibration without deformation, cannot assess viscous-heating effects potentially

acting at high viscosities and/or high shear rates (Hess et al. 2008; Cordonnier et al. 2012a). A new experimental device that allows for *in situ* thermal characterization of rheological measurements was presented in Kolzenburg et al. (2016) and may serve to address the above questions in the future (see for example Kolzenburg et al. 2020).

The available disequilibrium data document that, at the conditions charted to date, cooling rate is the governing parameter determining the rheological evolution of magma and shear rate and oxygen fugacity play smaller roles. All presented experimental data describe a systematic sub-liquidus rheological evolution (Fig. 4.4). The measured apparent viscosity initially follows the pure liquid curve and once crystallization occurs, the apparent viscosity of the suspension (also sometimes called the effective viscosity; Petford, 2009) deviates from this curve towards higher viscosity values. Over the course of the experiment, the apparent viscosity of the magmatic suspension gradually increases with increasing undercooling until reaching a point where the apparent viscosity of the suspension rises steeply, terminating its capacity to flow at the "rheological cut off temperature" (T_{cutoff}); see Kolzenburg et al. (2017). This point is commonly assigned as the stopping condition for cooling limited lava flow behavior (Wilson and Head 1994; Harris and Rowland 2009) but systematic experimental determination of this temperature only started over the past few years. The available data show that increasing cooling rate delays the crystallisation onset and hence decreases the temperature at which the initial departure from the liquid curve occurs as well as reducing T_{cutoff}. Decreasing oxygen fugacity decreases the temperature of the crystallisation onset and hence decreases the temperature at which the suspension viscosity departs from liquid viscosity and the T_{cutoff} (Kolzenburg et al. 2018c, 2020). Conversely, increasing shear-rate promotes crystallization (Kouchi et al. 1986; Vona and Romano 2013; Kolzenburg et al. 2018b; Tripoli et al. 2019) and therefore acts to increase both the temperature of the departure from liquid viscosity and T_{cutoff}. This is the case for any investigated cooling rate and composition. Currently available data (see Fig. 4.4. as example) suggest that, while inducing important changes, shear-rate does not out-scale the effects of cooling-rate or oxygen fugacity (Kolzenburg et al. 2018b). While standard rheological parameterization of disequilibrium data is not possible due to the lack of quantitative textural data, T_{cutoff} measurements present a promising approach to develop an empirical understanding of stopping criteria that can be implemented in magma and lava transport models at low computational cost (Harris and Rowland 2001; Chevrel et al. 2018).

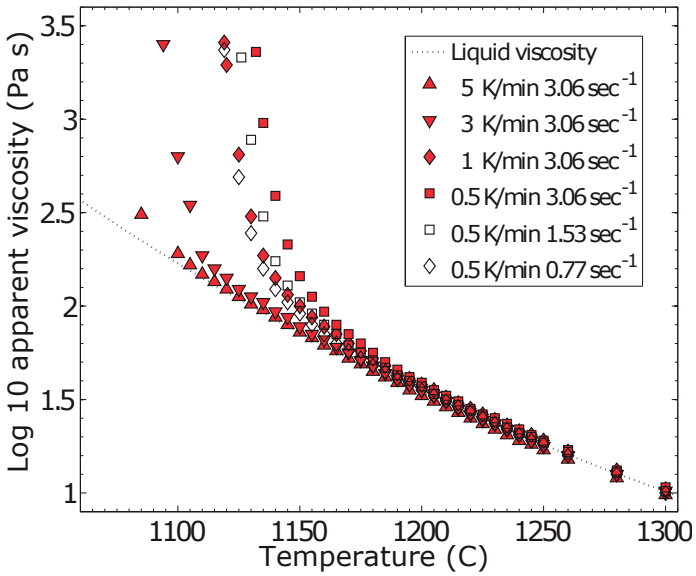

Figure 4.4. Evolution of apparent viscosity under constant cooling at various cooling and shear rates; data from Kolzenburg et al. (2017). All data describe a similar trend, where during constant cooling from super-liquidus to sub-liquidus temperatures the apparent viscosity initially follows the pure liquid curve and once crystallization occurs, the apparent viscosity deviates from this curve towards higher viscosity values.

Rheological mapping of crystal-bearing suspensions. To describe the full rheological evolution of a magma batch over the course of its journey to and on the surface requires rheological characterization over a wide range of sub-liquidus temperatures and shear-rate conditions. This can be done by combining data from equilibrium and disequilibrium experiments as well as from other techniques (e.g., parallel plate). An example of such a rheological map, representing the physical behavior of a given starting bulk rock composition from super- to sub-liquidus (crystal-bearing suspension) conditions, is given in Figure 4.5. The melt compositions of Vona et al. (2011) and Kolzenburg et al. (2018c), albeit stemming from different eruptions, are within analytical error for all major oxides and hence all variations in the rheology of the crystallizing basalt are controlled by variations in the volumetric fractions of crystals and bubbles rather than melt composition. The megacryst-bearing lava measured in Vona et al. (2017) is slightly more silicic (~+4 wt.% SiO_2) and hence somewhat more viscous. Comparison of the pure liquid viscosity of the re-melted bulk rock and the separated groundmass presented in Vona et al. (2017) document that, for basaltic melts, crystallization induced variations in melt composition result in small changes (<0.2 log units) in the liquid viscosity of the evolving suspension. Note that this is due to the compositional similarity of the melt and the crystallizing phases. This effect will be larger if the crystal growth induces significant changes in the melt composition, which is not the case in this example.

The non-isothermal viscosity data from Kolzenburg et al. (2018b) document that both cooling-rate and shear rate exert a modulating effect on the disequilibrium rheology of the Etna melt. However, the concentric cylinder measurements are mechanically restricted to relatively low viscosities. Measurements beyond the mechanical limit of concentric cylinder viscometry were presented in (Vona et al. 2017) who employed parallel plate viscometry to measure the viscosity of three phase magmatic suspensions (this method is reviewed in detail in the following section). Combined, the data from both methods form a continuing trend with respect to the concentric cylinder viscometry measurements (Kolzenburg et al. 2018b) (Fig. 4.5) but document lower lava

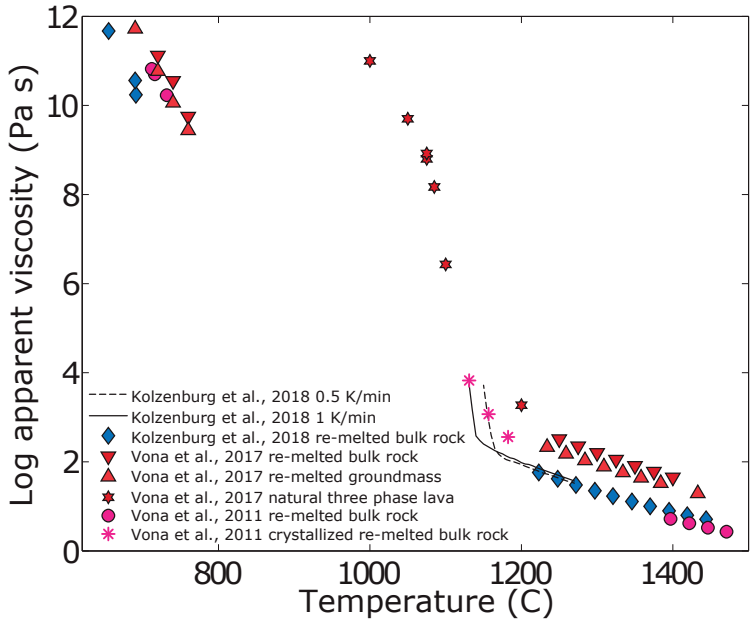

Figure 4.5. Summary plot of apparent viscosity vs. temperature for published melt and crystal-suspension viscosity data on re-melted lava samples from Mt Etna, Italy. Viscosity of the re-melted bulk rocks and groundmass (megacrysts removed) were performed at 1) super-liquidus temperatures (i.e., pure melt at >1200 °C) via concentric cylinder, 2) low temperature (<800 °C) via micro penetration and differential scanning calorimetry; 3) at sub liquidus conditions via concentric cylinder viscometry at constant temperature (**snowflakes**) or at varying cooling- and shear-rates (**continuous and dashed lines**); Viscosity of the natural rock (i.e., the lava including groundmass, bubble and crystal) was measured at subliquidus temperature (between 1200 and 1000°C) via parallel plate viscometry using unconfined uniaxial deformation (**stars**).

viscosities than extrapolation from the two-phase measurements would suggest. This is likely a result of the differences in sample texture, where all concentric cylinder data are restricted to bubble free two-phase suspensions of crystals and melt, whereas the parallel plate viscometry data present measurements on three phase (i.e., crystal and bubble bearing) suspensions. In summary, the rheological evolution of lava at sub-liquidus conditions can be reconstructed neatly by combining datasets from differing sources. This is also shown in (Pinkerton and Norton 1995; Sehlke et al. 2014; Kolzenburg et al. 2019), where laboratory and field estimates of lava rheology at emplacement conditions are compared. The respective data fall within a close range, highlighting the potential of data correlation from various sources and the need to expand the available experimental database in order to generate a holistic view of the dynamics of magma and lava transport. Nonetheless, to date no study has shown direct correlation of field and laboratory measurements that proves beyond reasonable doubt that a one to one comparison is possible. This is largely due to the respective technical limitations of both field and laboratory rheometry.

Additionally, increasing volatile contents push the onset of crystallization to lower temperatures and increasing pressure may change the crystallisation sequence e.g., (Hamilton et al. 1964; Gualda et al. 2012; Arzilli and Carroll 2013). To date, no experimental infrastructure exists to investigate either of these effects during rheological measurements and as a result, the effects of pressure and volatile content remain uncharted. Further, the available data on disequilibrium rheology do not account for the presence of bubbles, which is largely due to the unfavorable balance between machine constraints (low torque limits inhibit measurements at sufficiently high melt viscosities to retain bubbles) and melt crystallization kinetics (high viscosity melts crystalize slowly, requiring extremely slow cooling rates). The only apparatus capable of such measurements was presented by Stein and Spera (1998) but has since been put out of comission. A promising approach for direct measurements of three phase mixtures at natural disequilibrium conditions is field rheology, e.g., Chevrel et al. (2019a), as reviewed later in this chapter.

Data from concentric cylinder measurements at both thermal equilibrium and disequilibrium enable us to produce time–temperature–transformation (TTT) diagrams. These diagrams map the time and temperature dependence of the crystallization process and, thus, qualitatively reconstruct the process kinetics. This kind of analysis of rheological data was first presented in Chevrel et al. (2015) on the example of an andesitic melt from Tungurahua, Ecuador. Figure 4.6 shows a comparison of TTT diagrams of experiments at constant undercooling by Chevrel et al. (2015) and Vona et al. (2011) with those from experiments at disequilibrium presented in Kolzenburg et al. (2017) and Kolzenburg et al. (2019). Since the location of these transitions in time–temperature space are deduced from change points in the rheological data, they can only be tied qualitatively to classical, texture derived, time–temperature–transformation data from crystallization experiments as reviewed in for example Hammer (2008). A more quantitative connection between these two types of datasets is, however, possible, when the rheological data are combined with textural analyses and models for particle suspension rheology (Kolzenburg et al. 2020).

At thermal equilibrium (Fig. 4.6A), the onset of crystallization occurs slightly earlier with decreasing temperature, reflecting the increased supersaturation of the crystallizing phases. Note that all these experiments reach a constant crystal content but remain melt-particle suspensions (i.e., they do not solidify completely). Due to the higher melt viscosity, the andesitic sample of Chevrel et al. (2015) has slower phase dynamics than the basaltic composition measured in Vona et al. (2011) and thus, both onset and equilibrium state are shifted to longer times. The two datasets at disequilibrium conditions (Fig. 4.6B) describe broadly similar trends, where the onset of crystallization (open symbols) and the point of rheological solidification (black filled symbols) shift to higher temperatures and longer times with decreasing cooling rate. The difference between the two disequilibrium datasets can be explained by the variation in composition, where the lower viscosity lava from Piton de la

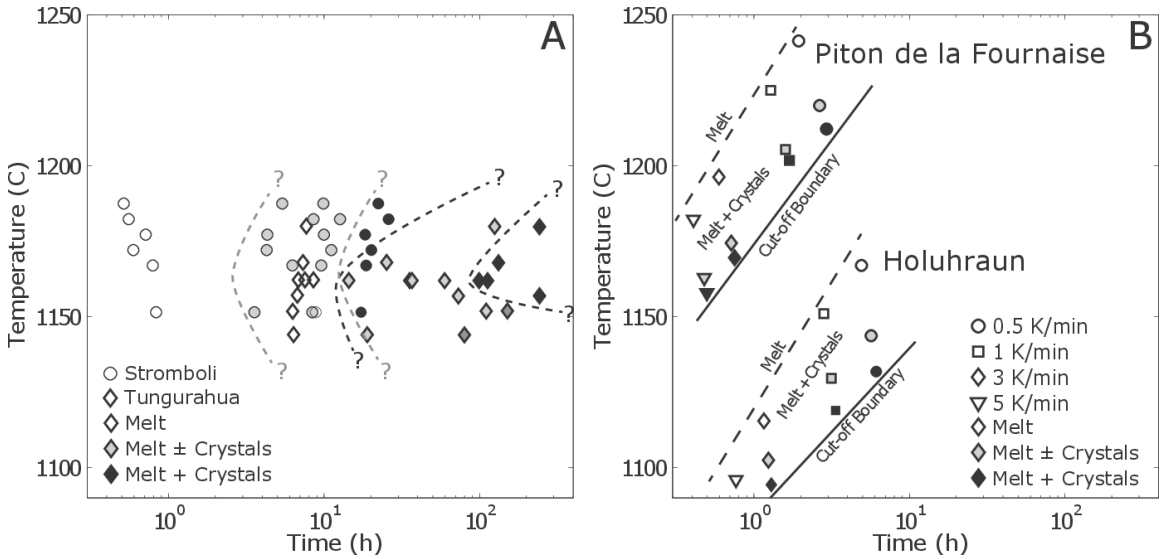

Figure 4.6. Time–Temperature–Transformation (TTT) diagrams reconstructed from viscosity measurements at atmospheric conditions (i.e., pressure and oxygen fugacity). The data plotted in **A** are reconstructed from the viscosity–time paths of thermal equilibrium measurements as shown in Figure 4.3 and were extracted from Vona et al. (2011) (**circles**) and Chevrel et al. (2015) (**diamonds**). **Open symbols** are the pure liquid phase (t_1 in Fig. 4.3), **gray symbols** describe the time of the crystallization onset (t_2 in Fig. 4.3); **black symbols** correspond to the thermodynamic equilibrium – constant crystal content (t_3 onward). **Dashed black and gray lines** delineate the time of the crystallization onset (low temperature) and thermodynamic equilibrium (high temperatures), also called the "crystallization nose", for the Vona et al. (2011) and Chevrel et al. (2015) datasets, respectively. The data plotted in **B** are reconstructed from the viscosity–time paths of measurements under constant cooling – thermal disequilibrium – (Kolzenburg et al. 2017, 2019). The individual data points for each cooling rate represent the times at which 1) the relative viscosity departs significantly from the liquid viscosity (**open symbols**; $\eta_r > 0.2$; highest temperature) 2) the relative viscosity starts to increase exponentially (**gray symbols**; $\eta_r > 2$; intermediate temperature) 3) the measurement limit at which the sample exceeds the torque limit of the rheometer and its relative viscosity tents towards infinity i.e., solidification (**black symbols**). Dotted and bold lines represent the crystallization onset and the rheological cut off, respectively.

Fournaise (La Réunion) has higher liquidus temperatures (hence the higher temperatures of the crystallization onset and solidification point) and faster crystallization kinetics (hence the shorter times required to reach both the crystallization onset and solidification point) than the Holuhraun lavas (Iceland). A prominent feature when comparing data from equilibrium and disequilibrium experiments is that at thermal equilibrium (Fig. 4.6A), the crystallization process shows a dominant time dependence (solidification occurs from left to right in the diagram), whereas at thermal disequilibrium (Fig. 4.6B), the crystallization process shows a dominant temperature dependence (solidification occurs from top to bottom in the diagram for any given cooling rate). This is because the available disequilibrium data are restricted to rather high cooling rates (> 0.5 K/min) and it is expected that at lower cooling rates (approaching equilibrium conditions), the dependence of temperature would decrease while the time dependence would increase thus merging the two experimental datasets. The measurements on the lava from Piton de la Fournaise suggest an increase in the time dependence of the process between the highest and lowest cooling rate but, to date, no coherent dataset exists that investigates this transition for a single composition and a broad range of cooling rates.

Bubble bearing suspensions

Concentric cylinder rheometry data on bubble bearing suspensions are scarce. This is largely due to the thermal and mechanical constraints of the method. Retaining bubbles in a melt at high temperatures for the duration of rheology experiments (several hours to days) requires relatively high melt viscosities (>10^5 Pa s) to minimize bubble percolation (i.e., volatile

exsolution and loss upwards through the melt). This, in turn, requires a device design that permits high torques. Only few datasets on concentric cylinder measurements of bubble bearing suspensions are published (Stein and Spera 1992, 2012; Bagdassarov and Dingwell 1993a) and few studies describe devices that could access such experimental conditions in the laboratory (Stein and Spera 1998; Morgavi et al. 2015; Kolzenburg et al. 2016). Alternatively, it was suggested that field rheometry could be used for measuring the rheology of bubble-bearing low viscosity suspension (Chevrel et al. 2018), but to date no systematic study has been published.

Parallel plate experiments

Parallel plate suspension viscometry is largely dedicated to understanding the multiphase rheology of lava and magma at constant environmental and textural conditions. The compositions used in studies employing this approach vary from Andesites to Rhyolites with few examples of Basalts (Fig. 4.2). This method allows for simple experimentation on multiphase suspensions of synthetic or natural samples, since the samples can be readily recovered by core drilling from any glass bearing rock sample. This permits detailed characterization of sample texture, an important factor for parameterization of the rheological data (see the "*Parameterization Strategies*" section later in this chapter). For accurate measurement it is crucial to ensure parallel faces of the sample surfaces in contact with the compacting pistons since uneven faces result in anomalously high strain-rates due to the reduced initial contact area and thus underestimation of the samples viscosity. The cylindrical cores are loaded in a uniaxial press (Fig. 4.1B) and heated to the desired experimental temperature. Sample temperature can be monitored by insertion of thermocouples or by calibration to reference samples. Experiments are performed near the melt's glass transition (i.e., in the supercooled liquid state), where the viscosity is sufficiently high to neglect crystallization and vesiculation timescales relative to the duration of the experiment. This minimises textural and chemical change of the sample over the course of the experiment and maintains steady state suspension viscosity over the measurement timescales (minutes to hours).

Parallel plate viscometry uses cylindrical samples that are deformed in uniaxial compression either at constant load or at constant strain-rate. Constant strain-rate experiments record stress-time relationships sensed via a load cell. Constant load experiments record strain-time relationships measured by dilatometry. Although the experiments involve relatively small total strains it is still possible to run stress or strain-rate stepping experiments (Fig. 4.7A). The simplest approach to calculate the apparent viscosity of the sample in uniaxial compression parallel plate experiments is to derive it directly from the ratio of the recorded stress (σ, i.e., load over surface area in contact with the piston) and engineering-strain-rate ($\dot{\varepsilon}_e$; i.e., variation of the sample length ($\Delta l/l$) per unit time) (Quane and Russell 2005; Avard and Whittington 2012; Heap et al. 2014; Ryan et al. 2019a):

$$\eta_{app} = \frac{\sigma}{\dot{\varepsilon}_e} \tag{4.3}$$

However, at the imposed strains (up to ~30–40 %), the sample geometry changes, and the sample strain cannot simply be described as $\Delta l/l$. Thus, Recovering the samples shear viscosity from parallel-plate viscometry requires that the geometrical change is accounted for. This approach rests on the mathematical description of the flow process by two differential equations, the Navier–Stokes equation and the continuity equation, following the Wallace plastimeter methodology (Rowlatt 1956). For isothermal conditions and with some simplifying assumptions, an analytical solution to these was obtained by Gent (1960). Based on experiments on coal tar and cross correlation with concentric cylinder viscometry, Gent (1960) validated the proposed, geometry independent (isovolumetric), theoretical formulation to recover shear viscosity from parallel plate experiments. Following this approach, calculation of the samples' shear viscosity (η_s) from the experimental data rests on one of two geometrical assumptions for the deformation mechanism.

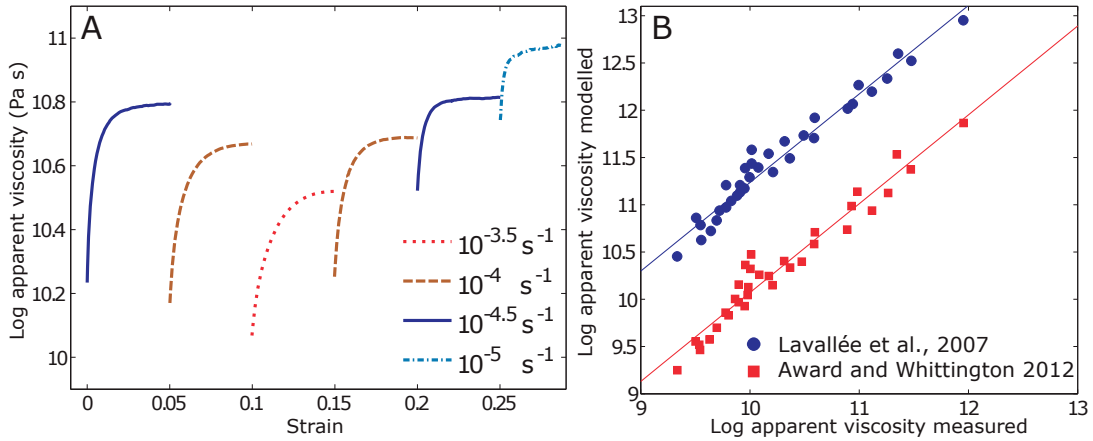

Figure 4.7. (A) Plot of apparent viscosity vs. strain for a strain rate stepping experiment on Chaos Crags (USA) dome lava (unpublished data by Kolzenburg et al.). For a given strain rate, the recorded load (and thus also the measured viscosity) initially increases rapidly until reaching a constant value equivalent to the relaxed rate of continuous sample deformation. The data describe clear shear thinning behavior (i.e., increasing strain-rate decreases apparent viscosity). **(B)** Comparison between the non-Newtonian models of Lavallée et al. (2007) and Avard and Whittington (2012) derived from uniaxial parallel plate experiments (plot modified after Avard and Whittington 2012 Fig, 12a). Note that this figure compares the model of Lavallée et al. (2007) to the one presented in Avard and Whittington (2012). As such, this is not an assessment of overall quality of one model over the other but a demonstration of the fact that that neither of these non-Newtonian models can comprehensively describe the rheology of dome lavas but each one is applicable only within the framework it was developed in. This highlights the need for further and systematic rheometry in order to derive a holistic rheological model.

1. The "no slip" condition, where the contact surface area between the sample and the parallel plates remains constant and the cylinder accommodates all deformation by bulging/barrelling. In this case the shear viscosity is calculated as follows:

$$\eta_s = \frac{2\pi F h^5}{3V\frac{\Delta h}{\Delta t}\left(2\pi h^3 + V\right)} \tag{4.4}$$

where F the applied force, h the sample height, V the sample volume and t is time. Δt and ΔV are time and volume variation, respectively

2. The "perfect slip" condition, where the contact surface area between the sample and the plates increases with deformation while the cylinder does not bulge (i.e., retains vertical sides). In this case the shear viscosity is calculated as follows:

$$\eta_s = \frac{h^2 F}{3V\frac{\Delta h}{\Delta t}} \tag{4.5}$$

Both equations are valid only for experimental geometries where the sample diameter is smaller than the diameter of the parallel plates (i.e., no sample extrusion) and the sample is assmed to be both incompressible and stay cylindrically symmetrical (i.e., not sagging under its own weight).

Further, at high porosity, vesicular melts may behave in pure uniaxial compression, meaning that neither bulging nor sample translation occurs. It is important to note here, that the deformation of bubbles contributes a significant volume viscosity to the macroscopic flow of vesicular materials and due to the compressibility of pore fluids or gases, the sample volume does, in most cases, not remain constant during experimentation. In this case, the measured viscosity is equivalent to the samples' bulk (or longitudinal) viscosity (Eqn. 2.6) and therefore additional determination of shear or volume viscosity is required to completely resolve the samples' rheology.

The main limitation of parallel plate viscometry for application to natural magmatic suspensions has long been the relatively small sample size. Most common parallel plate viscometers are restricted to cylindrical sample diameters below 10-15 mm, largely because of the balance between the high stresses required for deformation of high viscosity samples near the glass transition and the limitations in compressive strength of the materials used as pistons driving the parallel plates (ceramics, silica glass or high temperature metal alloys). For a sample to be representative of the whole rock texture, however, its diameter sample should be ~8–10 times that of the largest crystal or bubble present (Ulusay and Hudson 2006). Seeing as bubble and crystal sizes in igneous rocks commonly range from hundreds of microns up to a few centimetres, rheological studies were initially limited to microlite bearing melts with crystal sizes below ~350 micron (Lejeune and Richet 1995; Stevenson et al. 1996) and bubble sizes below 1 mm (Bagdassarov and Dingwell 1992). Although the available experimental data are few, only a limited number of studies were presented following the initial qualitative descriptions in the aforementioned contributions and there is significant potential for expansion and improvement.

The first magmatic suspensions studied with parallel plate viscometry concerned vesicular rhyolite and were presented in Bagdassarov and Dingwell (1992). However, as outlined above, the equations provided by Gent (1960) are valid only for isovolumetric systems. On first glance this makes them inapplicable to bubble bearing systems, since bubbles contain compressible gas. Several approaches have been presented to account for this issue but all of them remain to be validated by cross correlation with other rheometric methods.

Bagdassarov and Dingwell (1992) modify the perfect slip equation provided in Gent (1960) by expanding sample volume to:

$$V = h \times S_{\text{eff}} \tag{4.6}$$

And then simplifying Equation (4.5) to:

$$\eta_{\text{s}} = \frac{hF}{3S_{\text{eff}} \dfrac{\Delta h}{\Delta t}} \tag{4.7}$$

Note that they introduce S_{eff}, the effective surface area of the sample, which is corrected for the sample's surface porosity in contact with the plates:

$$S_{\text{eff}} = S_{\text{abs}} \times (1 - \Phi_{\text{b}}) \tag{4.8}$$

where S_{abs} being the total sample surface area in contact with the plates and Φ_{b} the bubble volume fraction.

Vona et al. (2016) also adapted the equation for perfect slip conditions and expanded it to account for variations in sample volume over the course of the experiment. They achieve this by measuring sample volume before and after the viscosity measurement and then distributing the volume reduction linearly over the course of the experiment:

$$\eta_{\text{app}} = \frac{h^2 F}{3\left[V_0\left(1 + kt\right)\right]\dfrac{\Delta h}{\Delta t}} \tag{4.9}$$

where V_0 is the initial sample volume and k is a coefficient tracking the porosity loss. It is defined as $k = 0.01(\phi_{\text{f}} - \phi_{\text{i}}) / t_{\text{f}}$, where ϕ_{i} is the initial porosity, ϕ_{f} is the final porosity, and t_{f} is the final time. This linear distribution of volume reduction, however, does not account for the compressibility of the gas phase in the bubble, which induces a non-linear transition from simple core shortening during the initial deformation phase to the perfect slip condition reached at the end of the experiment. As such this approach is only applicable for low strain experiments.

Bubbly silicate melts or foams are essentially impermeable unless they undergo bubble wall fragmentation (Taisne and Jaupart 2008; Takeuchi et al. 2008, 2009; Caricchi et al. 2011; Shields et al. 2014; Von Aulock et al. 2017; Ryan et al. 2019a,b). Hence they can act as gas springs due to the compressibility of the pore gas (Jellinek and Bercovici 2011). It would therefore be favorable to treat the sample as one volumetric unit and use the entire sample (melt + bubbles) surface area when converting measurement data to viscosity values (see Eqn. 4.10).

This approach could, in principle, be developed to also account for the non-linear compressibility of gases for the study of suspensions of pressurized bubbles. Ultimately, the simplest and most favorable way to recover shear viscosity from parallel plate experiments is a modified version of the method proposed by Bagdassarov and Dingwell (1992) that uses the absolute sample surface area (rather than a porosity correction) in the form of:

$$\eta_{app} = \frac{hF}{3S_{abs}\dfrac{\Delta h}{\Delta t}} \tag{4.10}$$

Due to the range of proposed data reduction approaches reviewed above, rigorous comparison of published date is not possible and hence systematic parameterization of bubble suspension and three phase suspension rheology has been impeded to date. In the following we present a review of published experimental work on magmatic suspensions, focusing on the employed apparatuses, textural variations and core findings of the respective studies.

The first experiments on bubble-free particle suspension obtained with parallel plate viscometry were performed with unimodal enstatite spherules suspended in an enstatite melt (Lejeune and Richet (1995). This study describes Newtonian behavior up to crystal volume fractions of $\Phi = 0.4$. Beyond the $\Phi = 0.4$ threshold Stevenson et al. (1996) document non-Newtonian shear thinning effects and the development of an apparent yield stress. At $\Phi > 0.7$ the deformation behavior is reported to evolve towards non-uniform distribution of crystals and melt with the onset of brittle processes (solid-like behavior). The authors state that the data support the simple Einstein–Roscoe model (see "*Parameterization Strategies*" section later in this chapter for details) for suspensions of spherical particles but also noted that crystal size distribution and shape may be of importance to fully describe textures relevant to natural samples. The latter point was demonstrated by Stevenson et al. (1996) who performed measurements on obsidian containing prismatic to needle shaped microlites and demonstrated the Einstein–Roscoe model may drastically underestimate the effective suspension viscosity once particle shapes deviate from spherical.

The sample size limitation was addressed by Quane et al. (2004) who introduced a new device capable of high temperature (up to 1100 °C) experimentation on samples of up to ~7 cm diameter and loads of up to ~1100 kg. This high-temperature, low-load apparatus was employed in a number of studies, dominantly aimed at quantifying the rheological behavior of welding and compacting volcaniclastic deposits, on both natural and analogue materials at atmospheric conditions (Quane and Russell 2005, 2006; Quane et al. 2009; Heap et al. 2014) and was later modified to allow for experimentation at elevated H_2O pore fluid pressures (Robert et al. 2008). Based on some of these data, Russell and Quane (2005) developed an empirical rheological model for welding and compacting deposits that has found wide application in numerical studies, e.g., Kolzenburg et al. (2019). The observed strain (ε_T) is ascribed to a combination of a time-dependent viscous compaction (ε_v) and a time-independent mechanical compaction (ε_m) described by:

$$\varepsilon_T = \frac{(1-\phi_0)}{\alpha}\ln\left\{1+\frac{\alpha\sigma\Delta t}{\eta_{0x}(-1\phi_0)}\exp^{\frac{\alpha\phi_0}{1-\phi_0}}\right\}+\frac{\sigma}{E(1-\phi_0)} \tag{4.11}$$

where ϕ_0 is the original porosity, σ is the stress acting on the sample, and η_{0x} and E are the viscosity and Young's modulus of the deposit at zero porosity, respectively. In this model, the effective viscosity of the crystal-bearing melt without bubbles (i.e., η_{0x} where $\phi_0 = 0$) is determined as a function of temperature. The α value is used to predict the bulk viscosity of the mixture as a function of porosity, and the increase in relative viscosity with decreasing porosity (Quane et al. 2009). Published values of α range from ~0.7 to ~5.5 (Ducamp and Raj 1989; Quane and Russell 2005; Quane et al. 2009; Heap et al. 2014) and vary as a consequence of differences in sample microstructure (i.e., porosity, crystal content, pore size and shape, particle size and shape, and pore and particle size distribution, amongst others). See Wadsworth et al. (2022, this volume) for further details on sintering and welding.

A similar device to that introduced in Quane et al. (2004) was also employed by Vona et al. (2017) to study the multiphase rheology of megacryst-rich magmas. This study documents the lava's complex rheological response related to a non-homogenous deformation of the natural sample (e.g., viscous and/or brittle shear localization), favored by the presence of bubbles. The authors argue that the obtained flow parameters can be considered as representative of the bulk rheology of natural magmas, characterized by similar non-homogeneous deformation styles. The optimal scaling relation of sample size $\gg$ largest crystal or bubble could however not be reached by this study due to machine limitations.

To date there are only few parallel plate devices that are capable of performing high load high temperature experiments on large samples. The design for a high load, high temperature deformation apparatus was introduced in Hess et al. (2007) and allows measurements on geologically relevant sample dimensions (up to 100 mm in both length and diameter). This resulted in several seminal contributions advancing the understanding of non-Newtonian effects such as viscous heating in pure melts (Hess et al. 2008) as well as strain-rate dependent rheology and viscous limit of flow during dome building eruptions (Lavallée et al. 2007, 2008, 2012; Cordonnier et al. 2009, 2012b); see also Lavallée and Kendrick (2022, this volume) . The large sample size and high load capacity directed use of this device towards investigating magma failure and shear localisation (Lavallée et al. 2008, 2012, 2013; Coats et al. 2018); mapping the boundary between viscous and elastic deformation mechanisms and exploring suspensions of high crystal volume fractions $\Phi = 0.5–0.6$. The first published datasets suggested that highly crystalline suspensions of varying composition and texture can be described by a single non-Newtonian rheological law (Lavallée et al. 2007). Successive experiments, however, showed that their behavior is more complex, involving decreases in viscosity with increasing total strain and strain-rate, resulting from changes in sample texture (i.e., breaking of crystals and textural reorganization rather than true non-Newtonian flow behavior). Therefore, further systematic characterization is needed in order to derive holistic rheological laws for magmatic three phase suspensions at eruptive conditions (Cordonnier et al. 2009; Avard and Whittington 2012).

Some interesting non-isothermal parallel plate viscometry experiments were presented in Bouhifd et al. (2004) and Villeneuve et al. (2008), in which samples of glassy basalt were heated from below their glass transition temperature to 1250 °C and 1300 °C, respectively. This induced crystallization of the glassy basalt sample while passing from the supercooled liquid state through the crystallization window to super-liquidus temperatures. The results highlight the profound effect that crystallization has to increase the effective viscosity of basaltic melts and also indicate that decreasing oxygen fugacity may inhibit crystallization in the supercooled liquid field. Unfortunately, neither of the studies provided accurate determinations of the viscosity–crystal fraction relationships or textural characterization, rendering the data not suitable for parameterization and derivation of rheological flow-laws.

Dynamic experiments tracking rheological changes during vesiculation of synthetic three phase magmas were presented in Pistone et al. (2017). The experiments document that during foaming (i.e., nucleation and growth of gas-pressurised bubbles) and inflation, the rheological

lubrication of the system is dictated by the initial crystallinity. At $\Phi < 0.6$, gas bubbles form and coalesce during expansion and viscous deformation, favoring strain localisation and gas permeability within shear bands, reducing the samples overall apparent viscosity. At $\Phi = 0.6$–0.7, gas exsolution generates pressurized pores that remain trapped in the solid crystal clusters and promote the formation of microscopic fractures within both melt and crystals, driving the system to brittle behavior. At higher crystallinity ($\Phi > 0.8$), vesiculation leads to large overpressures, triggering extensive brittle fragmentation. This novel approach to using parallel plate viscometry as a method to probe dynamic changes in flow behavior of three phase suspensions magma is very promising and presents a potentially very fruitful research path to be explored for natural magmas in the years to come.

Torsion experiments

Oscillatory torsion measurements. The first high temperature viscometry experiments on magmatic suspensions performed in torsion used a custom built forced sinusoidal torsion deformation device that induced very small oscillatory strain ($\varepsilon < 10^{-3}$ rad) in a cylindrical sample while monitoring the torque as a function of deflection angle (Bagdassarov and Dingwell 1993b; Bagdassarov et al. 1994). In oscillatory experiments, the total stress comprises two components: an elastic component in-phase with the strain and a viscous component in-phase with the strain rate. Together, these signals generate a sinusoidal signal that, in viscous and viscoelastic materials, is phase-shifted with respect to the applied stress. Measurements are performed over a range of oscillatory frequencies to determine the material's frequency dependent viscosity function. The resulting stress–strain wave forms are described in terms of complex variables having both real and imaginary parts. The complex shear modulus, G^*, is then defined as follows

$$G^* = \frac{\text{complex stress amplitude}}{\text{complex strain amplitude}} = \frac{\sigma_0}{\varepsilon_0}\cos\ell + \frac{\sigma_0}{\varepsilon_0} j \sin\ell \tag{4.12}$$

where ε_0 and σ_0 are the stress- and strain-amplitude, respectively, ℓ is the phase lag (i.e., loss angle) and $j = \sqrt{-1}$.

The complex viscosity is then defined as:

$$\eta^* = \frac{\text{complex stress amplitude}}{\text{complex strain rate amplitude}} = \frac{\sigma_0}{j\varepsilon_0\varpi} e^{j\ell} = \frac{G^*}{j\varpi} \tag{4.13}$$

with $\varpi = 2\pi f$ being the angular frequency and f the frequency.

Bagdassarov and Dingwell (1993b) and Bagdassarov et al. (1994) resolve the frequency dependent shear viscosity as a real and imaginary component in a frequency range of 0.005–10 Hz and temperature range of 600–900 °C. The authors describe that the recovered shear viscosities of magmatic suspensions at low frequencies and high temperatures compare well with data from parallel plate viscometry. They find the relaxed shear viscosity of vesicular rhyolites to decrease progressively with increasing bubble content. As documented previously by Stein and Spera (1992), magma viscosity can either increase or decrease with bubble content, depending on the rate and state (steady vs. unsteady) of strain during magmatic flow. Oscillatory torsion viscometry at high temperatures was largely abandoned after these studies with exception of one dataset on natural three phase suspensions from Etna, Hawaii and Vesuvius published in James et al. (2004). They document non-Newtonian, shear-thinning rheology in all samples for temperatures between 200 and 1150 °C but do not rigorously correlate the data to sample texture.

It is important to note that there is a fundamental difference between rheometry using oscillation experiments and all other experimental methods reviewed in this chapter. The strain induced in the sample is extremely small in most forced oscillation experiments and hence, the texture of the sample undergoes negligible change. Measurements under forced oscillation,

thus resolve the rheological regime near zero strain. This allows measuring the viscous response of a sample without inducing strain dependent effects such as bubble or crystal deformation and/or re-orientation. Sumita and Manga (2008) present a study of the oscillatory rheology of analogue suspensions of spherical particles at volume fractions of $0.2 < \Phi < 0.6$. They present data for the response of the elastic and viscous moduli as a function of oscillation frequency and find a strain dependent rheological evolution where the suspension displays three rheological regimes. The response is initially linear viscoelastic, becomes shear-thinning with increasing strain and transitions to shear-thickening at high strain amplitudes. While these data are of great value to understanding for example the viscous dissipation of seismic energy in magma bodies, they are not directly applicable to processes where large strains are expected (e.g., magma migration and lava flow). Correlation of frequency dependent data to data from methods probing higher strain regimes remains challenging, largely due to the paucity of data since torsion experimentation following the above reviewed studies focused chiefly on deformation in simple shear at much higher total strains.

Simple shear torsion measurements. Simple shear torsion viscometry is predominantly performed in Paterson type high temperature, moderate pressure apparatuses that were originally designed for rock deformation experiments. The Paterson apparatus (Paterson and Olgaard 2000) allows for sample deformation in compression and/or torsion at confining pressures of up to 500 MPa (~ equivalent to the pressure at 15 km depth) and at temperatures of up to ~1325 °C. This makes them well suited to study the effect of moderate pressures and, with that, variations in volatile contents on the rheology of magmatic suspensions. Cylindrical samples of 8–15 mm diameter and between 4 and 15 mm length are loaded in custom built load-column assemblies made of alumina and zirconia pistons enclosed in a copper or iron jacket, which is housed in an internally heated gas pressure vessel; see Figure 4.1C. Determination of sample viscosity is based on torque and rotation rate data recorded during measurement, where both the effective stress and strain rate need to be calculated following the procedure presented in Paterson and Olgaard (2000) to account for the experimental geometry and non-linear distribution of both parameters within the sample.

One inherent issue in torsion experiments, is that the strain rate of a cylindrical sample is non uniform with the highest rate at the outside of the cylinder and zero strain-rate at the center (Paterson and Olgaard 2000). However, because of the constraints of the geometry, planes of material normal to the deformation axis will remain planar, and radial lines of material normal to the deformation axis will remain linear. Any element along a radius of the cylinder undergoes simple shear in a plane normal to the radius (r), the displacement being in the direction normal to the cylinder axis.

The shear strain ε_r at any radius r is thus given by:

$$\varepsilon_r = \frac{\mathrm{O}}{h} \tag{4.14}$$

where h is the length of the sample and O being the angle of deflection and so the strain-rate at any given radius is given by:

$$\dot{\varepsilon}_r = \frac{r\dot{\mathrm{O}}}{h} \times s^{-1} \tag{4.15}$$

Quantification of the experimental data commonly rests purely on the maximum shear strain ε, at the surface of the cylinder, which is given by:

$$\varepsilon = \frac{d\mathrm{O}}{2h} \tag{4.16}$$

where d is the sample diameter and the corresponding maximum strain rate $\dot{\varepsilon}$ is given by:

$$\dot{\varepsilon} = \frac{d\dot{\mathrm{O}}}{2h} = \frac{\pi d\omega}{h} \tag{4.17}$$

where $\dot{\mathrm{O}}$ and ω are the twist rate in radians per second and in revolutions per second, respectively. The torque (M) measured in torsion represents the integrated shear stress (σ_s) over the entire cylinder and is expressed as follows:

$$M = 2\pi \int_0^{\frac{d}{2}} \sigma_s r^2 \, dr \tag{4.18}$$

Hence, for Newtonian liquids it related to viscosity as follows:

$$M = \frac{\pi d^3}{12} \eta \dot{\varepsilon} \tag{4.19}$$

whereas when assuming a Herschel–Bulkley flow law it is described as follows:

$$M = \frac{\pi \tau_y d^3}{12} + \frac{\pi d^3}{4\left(n+3\right)} K \dot{\varepsilon}^n \tag{4.20}$$

This highlights that, while strain-rate dependent non-Newtonian effects can be investigated qualitatively in a Paterson apparatus using the standard sample assembly geometry (Fig. 4.1C), rigorous strain-rate dependent rheological quantification is not possible for cylindrical samples since the strain rate varies drastically along the sample radius within the specimen. One way to overcome this issue is to use hollow cylinders as proposed by (Paterson and Olgaard 2000) who filled the hollow cylinders with a material of similar compressibility but lower internal friction. Sample strain is then confined to a narrow annulus for which it can be treated as near constant. The torque resulting from this inner plug can be calibrated and thus both shear stress and shear strain rate can be recovered, allowing for more accurate rheological measurements. To date this approach has not been employed for measurements concerning the multiphase rheology of magmatic suspensions due to a combination of the challenges of sample preparation as well as the limitations in the sample-to-crystal size ratio.

Caricchi et al. (2007), Arbaret et al. (2007) and Champelier et al. (2008) provided the first systematic viscosity measurements and textural analyses using this apparatus for experiments on synthetic suspensions. Caricchi et al. (2007) present measurements of equant quartz grains of $\Phi = 0.5–0.8$ suspended in a hydrous haplogranitic melt, whereas Arbaret et al. (2007) present measurements of $\Phi = 0–0.76$ of equant corundum grains suspended in a hydrous haplogranitic melt. The experimental data document increasing relative viscosity with increasing crystal fraction, shear thinning, and strain dependent viscosity decreases through textural reorganization. They present a comprehensive rheological dataset and derived an empirical set of equations by combining the experimental data with literature values on dilute suspensions of spherical particles. The resulting rheological model describes the interdependent effects of crystal volume fraction and strain-rate on the relative viscosity of two-phase suspensions of silicate melt and crystals. These span crystal volume fractions of $\Phi = 0–0.8$ and strain rates from ~10^{-3} to 10^{-6} s^{-1}. They use the model to discuss the implications of non-Newtonian rheology for magma ascent, fragmentation and degassing. An example dataset from Caricchi et al. (2007) is shown in Figure 4.8. Expansion of the investigated crystal volume fractions to a range between $\Phi = 0.16–0.76$ of equant particles presented in Champallier et al. (2008), who echoed the rheological findings of Caricchi et al. (2007) and also documented the absence of measurable yield stress and thixotropic behavior. They further stress that a complete understanding of magmatic multiphase rheology requires experiments with different shapes, sizes and aspect ratios of crystals.

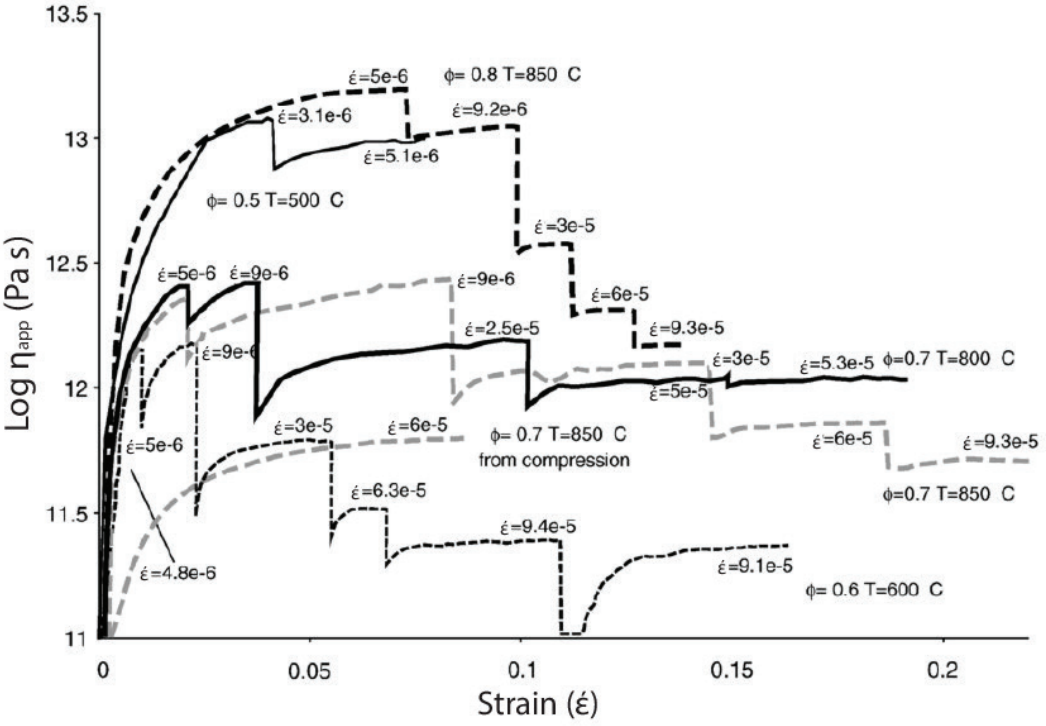

Figure 4.8. Apparent viscosities obtained from individual strain rates ($\eta_{app}=\sigma/\dot{\varepsilon}$) plotted versus strain; modified from Caricchi et al. (2007). Increasing the strain rate for any given crystal fraction (Φ) and temperature (T) induces a decrease of viscosity, which is interpreted as shear thinning behavior in Caricchi et al. (2007).

Pichavant et al. (2016) expanded the range of compositions and crystal aspect ratio for two phase melt–particle suspensions through measurements of plagioclase crystals suspended in a basaltic melt. Their results highlight the interplay between rheology and the maturation of microstructures with increasing absolute strain and the importance of crystal shape on suspension rheology. The study concludes that magmatic suspensions of plagioclase have viscosities approximately five orders of magnitude higher than suspensions of equivalent crystallinities made of isometric particles such as quartz that were presented in Caricchi et al. (2007). This discrepancy highlights the need for more systematic experimental mapping of all relevant rheological parameters to derive theoretical models describing multiphase magma rheology as a function of textural parameters (dominantly crystal-content, -shape, size distributions, pressure, and volatile content; see also the "*Parameterization Strategies"* section later in this chapter).

The first systematic investigations of three phase (crystals, bubbles and hydrous silicate melt) suspensions were spearheaded in experimental efforts using a Paterson type apparatus. This is because it allows containment of pressurized bubbles at simulated magmatic conditions. These studies highlighted significant changes in rheology between two and three phase suspensions. Pistone et al. (2012, 2013) present a series of measurements on three-phase, hydrous (2.26–2.52 wt.% H_2O), haplogranitic magmas, composed of quartz crystals ($\Phi=0.24$–0.65), pressurized CO_2-rich gas bubbles ($\Phi_b=0.09$–0.12) and melt in different proportions. The results show that three-phase magmas are characterized by a rheological behavior that is substantially different with respect to suspensions containing only crystals or only bubbles. Three-phase suspension rheology is found to be strongly strain-rate dependent (i.e., non-Newtonian). Both shear thinning and shear thickening non-Newtonian regimes were observed. Apparent shear thinning occurs in crystal-rich magmas ($\Phi=0.55$–0.65; $\Phi_b=0.09$–0.12) as a result of crystal size reduction and shear localization. Note however that viscosity reduction from crystal breakage constitutes a change in sample componentry rather than being a rheological phenomenon from textural re-organization (Cordonnier et al. 2009). Pistone et al. (2013) show

that when bubbles are retained in the suspension, the presence of limited amount of gas bubbles results in a prominent decrease in viscosity compared to the rheology of bubble-free, crystal-bearing systems, e.g., at $\Phi = 0.7$, a decrease of about 4 orders of magnitude in relative viscosity is caused by adding 10 vol% of bubbles. At intermediate crystallinity ($\Phi = 0.44$; $\Phi_b = 0.12$) both shear thickening and thinning occur. Contrary to previous data on two phase suspensions, the authors report that shear thickening prevails in dilute suspensions ($\Phi = 0.24$; $\Phi_b = 0.12$), when bubble coalescence and outgassing dominate. This highlights that crystallization and outgassing of magmatic bodies can lead to a substantial increase of viscosity inducing their "viscous death" and transition to elastic behavior. On the other hand, the significant viscosity decrease associated with limited volumes of gas can promote re-mobilization of large plutonic magma bodies and the generation of large explosive eruptions. Pistone et al. (2016) presented some further measurements on the material synthesized and characterized in Pistone et al. (2012). Based on this database they derived empirical flow laws for multiphase magmatic suspensions. Their applicability remains to be tested both experimentally as well as via numerical and field studies. The insight that degassing may profoundly affect suspension viscosity inspired several contributions that employ torsion experiments to study the viscous to brittle transition and constrain the parameters required to develop shear fracturing of particle suspensions (Cordonnier et al. 2012b) and/or bubble coalescence (Kushnir et al. 2017). Both processes act to generate permeability and facilitate outgassing (Caricchi et al. 2011; Shields et al. 2014; Kushnir et al. 2017). The available data highlight that generation of a permeable network heavily relies on brittle deformation mechanisms (i.e., melt fracturing) to generate the connectivity required for permeability development; see also (Ryan et al. 2019b). For further details please also see Wadsworth et al. (2022, this volume) and Lavallée and Kendrick (2022, this volume).

Okumura et al. (2016) performed the first high temperature viscometry experiments on natural volcanic rocks with $\Phi = 0.16–0.45$; $\Phi_b < 0.04$. They highlight that in natural samples, the effective viscosity of the magma may increase with respect to previous experimental results due to textural heterogeneity. These heterogeneities introduce local stiff regions within the sample owing to crystal interaction. This highlights that similar to small scale parallel plate viscometry, sample size is one of the main limitations of viscometry in a Paterson type apparatus.

5. FIELD RHEOLOGY

Laboratory viscometry of silicate melt or analogue material suspensions, as reviewed in the earlier sections of this chapter, provides unique information for understanding the flow dynamics of magmas and lavas. However, it has proven difficult, if not impossible, to reproduce natural conditions in the laboratory, in particular in terms of redox state, crystal- and bubble-contents, sizes, shapes and their respective distributions as well as pressure (see Section 4. *Experiments on high temperature silicate melt suspensions*). In order for the laboratory data to become relevant for the interpretation or forecasting of flow emplacement they need to be directly linked to natural settings and conditions. Numerous studies have estimated lava viscosity from the dynamics of the lava flow as a whole, using either the velocities of lava flowing within channels or at flow fronts (Nichols 1939; Krauskopf 1948; Rose 1973; Walker et al. 1973; Harris et al. 2004; James et al. 2007) or from solidified flows, using their final dimensions, e.g., (Hulme 1974; Fink and Zimbelman 1986; Moore 1987; Kilburn and Lopes 1991) However, these methods are only able to provide spatially and temporally integrated values of the flow as a whole, averaging viscosity gradients across the flow (e.g., effect of cooler surface, base and sides) and viscosity variations with time (Kolzenburg et al. 2018). Other studies have tried to provide a parameterization to link the bulk chemical composition to the rheological properties of the whole lava flow (Hulme 1974; Lev et al. 2012), which, while operationally favorable due to its simplicity, does not allow

tying the lava viscosity to the texture and temperature of the suspension itself. This has inspired several research groups to attempt direct viscosity measurements in the field, on active lava flows. These measurements of lava viscosity use specialized instrumentation and aim to capture the rheological flow curve of the lava in its natural state, including all intrinsic and extrinsic dynamics such as crystal and bubble content, temperature, oxygen fugacity etc. Such rheological field data, when associated with temperature measurement, detailed textural analyses of the samples, and dedicated experimentation in the laboratory, can provide a holistic assessment and parameterization of three-phase suspension rheology at natural conditions. However, due to the challenges associated with the development and deployment of this specialized instrumentation and the intrinsic hazards of work on active volcanoes, field rheology data remain very scarce; see Chevrel et al. (2019a) for a detailed review.

The success of field rheology campaigns is fundamentally controlled by the eruptive dynamics of the volcano, accessibility of the flow as well as external conditions (e.g., weather). While an eruption might be in progress and the infrastructure may be available, field measurements are not always possible, as direct approach to and contact with active lava are required. All the aforementioned conditions must be favorable to perform accurate and reproducible field rheometry. A further complication arises from the fact that, working in a dynamic environment like active lava implies that the lava is continuously changing (e.g., cooling, crystallization, degassing) and hence stable conditions are rarely encountered.

Current field rheology data is restricted to low silica content lava (<55 wt. %) and low crystal contents $\Phi < 0.45$. This is largely due to their relatively low viscosity at eruption temperatures ($< 10^6$ Pa s). However, an important limitation even in low viscosity systems is the rapid cooling of the lava surface. The time of the measurement therefore needs to be shorter than crust formation. Lavas of higher viscosity have not been measured to date because of the extremely challenging conditions of approach. High viscosity lava flows are usually ‘a’ā to block types with an outer, fragmented, surface that makes it extremely difficult to access the molten interior. Further, the time required to measure high viscosities may expose the operator to risks from falling blocks. Lastly, there are currently no instruments available for measuring at sufficiently high torque. Due to this mechanical limitation, the devices employed in the studies reviewed below were so far only able to access a narrow range of flow types (i.e., pahoehoe lobes and stable small lava channels).

In over 60 years (1948 to 2019), only eleven studies on field lava rheology measurements have been published (Einarsson 1949; Shaw et al. 1968; Gauthier et al. 1973; Pinkerton and Sparks 1978; Panov et al. 1988; Pinkerton et al. 1995a,b; Pinkerton and Norton 1995; Belousov and Belousova 2018; Chevrel et al. 2018). Two types of instruments have been used; both are derived from methodologies applied in laboratory rheometry: 1) penetrometers, where a penetrating body is pushed into or onto the lava by applying an axial force; this method is commonly used for relatively high viscosity lavas ($>10^3$ Pa s) and 2) rotational viscometers, analogous to the concentric cylinder method, where a measurement body is pushed into the lava and then rotated; this method is commonly used for lower viscosity lavas ($<10^4$ Pa s). The penetrometer method is either based on calculation of the viscous drag following Stokes’ law (falling sphere theory) for penetrometers with semi-spherical heads (Panov et al. 1988; Belousov and Belousova 2018) or viscosity is obtained from calibration of the relationship between the penetrating force, the speed of penetration and fluid viscosity of a known liquid (Einarsson 1949, 1966; Gauthier et al. 1973; Pinkerton and Sparks 1978). Penetration rheometry has also been employed to measure the apparent yield stress of lava by recording the minimum force required to initiate movement (Pinkerton and Sparks 1978). Rotational viscometers, like in the laboratory, involve a rotating spindle immersed into the lava and viscosity is obtained from the wide-gap concentric cylinder theory (see the *Experiments on high temperature silicate melt suspensions* section earlier in this chapter for details).

Low carbon stainless steel alloys have proven most suitable for construction of both types of field rheometers because they are highly resistant to both mechanical stress and thermal exposure, readily available, and reasonably cost-effective. Although the use of steel may potentially cause iron contamination of the lava, the degree of contamination is considered to be insignificant due to the much shorter timescale of the measurements with respect to the diffusion speed of iron in silicate melts. Initial attempts to measure the viscosity of lava used crude instruments (such as forcing a rod by hand into flowing lava), and even the latest instruments (motor-driven rotational viscometer) are significantly less refined than those one would encounter in a well-equipped laboratory. This highlights that advances in instrumentation are still required to advance field rheology to a point where it can become a routine technique for parameterization of natural magmatic suspensions.

Falling sphere

To date, the falling sphere method was employed only once by Shaw et al. (1968) for measurements in the Makaopuhi lava lake. A stainless-steel sphere (2.5 cm diameter) was attached to a fine stainless-steel wire that was passed through a drill hole in the thick, solidified surface of the lava lake. The sphere was released into the lava in its hottest part and the movement of the wire (velocity and distance of penetration) behind the descending sphere was measured to calculate the viscosity via Stokes law. The strain rate during measurement was as low as 0.004 s^{-1} given the settling velocity of 3.5×10^{-3} cm/s. The viscosity is reported as 10^3–$10^{3.25}$ Pa s. This method could only be employed on a stable lava lake of sufficient depth, and with a suitably thick crust to support the measurement system.

Penetrometers

Penetrometers have been employed from the first published measurement by Einarsson (1949) until recently Belousov and Belousova (2018). This type of instrument is advantageous because it is light, easily transportable to the field, easy to build (the simplest versions consist of a rod equipped with a force gauge) and permits quick measurements over a wide range of viscosity (10^3–10^7 Pa s). The three kinds of penetrometers used to date are: 1) the simple penetrometer consisting of a pole pushed into the lava by hand, 2) the ballistic penetrometer that is a spear shot with a crossbow into the lava, and 3) the dynamic penetrometer that operates by propelling a piston once it has been placed inside the molten lava.

Simple penetrometers, where a rod is thrust by hand into the lava, allow the operator to qualitatively assess the viscosity during the measurements from to the amount of force and the time needed to penetrate the lava. In low viscosity lava, the rod may sink under its own weight while for higher viscosity the operator needs to apply the entire body weight to push the rod into the lava. Quantification of viscosity has been established via a relationship between viscosity and velocity of penetration from repeated measurements of fluid with known viscosity (Einarsson 1949; Pinkerton and Sparks 1978). More advanced penetrometers are equipped with a force gauge to record the force applied on the rod and designed with a semi-spherical head (Fig. 5.1B). Neglecting the potential effect of lava sticking to the rod, the viscosity of the fluid equates to the viscous drag on a half sphere that can be obtained via Stokes' law, given the force acting on the penetrating rod advancing through a viscous medium is known (Panov et al. 1988; Belousov and Belousova 2018):

$$\eta_{app} = \frac{F}{3\pi u R_{eff}} \tag{5.1}$$

where F is the force of penetration (viscous drag), u is the speed of penetration, and R_{eff} is the effective radius of the rod.

The ballistic penetrometer was used only once and involves shooting a spear at high-velocity perpendicularly into the lava and measuring its penetration depth (Gauthier 1971; Gauthier et al. 1973). The viscosity measurement relies entirely on previous laboratory

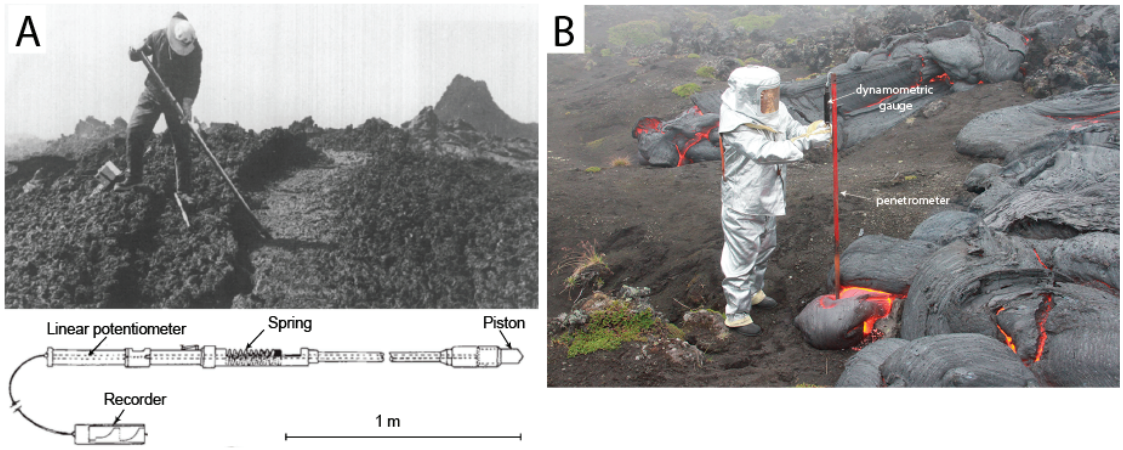

Figure 5.1. Field penetrometers: **A)** Photo and sketch of the dynamic penetrometer employed by Pinkerton and Sparks (1978); **B)** simple penetrometer with dynamometric gauge (Belousov and Belousova 2018).

calibration of the same spear geometry on liquids of different viscosities. The high initial penetration velocity prevents lava advance rates from influencing the measurement and limits cooling of the lava around the spear during penetration.

The disadvantage of simple and ballistic penetrometers is that the viscosity is an integrated value of the lava properties from the cooler surface of the flow to the hotter core. The measurements are therefore biased by the higher force required to penetrate the more viscous outer layer. Thus, this type of penetrometer tends to provide a semi-quantitative measurement of the rheology of the cooler exterior of a flow, and little indication of the rheological characteristics of the hot interior. To overcome this issue, Pinkerton and Sparks (1978) introduced the dynamic penetrometer (Fig. 5.1). It consists of a piston that is protected from the cooler crust by an outer stainless-steel tube. Once it is passed through the lava crust and has reached thermal equilibrium with the surrounding lava, penetration is activated (i.e., only the tip of the penetrometer is moving forward). This penetrometer was equipped with a pre-compressed spring to provide a controlled force during penetration which is recorded together with the piston advance rate. These data can then be converted into shear stress and strain-rate measurements (Pinkerton and Sparks 1978).

Another approach was proposed by Belousov and Belousova (2018) who measured the viscosity profile across small pāhoehoe lobes (Fig. 5.1B). To do so, they recorded the speed of penetration under a constant load from the surface to the base of the lobe. This enabled them to document the higher viscosity at the lobe surface, which quickly decreases directly below the skin, reaching a minimum in the interior of the lobe and then increases again toward the base.

Rotational viscometers

Two types of rotational viscometers have been employed in the field: a fixed rig installed on the frozen surface of a lava lake with a rotating spindle lowered into the molten core and controlled rotation rate, Fig. 5.2A; Shaw et al. (1968) and a portable instrument with a strain-rate controlled spindle inserted into the lava (Figs. 5.2B and 5.3); (Pinkerton and Sparks 1978; Pinkerton 1994; Pinkerton et al. 1995a; Chevrel et al. 2018). Both types of rotational viscometers rely on wide-gap concentric cylinder theory, where the torque is converted into shear stress and the rotational velocity into strain-rate using Couette theory and the spindle geometry (Dingwell 1986; Spera et al. 1988); see also Section 4. Equations (4.1) and (4.2). Unlike most laboratory experiments where the immersed spindle is cylindrical, vane geometry (i.e., four orthogonal blades; see Fig. 5.2B) is favorable for use in the field due to 1) lower weight, 2) ease of penetration, 3) reduced disturbance of lava during insertion, 4) reduced slippage between the edge of the vane and the lava (Shaw et al. 1968). The material between the vanes is trapped, forming a virtual cylinder of sample material whose equivalent diameter is used for viscosity calculation (Eqns. 4.1 and 4.2).

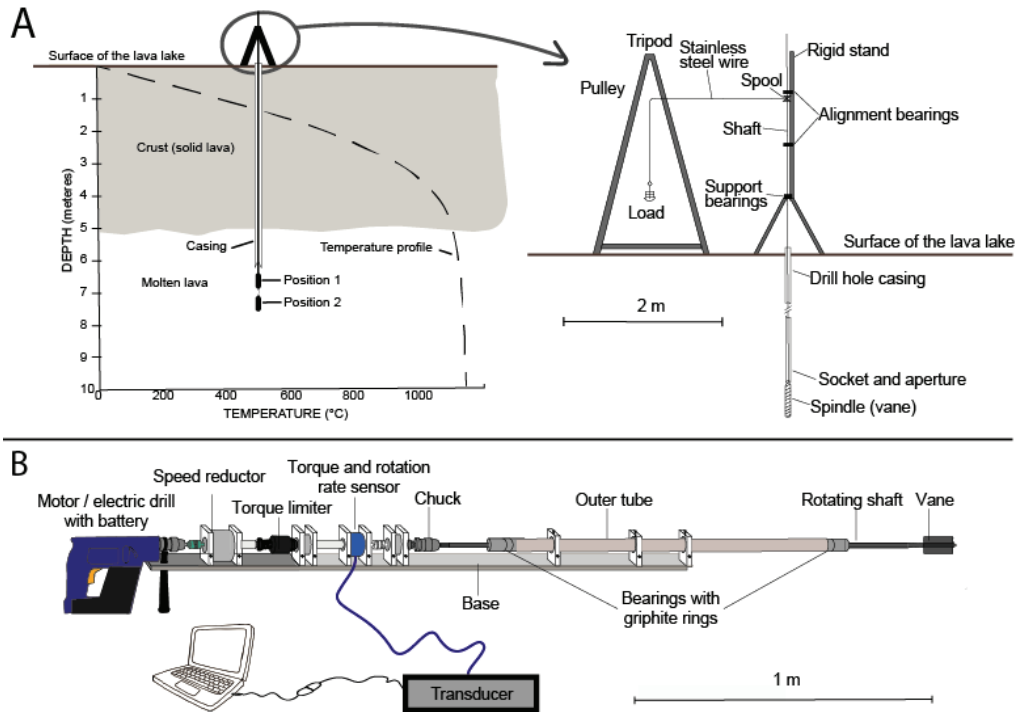

Figure 5.2. Sketch of a fixed rotational viscometer **(A)** ; modified from Shaw et al. (1968) and a motor-driven rotational viscometer **(B)** employed in Pinkerton et al. (1995b) and Chevrel et al. (2018).

The fixed rotational viscometer can only be used in the unique setting where a thick, frozen, stable surface is available for installation (Fig. 5.2A); (Shaw et al. 1968). The experimental setup consists of a fixed stand with a rotating shaft and vane attached to its lower end that is lowered vertically into the lava (Fig. 5.2A). A wire is spooled to the shaft, passed through a pulley mounted on a tripod and attached to a load. This permits to pull the wire and to rotate the shaft. By changing the load weight, different rotational torques can be applied to the vane. Flow curves are then obtained by measuring the resulting rotational speed.

Portable rotational viscometers have been used several times and the design has evolved over the years from manually activated to motor-driven (Fig. 5.3). The manually activated shear vane consists of a stainless steel vane attached to a torque wrench (Fig. 5.3A), which allows yield stress to be measured by applying torque slowly until the shear vane begins to rotate (Pinkerton and Sparks 1978). This system was also used to measure viscosity over a range of strain rate by monitoring the rotation speeds via an optical tachometer (Pinkerton and Norton 1995). The first motor-driven rotational viscometer consisted of a rotating steel vane attached to a drill hammer (Fig. 5.3B). The torques measured at different rotation rates (monitored with optical tachometer) are recorded using a torque meter, mounted coaxially between the drive train and the shear-vane. This device had a relatively low torque limit and was employed on natrocarbonatite lavas at Oldoinyo Lengai by (Pinkerton et al. 1995a). The second generation of motor-driven rotational viscometers was modified for silicate lavas (that have higher temperature and higher viscosity than natrocarbonatite lava). The motor is connected to a reduction gearbox, equipped with a torque limiter (to not break the instrument) and a new, combined, torque-rotation rate sensor (Figs. 5.2b, 5.3c,d). This viscometer has the capacity of varying the rotational speed; and thus to apply a large range of strain rates (0.2–3 s^{-1}) (Pinkerton 1994; Pinkerton and Norton 1995). The range of applicable strain rates is limited by the machine's torque range (< 2 N) and vane geometry and results in a range of stresses of 100–1000 Pa. By changing the torque sensor to a higher torque range of the same instrument, Chevrel et al. (2018) were able to reach higher stresses (up to 2500 Pa) and strain rates (up to 6 s^{-1}) but the lower strain-rate limit was consequently increased to 1 s^{-1} given the lava viscosity and the vane geometry.

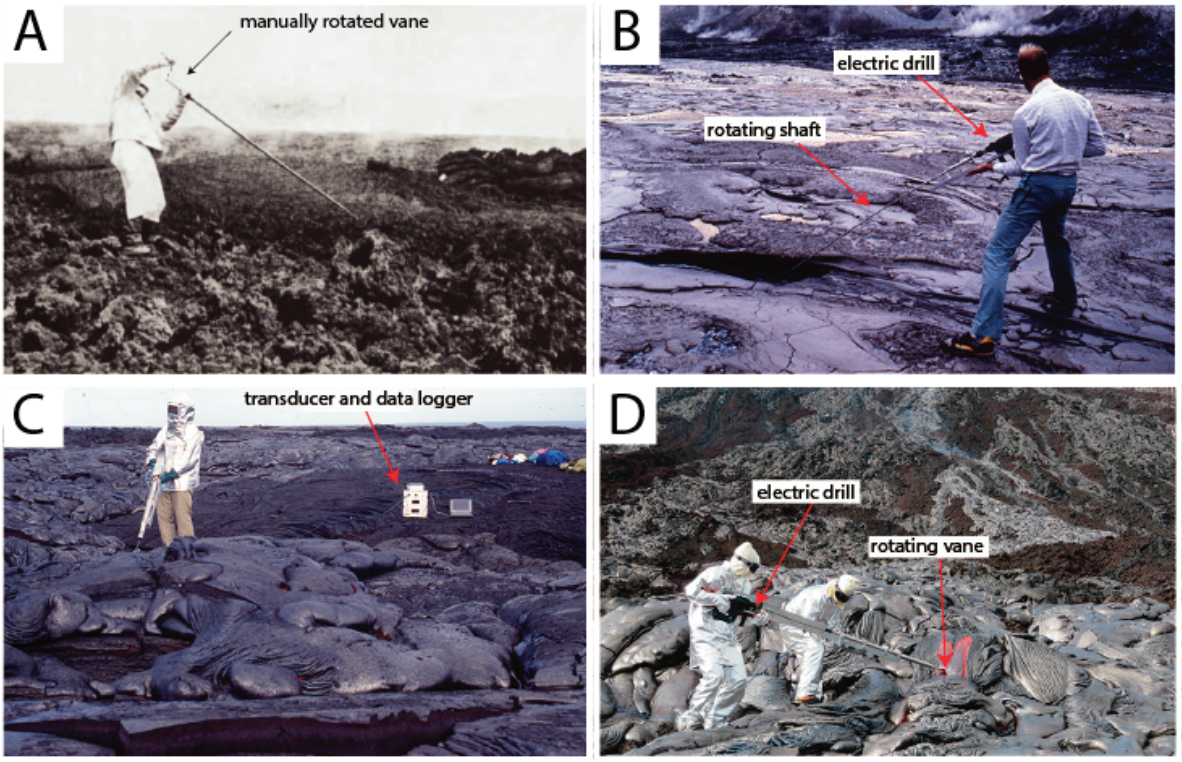

Figure 5.3. Photographs of all generations of portable rotational viscometers; **A)** manual rotational viscometer; photo from Chester et al. (2012); **B)** first motor-driven rotational viscometer employed on natrocarbonatite lavas employed by Pinkerton et al. (1995a); **C)** first measurements of the motor-driven rotational viscometer on pāhoehoe lavas by Pinkerton (1994) **D)** latest measurements using the motor-driven rotational viscometer on pāhoehoe lavas by Chevrel et al. (2018). Figure modified from Chevrel et al. (2019a).

Toward parameterization: requirements for future field viscometry

Field viscometry must always be performed in combination with temperature measurements and lava sampling. This is because the subsequent textural and petrographic analyses of these samples and data are key to understanding how crystal and bubble content affect rheology during lava emplacement. The molten lava must be sampled and quenched rapidly to conserve the texture at the location of measurement. In order to use field rheometry to its full potential for mapping of lava rheology in 4D throughout an entire lava flow, future field campaigns should combine measurements of rheological properties, temperature and lava texture as a function of distance from the vent to the front and across the flow. This likely also requires multiple field rheometers to be deployed synchronously in order to resolve the lava flows' rheology in 4D.

Recently Chevrel et al. (2018) showed that field viscosity measurements could not be readily compared with sub-liquidus laboratory measurements on natural lavas because the shear stresses acting during lava flow emplacement are, so far, mechanically inaccessible in the laboratory. Further, experiments performed in the laboratory tend to overestimate viscosity at a given temperature because of the shift of crystallisation toward higher temperature due to lack of volatiles in the melt, experimentation at ambient pressure and oxygen fugacity, as well as the dynamic thermal and chemical disequilibrium present during lava flow on the surface. Facilitated by the combined measurement of viscosity, temperature and petrology, Chevrel et al. (2018) further show that volatile and bubble content must be considered if the viscosity of active lava should be estimated via combined rheological and petrological models. They state, that to reproduce the field viscosity measurement using available models (see section "*Parameterization Strategies"*), three-phase parameterisation with 50% bubbles and 15% crystals is needed. Good agreement between field measurement and model-based viscosity estimation is obtained when considering elongated crystals (aspect ratio of 2.4) and deformed bubbles (Ca $\gg$1) (see section *Parameterization Strategies"* for details).

Reducing errors associated with field measurements requires accurate sensors as well as meticulous setup and calibration, which is difficult to achieve in the field where conditions are more dynamic and less controlled than in the lab. Field measurements will always be constrained by the balance between measurement machinery and the lava's thermodynamics. To reduce the effects of crust formation during measurements the instruments need to be pre-heated and inserted into fresh, molten lava through emerging breaches in the crust, or at the breaking point of pāhoehoe lobes where little-to-no crust is present. Further, the measurement timescale needs to be shorter than the timescale of cooling and crust formation. Both issues may be minimized by employing a dynamic penetrometer (Pinkerton and Sparks 1978), which allows triggering the sensor once the lavas isothermal core is reached. These are, however, limited to a specific range of stress–strain-rate conditions (See Fig. 5.4).

Figure 5.4 further highlights the current gaps in achievable measurement conditions. The development of the next generation of field rheometers thus needs to address several core issues. They need to be robust, light enough to be carried over rough ground and to remote locations, easily mounted and easy to handle (ideally by one person). Additionally, in order to capture the full rheological behavior of lava, field rheometers need to be able to apply a range of stress–strain-rate combinations. Current limitations include low strain rates ($<1\,s^{-1}$) and low shear stresses (< 200 Pa). The aforementioned issues place high demands on the dimensions of the shear vane or spindle, torque sensor capability and motor power. The technological advances since the early measurements (e.g., electronically controlled motors and sensors) make the development of a new generation of rotational viscometer the most suitable approach for future measurements on active lavas. Combination of several methods is the most promising approach to recover a more complete rheological map and to describe the full flow curves for natural lavas. An attempt to measure the variation of viscosity over a large range of strain rate for Hawaiian lavas, obtained via field viscometry, is presented (Chevrel et al. 2018) and revealed a shear-thinning behavior.

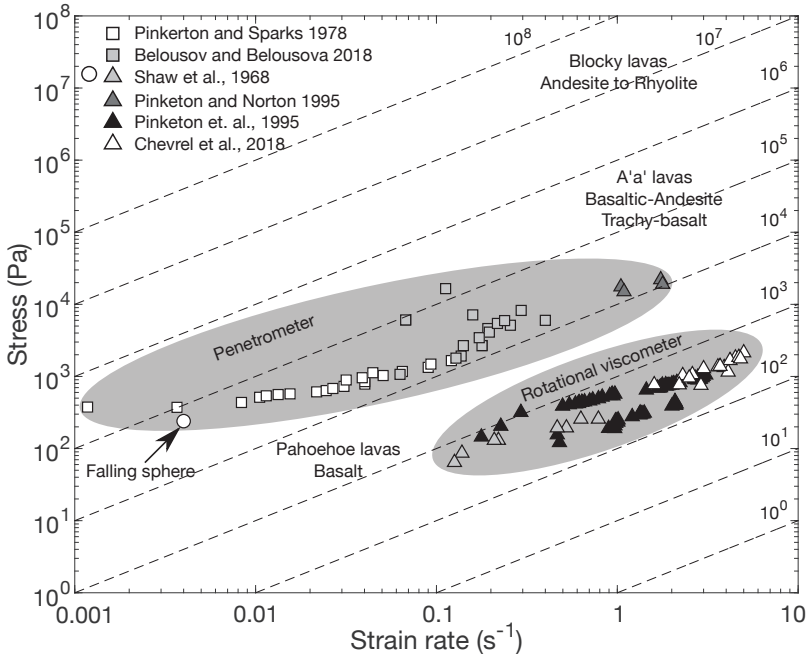

Figure 5.4. Regime plot of stress vs strain rate, mapping the measurement capacities of field rheometers. The plot shows the domains where lava viscosity has been measured with current hardware (**shaded areas**). It is important to state that neither method (rotational or penetration) is superior to the other but instead, they are to be regarded as complementary and employed depending on the viscosity regime that is encountered in the field. **Dashed lines** are iso-viscous conditions, **squares** and **triangles** represent data acquired with penetrometers and rotational viscometers, respectively. The **highlighted circle** represents the only data acquired by falling sphere method.

6. PARAMETERIZATION STRATEGIES

A central goal of most of experimental rheology is to generate predictive models that describe the rheology of multiphase suspensions as a function of extrinsic (temperature, shear rate, etc.) and intrinsic (melt- and crystal-composition, texture etc.) parameters. After reviewing the broad range of experimental approaches on both analogue and natural materials we now review the strategies for parameterization of the derived data that aim to generate a systematic understanding of multiphase magma and lava rheology. Parameterization of the data recovered from analogue, high-temperature and field experimentation has largely advanced in parallel with the increasing availability of experimental data. Thus, the derived models are intimately tied to the experimental approaches and have evolved predominantly as parameterization strategies for two phase suspensions of either particle- or bubble-suspensions and few attempts of the description of three-phase flow have been presented.

This review of parameterization strategies rides on the nomenclature introduced in the overview of common ways to describe rheological data that was presented in the first two sections of this chapter. Here we first presented parameterization efforts for particle suspensions, followed by those for bubble suspensions and finally those for three-phase suspensions. These models and the underlying physics are dominantly developed on the basis of data derived from analogue experiments, since these have produced the most complete and well constrained datasets for all relevant variables. The strategies reviewed here are focused on parameterization of shear viscosity. Multiphase suspensions may, however, also deform under tensile or compressive stresses, where the effects of volume viscosity become important. In such cases, longitudinal or bulk viscosities are defined that are products of volume and shear viscosities (see the "*Conventional descriptions of rheological data*" section). Also, note that due to the extremely narrow range of applicability of empirical, petrological approaches that relate relative viscosity to temperature as they were presented for example in Shaw (1969) or Dragoni and Tallarico (1994) we do not include them in this review.

Particle suspensions

In crystalline suspensions, the crystal phase or phases act as non-deformable particles which increase the suspension viscosity via both hydrodynamic effects (the melt has to flow around and between the particles) at low particles volume fraction (Φ) and mechanical interaction among particles at intermediate to high Φ. For low particle fractions (i.e., in the dilute regime) it is recognized that suspensions maintain a Newtonian character (i.e., a linear stress–strain-rate relationship). Within increasing particle fraction, once moving beyond a certain Φ threshold (that varies between 0.05 and 0.25, depending on the particle aspect ratio and surface roughness), suspensions becomes non-Newtonian, commonly exhibiting shear thinning behavior. Once Φ is sufficiently large (semi-dilute to concentrated regime), particles start to interact with each other and may align themselves with the flow direction or form force chains, resulting in a stronger shear thinning behavior and/or the development of an apparent yield stress (at $0.25 \lesssim \Phi \lesssim 0.6$). When the maximum packing fraction (Φ_m) is reached at even higher particle concentrations (concentrated regime) the particles may develop a solid interlocking network, which causes a drastic increase in the effective viscosity of the suspension and initiates the transition from suspension to creep rheology (Kohlstedt and Zimmerman 1996; Petford 2003; Lavallée et al. 2007).

Parameterization of the relative suspension viscosity η_r

The increase of viscosity and the evolution from Newtonian to non-Newtonian behavior during crystallisation depend fundamentally on the crystal content, shape, surface texture, and size distribution as well as the imposed strain rates. The development and nature of non-Newtonian behavior then result from the nature of particle–particle interaction during flow. Early empirical models consider the dilute regime (i.e., $\Phi \lesssim 0.25$) where particle interactions are limited. They are able to reproduce the measured relative viscosities of a broad range

of suspensions with varying particle shapes, size distributions and surface properties very accurately and prove impressively robust within their Φ limits. These models are founded on the work of Einstein (1906) who first described the relative viscosity of suspensions of solid spheres (Eqn. 6.1, Table 6.1). The goodness of fit of this model was later improved for a larger dataset by Guth and Gold (1938) using a second degree polynomial function (Eqn. 6.2, Table 6.1) and by Vand (1948) using an exponential term (Eqn. 6.3, Table 6.1). However, these models break down once the particle volume fraction exceeds the dilute regime, as they do not account for the effects of particle–particle interaction (Fig. 6.1). The first model aiming to capture the onset of the concentrated regime was presented by Roscoe (1952) (Eqn. 6.4, Table 6.1). This model, often called the Einstein–Roscoe equation, was frequently used for the study of magmas and lavas over the last decades (Shaw 1965; Marsh 1981; Murase et al. 1985; Ryerson et al. 1988; Pinkerton and Stevenson 1992). While these pioneer models are based on data for suspensions of solid spheres, their fitting parameters can be modified to capture variations in particle shapes and size dispersions as well.

Subsequent parameterization strategies aimed to capture the effects that arise in the semi-dilute regime ($\Phi < \Phi_m$). These describe particle suspension viscosity as a function of the relation between the volume fraction of suspended particles and a maximum particle volume fraction. The assumption is that when Φ_m is reached, there is no longer enough "free space" for particles to move past each other, causing the particle population to become "jammed", generating a rigid framework and thus the suspension becomes un-deformable with an infinite viscosity, Φ_m. These models are largely based on the work of Eilers (1941) and predict infinite viscosity at $\Phi = \Phi_m$ (Eqn. 6.5, Table 6.1). The model of Eilers (1941) was later simplified by Maron and Pierce (1956) (Eqn. 6.6, Table 6.1) and expanded by Krieger and Dougherty (1959) to include a shape dependent Einstein coefficient B (Eqn. 6.7, Table 6.1). The latter two equations serve as the base for a number of other proposed models (Eqns. 6.8–6.13, Table 6.1) (Gay et al. 1969; Chong et al. 1971; Wildemuth and Williams 1984; Shapiro and Probstein 1992; Faroughi and Huber 2015; Moitra and Gonnermann 2015). The fitting parameters in these models are dependent on particle shape and surface roughness, which are usually well defined in analogue experiments (Mueller et al. 2010; Mader et al. 2013; Klein et al. 2018) but difficult to quantify for natural magmatic suspensions. The model complexity varies largely as a function of the experimental data that the authors aim to describe.

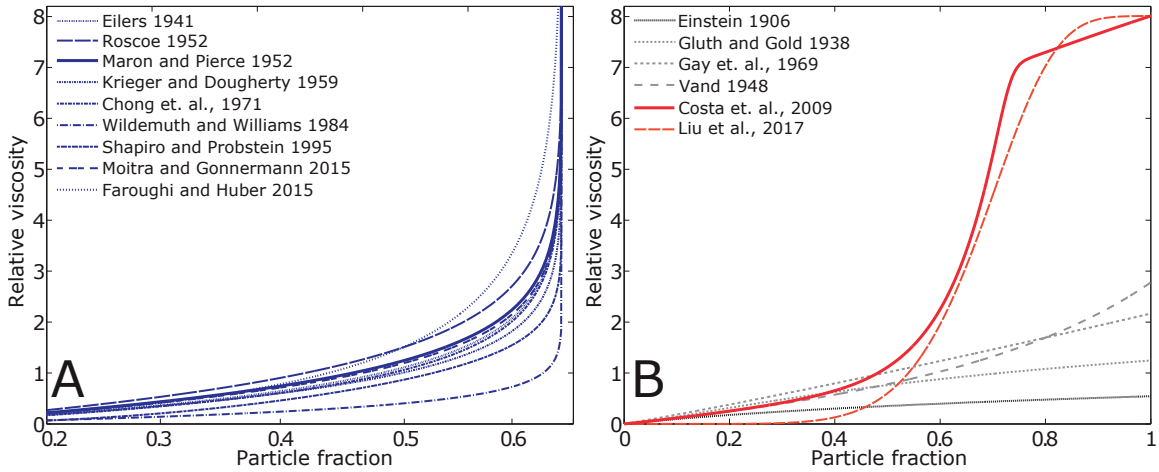

Figure 6.1. Examples of models of particle suspension rheology. **A)** models predicting a complete rheological lock-up at $\Phi = \Phi_m$ plotted for $\Phi_m = 0.65$ using the equations given in Table . Note that for Roscoe (1952) (Eqn. 6.4) this means R=1.58. **B)** models without rheological lock-up using the equations given in table 6.1. For Costa et al. (2009) (Eqn. 6.14) we plot the model with $B = 2.5$, $\Phi_* = 0.65$, $\alpha = 5$, $\delta = 13 - \alpha$ and $\xi = 10^{-4}$) and for Liu et al. (2017) we plot the model for $k = 10$, $n = 7$ and $\eta_{r(max)} = 8$.

Table 6.1. Equation for parameterization of the relative viscosity due to solid particles. All variables are defined in Table 1.1. equation numbers in the original publications are reported with the reference.

Equation	Reference	Comment	Eqn.
$\eta_r = 1 + B\Phi$	Einstein (1906; p.300)	For dilute particle content ($\Phi < 0.25$) with B= 2.5 for spheres	(6.1)
$\eta_r = 1 + B\Phi + B_1 \times \Phi^2$	Guth and Gold (1938)	For dilute particle content ($\Phi < 0.25$) with B= 2.5 and B_1=14.1 for spheres	(6.2)
$\eta_r = e^{\frac{B\Phi}{1-\alpha\Phi}}$	Vand (1948; Eqn. 6.8)	With α = 0.60937	(6.3)
$\eta_r = 1 - R\Phi^{-2.5}$	Rosecoe (1952; Eqn. 3)	With $R = \frac{1}{\Phi_m} = 1.35$ for spheres	(6.4)
$\eta_r = \left(1 + \frac{1.25\Phi}{1 - \Phi / \Phi_m}\right)^2$	Eilers (1941; pp.321)		(6.5)
$\eta_r = \left(1 - \frac{\Phi}{\Phi_m}\right)^{-2}$	Maron and Pierce (1956; Eqn. 30)		(6.6)
$\eta_r = \left(1 - \frac{\Phi}{\Phi_m}\right)^{-B\Phi_m}$	Krieger and Dougherty (1959; Eqn. 27)	With B = 2.5 for spheres but can be fitted for other particle shapes	(6.7)
$\eta_r = \exp\left\{\left[\left(2.5 + \frac{\Phi}{\Phi_m - \Phi}\right)^{\alpha}\right] \times \frac{\Phi}{\Phi_m}\right\}$	Gay et al. (1969; Eqn. 19)	With α = 0.48	(6.8)
$\eta_r = \left(1 + \alpha \frac{\frac{\Phi}{\Phi_m}}{1 - \frac{\Phi}{\Phi_m}}\right)^2$	Chong et al. (1971; Eqn. 1)	With α = 0.75	(6.9)

Equation	Reference	Comment	Eqn.
$\eta_r = \frac{1}{\left(1-\frac{\Phi}{\Phi_m}\right)^{\Phi_m}}$	Wildemuth and Williams (1984; Eqn. 1)		(6.10)
$\eta_r = 1+\frac{3\pi}{8}\frac{\beta}{\beta+1}\left(\frac{3+4.5\beta+\beta^2}{\beta+1}-3\left(1+\frac{1}{\beta}\right)\ln(\beta+1)\right)$	Shapiro and Probstein (1992; Eqn. 1)	With $\beta = \frac{\left(\frac{\Phi}{\Phi_m}\right)^{\frac{1}{3}}}{1-\left(\frac{\Phi}{\Phi_m}\right)^{\frac{1}{3}}}$	(6.11)
$\eta_r = \left(1-\frac{\Phi}{\Phi_m}\right)^{-\alpha}$	Moitra and Gonnermann (2015; Eqn. 13)	With α= 1.92	(6.12)
$\eta_r = \left(1-\frac{\Phi_m-\Phi}{\Phi_m(1-\Phi)}\right)^{-\frac{2.5\Phi_m}{1-\Phi_m}}$	Faroughi and Huber (2015; Eqn. 46)		(6.13)
$\eta_r = \frac{1+\varphi^{\delta}}{\left[1-\Phi_*\right]^{B\Phi_*}}$	Costa et al. (2009; Eqn. 1 + 2 +6)	With: $\Phi_* = (1-\xi)\times\mathrm{erf}\left[\frac{\sqrt{\pi}}{2(1-\xi)}\varphi\left(1+\varphi^{\gamma}\right)\right]$ $\varphi = \Phi/\Phi_*$, and ε, γ, δ, Φ_* are fitting parameters	(6.14)
$\eta_r = \eta_{r(max)}^{\frac{1-\exp(-k\Phi^n)}{1-\exp(-k)}}$	Liu et al. (2017; Eqn. 6)	$\eta_{r(max)}$ is the relative viscosity of the suspension at complete solidification i.e., Φ = 1 *k* and *n* are fitting parameters	(6.15)

All these models produce satisfactory fits to most experimental data in the dilute and semi-dilute regime but are not appropriate for concentrated magmatic suspensions because they cannot assess viscosity for particle concentrations above Φ_m, where they tend to infinity. However, it is documented that materials are able to flow even when $\Phi > \Phi_m$, because Φ_m increases as particles align during flow, or when the particle size distribution is polydisperse (space between large particles can be filled with smaller particles). In such cases (high particle fraction suspensions; Φ = 0.5–0.8) the rheological response is primarily dictated by the crystal phase and phase-assembly while the importance of the interstitial melt is reduced. This observation implies that models for dilute suspensions will break down for suspensions of $\Phi \gtrsim 0.6$ (Lejeune and Richet 1995; Lavallée et al. 2007) because the materials are still able to flow at $\Phi > \Phi_m$ and hence their viscosity cannot be infinity. Further, experimental data document that even solid materials are able to deform via creep when Φ = 1. Therefore, a more complete rheological model has to encompass rheological transitions from a low relative viscosity regime, where the rheology is determined by the suspending liquid, to a high viscosity regime where the effect of particles dominates.

Such a parameterization approach was first introduced for magmatic suspensions in Costa (2005). On the basis of this model, Caricchi et al. (2007) developed an empirical characterization describing the non-Newtonian, strain-rate-dependent rheological effects of particles in the range of Φ = 0–0.8 that is based on experimental data obtained via torsion experiments on synthetic silicate melt suspensions (see the "*High temperature experiments"* section). They provide a 3D equation for the Φ–$\dot{\varepsilon}$ dependence of the viscosity of partially crystallized magmas by fitting their experimental data to the model of Costa (2005). The Costa (2005) model was subsequently improved and generalised into a more comprehensive model in Costa et al. (2009) (Eqn. 6.14, Table 6.1), which has found frequent application in a range of studies concerning the rheology of geomaterials (Jamieson et al. 2011; Mandler and Elkins–Tanton 2013; Bachmann and Huber 2016; Cashman et al. 2017). The complex nature of the model stems from its goal to describe the entire range of Φ = 0–1 and deserves some more detailed consideration. The Costal et al. (2009) model is calibrated on analogue suspensions of particle fractions, between Φ = 0.1–0.8 and describes the relative viscosity increase of two-phase mixtures as a sigmoidal curve that initially increases exponentially until reaching a critical particle fraction, beyond which the exponential increase decays (Fig. 6.1B). This model is the first to cover the transition from the regime where the deformation behavior is controlled by melt viscosity up to the beginning of the regime where the deformation behavior is controlled by a solid framework of interlocking particles and is the most complete description of particle suspension rheology to date. Nonetheless, this model still requires characterization of fitting parameters as a function of particle size and shape as well as their respective distributions (Eqn. 6.14, Table 6.1). One of these parameters is defined as the critical solid fraction at the onset of the acceleration of viscosity (Φ_*). Another parameter (γ) describes the rate of relative viscosity increase with particle volume fraction, as $\Phi \rightarrow \Phi_*$; and the increase of η at $\Phi > \Phi_*$ is then expressed in terms of $\delta = A - \gamma$ with A = 13 as an empirical constant. ξ is an empirical fitting parameter commonly $\ll 1$ that allows optimization of the model for a given dataset. For large Φ, the second term in the numerator is a minute correction when $\Phi < \Phi_*$, while it becomes important when $\Phi > \Phi_*$. At $\Phi = \Phi_*$, the relative viscosity depends on Φ and Φ_*, only. With decreasing Φ at $\Phi < \Phi_*$, the model (Eqn. 6.14, Table 6.1) tends to the Krieger and Dougherty (1959) equation (Eqn. 6.7, Table 6.1) and when $\Phi \rightarrow 0$, it recovers the Einstein (1906) equation (Eqn. 6.1, Table 6.1).

Recently, Liu et al. (2017) proposed a simpler parameterization approach aimed at covering the range of Φ = 0–1. The model is based on a sigmoidal function and only requires three fitting parameters (Eqn. 6.15, Table 6.1). While this model is attractive due to its flexibility, simplicity and low number of fitting parameters, it does not lend itself for easy expansion to incorporate the details of variations in particle aspect ratio or polydispersity.

Using the Costa et al. (2009) model, this could be done by combining the Φ/Φ_* term with the empirical data of for example Mueller et al. (2010) or Klein et al. (2018). Nonetheless, both models of Costa et al. (2009) and Liu et al. (2017) remain to be validated by a complete rheological dataset covering the entire range of $\Phi = 0–1$.

Capturing polydispersity in relative viscosity models. An important issue that remains to be addressed in the models reviewed above is the fact that natural magmatic suspensions most frequently contain microlites in association with larger phenocrysts. This polydisperse distribution can act to moderate the onset of non-Newtonian effects because they are directly tied to the size and shape of the suspended particles and their respective distribution. Thus, a reasonable prediction of the relative viscosity of particle suspensions requires the consideration of particle volume fraction as well as their shape- and size-distribution.

Early work on bidisperse suspensions by Farris (1968) proposed that polydisperse suspensions may be treated as an incremental system where the coarse solid fraction acts as a monodisperse suspension in a separate, monodisperse fluid containing the finer particles. Farris (1968) considered a bidisperse system, where coarser and finer fractions have the same shape and behave independently of each other and proposed the following treatment:

$$\eta_r = \left(\frac{\eta_f}{\eta_l}\right)\left(\frac{\eta_c}{\eta_f}\right) \tag{6.16}$$

where η_l, η_f and η_c are the liquid viscosity, fine particle suspension viscosity, and coarse particle suspension viscosity, respectively (i.e., the finer grained suspension is treated as the effective medium; see the end of this section for details).

Cimarelli et al. (2011) used analogue experiments to measure the rheology of suspensions with bimodal particle size and shape distributions and show that increasing the relative proportion of prolate to equant particles at constant Φ can increase the relative viscosity by up to three orders of magnitude. Based on their data, they expand the modeling approach of Costa et al. (2009) for a variety of bidisperse suspensions. Their parameterisation rides on a variable that, instead of representing the monodisperse particle content (Φ), considers the ratio of fine (Φ_f) to coarse (Φ_c) particles $x = \dfrac{\Phi_f}{\Phi_f + \Phi_c}$: to modulate the fitting parameters of Costa et al. (2009). They report thefollowing parameterization to Equation (6.14):

$$\Phi_* = \Phi_{*f} x^{\alpha} + \Phi_{*c}\left(1-x\right)^{\alpha} \text{ with } \alpha = 1.34 \tag{6.17}$$

$$\gamma = \gamma_f x \gamma_c \left(1-x\right) \tag{6.18}$$

$$\xi = \xi_f x \xi_c \left(1-x\right) \tag{6.19}$$

The symbols are explained in Table 1.1.

Recently, Klein et al. (2018) presented a different parameterization using the Maron and Pierce (1956) model (Eqn. 6.6, Table 6.1). They substitute the shape parameter of the Mueller et al. (2010) model for Φ_m in Equation (6.25) to derive a model for polydisperse suspensions with non-spherical particles, which they then implement into the Maron–Pierce model (Eqn.6.6, Table 6.1):

$$\eta_r = \left(1-\Phi\left[1-\left(\left(1-\left\{\Phi_{m1}\exp\left[-\frac{\left(\log_{10} r_p\right)^2}{2b^2}\right]\right\}\right)\gamma^{\alpha}\right)\right]^{-1}\right)^{-2} \tag{6.20}$$

The aspect ratio r_p is defined as $r_p = \frac{l_a}{l_b}$, and l_a is the particle's axis of rotational symmetry and l_b is its maximum length perpendicular to that and non-spherical particles are approximated as prolate/oblate spheroids or cylinders (Mueller et al. 2010).

Parameterization of the maximum packing fraction. The maximum packing fraction (Φ_m) reflects the particle concentration at which the viscosity of a suspension of specific particle sizes, shapes and distributions tends towards infinity (i.e., a solid framework of interlocking particles develops and induces a transition from viscous flow to elastic or creep deformation). Φ_m is commonly determined empirically but can also be determined geometrically or numerically (Evans and Gibson 1986; Gan et al. 2004). Experimental values of Φ_m are often found to be lower than predicted from the geometrical analyses due to random heterogeneities in packing density as well as variations in packing efficiency resulting from particle roughness (Mader et al. 2013). Φ_m was found to strongly depend on particle shapes and size distributions (Cimarelli et al. 2011; Mueller et al. 2011; Klein et al. 2017)

Systematic studies have shown that for monodisperse suspensions, Φ_m decreases with particle shape anisotropy (i.e., elongate or prolate), surface roughness and decreasing particle alignment, while it increases for equant particles and polydisperse mixtures (Chong et al. 1971; Lejeune and Richet 1995; Saar et al. 2001; Caricchi et al. 2007; Vona et al. 2011; Mader et al. 2013). Often, Φ_m is determined by fitting the experimental data to rheological models like the Maron–Pierce equation (Eqn. 6.6. Table 6.1). Systematic measurement of values for Φ_m allowed derivation of empirical models that describe its dependence on aspect ratio and particle roughness (Mueller et al. 2011); Figure 6.2:

$$\Phi_m = \Phi_{m1} \exp\left[-\frac{\left(\log_{10} r_p\right)^2}{2b^2} \right] \tag{6.21}$$

where Φ_{m1} is the maximum packing fraction for equant particles and given as 0.656 and 0.55 for smooth and rough particles, respectively (Mader et al. 2013); b is a fitting parameter equal to 1.08 and 1 for smooth and rough particles, respectively. Klein et al. (2018) demonstrate that the only parameter in Eqn. 6.20 that is directly affected by particle shape is the monomodal Φ_m.

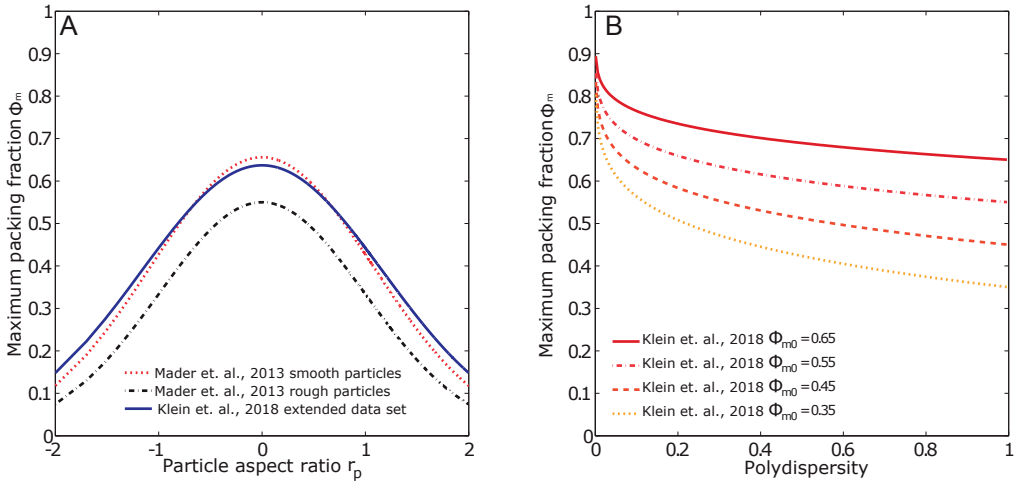

Figure 6.2. A) Summary of models of maximum packing fraction as a function of particle aspect ratio. All models are based on the equation of Mueller et al. (2010) for which Mader et al. (2013) highlighted the separation of smooth and rough particles and Klein et al. (2018) presented an improved fit based on an extended dataset. Note that these are established for monodisperse particle suspensions. **B)** The dependence of maximum packing fraction on particle polydispersity after Klein et al. (2018), plotted here for Φ_{m0} of 0.65–0.35. Note that ϙ = 1 is the monodisperse limit (i.e., polydispersity increases with decreasing ϙ) and Φ_{m0} is the maximum packing fraction of a monodisperse suspension and is derived from subplot A.

To address the issue of suspension with polydisperse particle size populations, highlighted in the previous section, Klein et al. (2017) show that the polydispersity (Φ) of solid particles is the main parameter that influences Φ_m and hence the viscosity of a given suspension. Using the Maron–Pierce equation (Eqn. 6.6, Table 1.1), they derived an empirical model that relates polydispersity of a particle size population with the maximum packing fraction Φ_m of a suspension and takes the shape of:

$$\Phi_m = 1 - \left((1 - \Phi_{m0})\, \varrho^{\alpha}\right) \tag{6.22}$$

where Φ_{m0} represents Φ_m for a monomodal suspension derived from Equation (6.21) (solid curve in Fig. 6.2A), α = 0.173 is an empirical constant and ϱ is the polydispersity of the suspension. The polydispersity represents the ratio of the specific surface area of a polydisperse system S_p to that of a monodisperse system S_m at the same volume fraction with radius r (Torquato 2013). Thus, increasing polydispersity decreases the surface area ratio (ϱ) and $\varrho = 1$ represents the monodisperse limit (i.e., lower values indicate higher degrees of polydispersity):

$$\varrho = \frac{S_p}{S_m} = \frac{r\langle r\rangle}{\langle r^3\rangle} = \frac{\langle r\rangle\langle r^2\rangle}{\langle r^3\rangle} \tag{6.23}$$

with $\langle r^n\rangle$ being the n-th moment of a given size distribution.

This approach was further expanded for application to polydisperse suspensions of varying aspect ratios in Klein et al. (2018), where the authors present a re-parameterization of the Mueller et al. (2010) data for smooth particles, based on an experimental dataset expanded to lower r_p and they recover a best fit for $\Phi_{m1} = 0.637$ and $b = 1.171$. Using this updated fitting approach and data sets of polydisperse suspensions with mean aspect ratios of ~7 and ~0.09, Klein et al. (2018) showed that Equation (6.22) is a robust tool to also estimate Φ_m for polydisperse distributions of suspensions with particles of aspect ratios above and below 1. Their analyses show that Φ_m systematically decreases, while maintaining the general relation of decreasing Φ_m with increasing polydispersity ϱ (Fig. 6.2B).

In summary, Φ_m decreases as particle aspect ratios deviate from unity and as particle surface roughness increases. Increasing polydispersity (i.e., decreasing ϱ) on the other hand can drastically increase Φ_m by allowing the interparticle space to be filled with smaller particles. It is important to note, however, that the models plotted in Figure 6.2A apply to monodisperse suspensions only but that these can be expanded for application to polydisperse suspensions as shown in Figure 6.2B. However, if both parameters are not constant (e.g., in a suspension of particles of varying size and aspect ratio), Φ_m cannot be predicted with great confidence. No constitutive model for polydisperse suspensions of particles with varying aspect ratio has been presented to date. The data presented by Moitra and Gonnermann (2015) show that varying the proportions of particles of differing aspect ratio can affect Φ_m by up to 25%. Nonetheless, a first order estimate can still be deduced from the work of Klein et al. (2018) by using the mean particle aspect ratio of a suspension of interest.

Parameterization of suspension consistency and flow index. Non-Newtonian effects cannot be described completely by a single, strain-rate-independent viscosity and thus the concept of relative viscosity, which considers the effective viscosity of a suspension at specific stress–strain-rate condition, is, at times, insufficient. A full rheological description requires establishing non-linear flow curves. The most frequently used approach to do so is by employing the three-parameter Herschel–Bulkley model (Eqn. 2.3), accounting for the yield stress, the flow consistency and the flow index of the suspension. As mentioned earlier, the non-Newtonian character increases with increasing Φ, resulting dominantly in shear-thinning behavior. It is therefore necessary to parameterise the consistency and the flow index as a function of Φ and strain rate.

Wildemuth and Williams (1984) showed that the relative viscosities of a large range of suspensions of varying particle shapes collapse on a single curve when plotted against Φ/Φ_m. This finding was echoed in Mueller et al. (2010), who evaluated the relative consistency:

$$K_r = \frac{K}{\eta_0} \tag{6.24}$$

of their experimental data by fitting a modified Maron–Pierce equation in the form of:

$$K_r = \left(1 - \frac{\Phi}{\Phi_m}\right)^{-2} \tag{6.25}$$

The results of their analysis show that the relative consistency of a suspension depends strongly on particle aspect ratio, thus demonstrating that the dependence of K on particle aspect ratio is caused by the dependence of the maximum packing fraction Φ_m on aspect ratio. This correlation was validated for suspensions of varying size and shape modalities by Moitra and Gonnermann (2015); see Figure 6.3.

The flow index, n, characterizes the nature and intensity of the shear rate dependence of viscous flow (i.e., curvature and slope in K–Φ space). The more the flow index differs from 1, the more non-Newtonian the fluid becomes. For non-Newtonian materials without yield stress ($\tau_y = 0$), the flow curve function is $\sigma = K\dot{\varepsilon}^n$ and characterization of the nature and intensity of shear rate dependent changes in rheology are provided by models of the variation of the flow index n as a function of Φ. As the apparent viscosity of the suspension is $\eta_{app} = \frac{\sigma}{\dot{\varepsilon}}$, the relative viscosity is defined as:

$$\eta_r = \left(\frac{K}{\eta_l}\right)\dot{\varepsilon}^{n-1} \tag{6.26}$$

There are several studies presenting parameterization of natural magmatic suspensions or their analogues that show a decrease in effective viscosity with increasing shear rate at any given Φ (i.e., shear thinning behavior; $n < 1$) (Mader et al. 2013). These all describe similar trends where, all other parameters being constant, n decreases with increasing Φ. Since the available

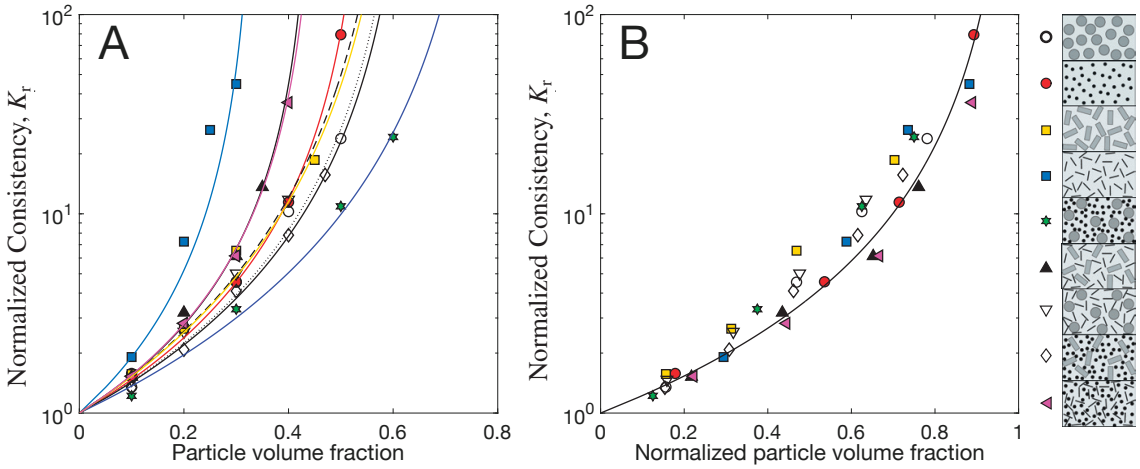

Figure 6.3. Relative consistency of monomodal and polymodal suspensions of varying particle aspect ratios plotted against particle volume fraction (A) and normalized particle volume fraction (Φ/Φ_m) (B), modified after Moitra and Gonnermann (2015). Lines in (A) are the best-fits of a Maron–Pierce type model (Eqn. 6.25) where the exponent (−2) has been adapted to fit each dataset and the line in (B) is the best for all dataset of a Maron–Pierce type model (Eqn. 6.25) where the exponent is −1.92 (see Moitra and Gonnermann (2015) for further details).

models describe the flow index as a function of Φ/Φ_m, it is important to view them in the light of the parameterization of Φ_m presented earlier in this section. This is highlighted in Mueller et al. (2010) and Moitra and Gonnermann (2015), who show that the onset of shear-thinning behavior commences at lower Φ for higher aspect ratio particles and that flow index values do not collapse onto a single curve by normalising the Φ/Φ_m (Fig. 6.3). Based on the measured systematic dependence of n (Φ/Φ_m) on particle aspect ratio, Mueller et al. (2010) derive an empirical relationship (Eqn. 6.28, Table 6.2). Their results show that non-Newtonian behavior is primarily controlled by particle aspect ratio rather than consistency or yield stress. Moitra and Gonnermann (2015) echo these findings and show that across different suspension types, at constant Φ, n decreases with increasing particle aspect ratio, and/or with decreasing particle size heterogeneity. However, instead of incorporating particle aspect ratio into the model, they introduce n_{min} that is the corresponding value of n at Φ_m (Eqn. 6.30, Table 6.2). Both Φ_m and n_{min} have to be estimated or determined experimentally but can also, alternatively, be treated as fitting parameters for data of unknown Φ_m and n_{min}. Truby et al. (2015) present measurements on three phase suspensions and derive the first, empirical, parameterization of the flow index for bubble-bearing suspensions (Eqn. 6.31, Table 6.2) and for multiphase suspensions, accounting for the volume fraction of particles and bubbles (Eqn. 6.32, Table 6.2).

Due to the higher technical difficulties and uncertainties of high temperature experimentation compared to experiments on analogue materials and the increased complexity of the sample textures as well as their quantification, the number of high temperature datasets parameterizing n, K and Φ_m remains scarce compared to those of analogue suspensions. To date, only two parameterizations of the flow index as a function of Φ/Φ_m have been presented that derive from experimentation on natural magmatic suspensions, namely Ishibashi (2009) (Eqn. 6.27, Table 6.2) and Vona et al. (2011) (Eqn. 6.29, Table 6.2).

Table 6.2. Equations for parameterization of the flow index.

Equation	Reference	Comment	Eqn. #
$n = 1 - 2\alpha\left[\ln\left(1 - \frac{\Phi}{\Phi_m}\right)\right]^2$	Ishibashi (2009) Eqn. 9b	From HT experiments, with $\alpha = 0.118$	(6.27)
$n = 1 - 0.2 r_p \left(\frac{\Phi}{\Phi_m}\right)^4$	Mueller et al. (2010) Eqn. 5.2	From analogue experiments	(6.28)
$n = 1 + 2\alpha \log\left(1 - \frac{\Phi}{\Phi_m}\right)$	Vona et al. (2011) Eqn. 20	From HT experiments, with $\alpha = 0.118$	(6.29)
$n = 1 - \left(1 - n_{min}\right)\left(\frac{\Phi}{\Phi_m}\right)^{2.3}$	Moitra and Gonnermann (2015) Eqn. 14	From analogue experiments	(6.30)
$n = 1 - 0.334\Phi_b$	Truby et al. (2015) Eqn. 6.1	From analogue experiments on bubbles	(6.31)
$n = 1 - 0.2\left(\frac{\Phi}{\Phi_m}\right)^4 - 0.334\Phi_b$	Truby et al. (2015) Eqn. 6.2	From analogue experiments on multiphase mixtures	(6.32)

All presented models in Figure 6.4 show reasonable agreement up to $\Phi/\Phi_m = 0.5$ but they deviate significantly at higher Φ/Φ_m. This is likely a result of the variation in the textural makeup of the suspensions measured in the different studies (i.e., particle size, particle shape as well as orientation and distribution), which end up influencing the parameterization. While the relative consistency/viscosity of the investigated suspensions can be described satisfactorily by Φ_m alone, which is only dependent on particle shape and polydispersity (see section on parameterization of Φ_m above), the non-Newtonian character of particle suspensions has a more complex relation to its textural features. Thus, it is likely owing to the paucity of existing experimental data on polydisperse suspensions that a general functional description of the effect of textural parameters on the non-Newtonian character of suspensions has not been presented so far.

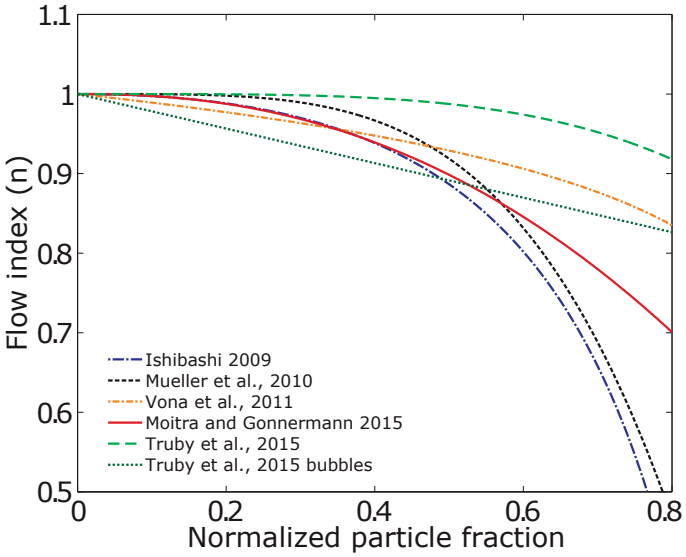

Figure 6.4. Models of the variation of the flow index as function of particle fraction, normalised for $\Phi_m = 0.65$. All models are summarized in Table 6.2. The Ishibashi (2009) model is fitted for Vona et al. (2011) data with $\alpha = 0.118$. Mueller et al. (2010) is plotted for the mean particle aspect ratio, $r_p = 6.5$. Moitra and Gonnermann (2015) is plotted for $n_{min} = 0.5$. Truby et al. (2015) is plotted for $\Phi_b = 0$, and Truby et al. (2015) bubbles for the effect of bubbles on a particle free melt.

Parameterization of the yield stress τ_y

To complete the description of non-Newtonian flow laws, using the Bingham equation ($\sigma = \eta_B \dot{\varepsilon} + \tau_y$) or the three parameter Herschel–Bulkley equation (Eqn. 2.3), for suspensions with an apparent yield stress, a parameterization of the yield stress (τ_y) as a function of Φ is required. Yield stress is defined as the stress under which a suspension first begins to show liquid-like behavior (i.e., continuous deformation) as stress is increased from zero or, similarly, the point where, when decreasing the applied stress, solid-like behavior (i.e., no continuous deformation) is first noticed. In particle suspensions, yield stress is thought to develop when a network of interacting particles is generated (Philpotts and Carroll 1996). At low shear stresses, this network is deformed elastically and ultimately broken up once the yield stress is reached, allowing the suspension to flow (Heymann et al. 2002). The first parameterization of yield stress in magmas was given by (Ryerson et al. 1988) and is based on experiments on natural lava at high temperature (Eqn. 6.33, Table 6.3). More recently, based on channelized flows of analogue material, Castruccio et al. (2010) proposes a different equation (Eqn. 6.34, Table 6.3) where a critical particle fraction, Φ_C, for development of a yield stress, is given (and reported as Φ_C =0.27).

However, these do not include any parameterization of the efficiency of particle–particle interaction as a function of textural parameters such as aspect ratio or packing density.

Table 6.3. Equations for parameterization of the yield stress.

Equation	Reference	Comment	Eqn. #
$\tau_y = 6500\Phi^{2.85}$	Ryerson et al. (1988) Eqn. 17		(6.33)
$\tau_y = 5\times10^6\left(\Phi - \Phi_C\right)^8$	Castruccio et al. (2010) Eqn. 18	With $\Phi_C = 0.27$	(6.34)
$\tau_y = 200\left(\frac{D_p}{\Phi_m - \Phi}\right)\left(\frac{\Phi_m}{1-\Phi_m}\right)^2\left(\frac{1}{\eth^{1.5}\sigma_g^2}\right)$	Gay et al. (1969) Eqn. 27	Where for spheres ð = 0.118. σ_g is the geometric standard deviation for particle diameter, reported as 2.02	(6.35)
$\tau_y = \left[A\left(\frac{\frac{\Phi}{\Phi_C}-1}{1-\frac{\Phi}{\Phi_m}}\right)\right]^{\frac{1}{m}}$	Wildemuth and Williams (1985) Eqn. 2b	A, Φ_C and m are constants reported as 0.848, 0.1978 and 0.8364,	(6.36)
$\tau_y = \left(\frac{\left(\frac{\Phi}{\Phi_C}-1\right)}{\left(1-\frac{\Phi}{\Phi_m}\right)}\right)^{\frac{1}{p}}\tau_c$	Zhou et al. (1995) Eqn. 8	With $\Phi_C = 0.2$ and $p = 1.3$. τ_c is the inter-particle cohesion, expressed as: $\tau_c = \frac{1}{6C\pi a^3}$ where a is the particle radius; C is a fit parameter	(6.37)
$\tau_y = \left(1-\frac{\Phi}{\Phi_m}\right)^{-2} - 1$	Heymann et al. (2002) Eqn. 9		(6.38)
$\tau_y = \tau^*\left[\left(1-\frac{\Phi}{\Phi_m}\right)^{-2} - \left(1-\frac{\Phi_C}{\Phi_m}\right)^{-2}\right]$	Moitra and Gonnermann (2015) Eqn. 15	τ^* is a fitting parameter.	(6.39)

It is intuitive that the efficiency of formation of interacting particle networks varies also with particle concentration, size and shape. Thus, a model capturing these complexities needs to be able to account for their variation. Some experimental datasets document that yield stress arises at lower particle concentrations for higher particle aspect ratios due to more efficient particle–particle interaction. As a result, more robust parameterization approaches of τ_y as a function of Φ frequently include its relation to Φ_m allowing to capture the fact that the development of yield stress is strongly dependent on particle packing efficiency (Eqn. 6.33 to Eqn.6.39, Table 6.3) (Gay et al. 1969; Wildemuth and Williams 1985; Ryerson et al. 1988; Zhou et al. 1995; Heymann et al. 2002; Castruccio et al. 2010; Moitra and Gonnermann 2015).

Most datasets that serve as a basis to develop these relationships report that yield stress is small or negligible for $\Phi \ll \Phi_m$ but rapidly becomes appreciable when $\Phi/\Phi_m \geq 0.8$ (Mueller et al. 2010). Further, yield stress tends to be larger for smaller particles, as these can achieve high packing densities and thus generate stronger networks (Heymann et al. 2002). Published models for the relationship between τ_y and Φ predict vastly different values (see Fig. 6.5), which is

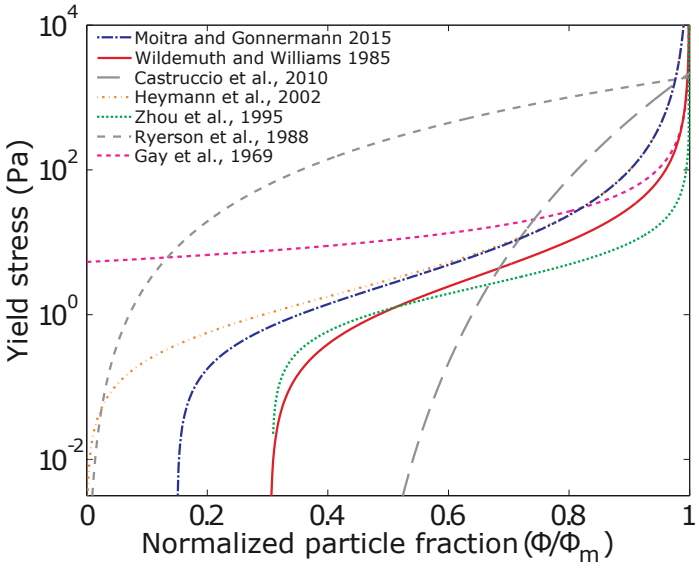

Figure 6.5. Examples of models for yield stress as a function of particle content, plotted for Φ/Φ_m with $\Phi_m = 0.65$. Models are summarized in Table 6.3. Gay et al. (1969) is plotted for Dp = 0.000833333 (i.e., 250 micron particle size). Moitra and Gonnermann (2015) is plotted for $\tau^* = 1$ and $\Phi_C = 0.0975$.

likely due to the fact that they were individually derived from, or optimized for, a narrow range of rheological data and suspension textures. However, with exception of the models presented by Ryerson et al. (1988) and Castruccio et al. (2010), that are derived from high temperature and analogue flow experiments, respectively, the models show broad agreement that yield stress rapidly increases at $\Phi \rightarrow \Phi_m$. As evident from the variation in the predicted values, the available experimental data prove difficult to model and no robust relationship between Φ, Φ_m and τ_y is available. Heymann et al. (2002) suggest that smaller particle sizes produce higher yield stresses as a result of increased particle–particle interactions and Mader et al. (2013) discuss the importance of aspect ratio for the development of yield stress. However, the conditions under which an apparent yield stress is measured is fundamentally linked to the measurement limitations of the rheometric apparatus (predominantly the lower shear rate and -stress limit).

The inconsistencies in the determination of yield stress likely root in the fact that the yield stress is best described as a transition zone between two regimes of drastically varying deformation timescales (Barnes 1999), rather than being a rheological constant, which it is commonly interpreted to be. For a detailed discussion of the nature of the yield stress, its relevance and application to natural multiphase suspensions please see Figure 6.9 in the later section "*The yield stress dilemma*" below.

Unsteady flow in particle suspensions. While unsteady flow in bubble suspensions is relatively well understood (see below), this is not the case for particle suspensions. Much of the data reviewed above consider steady (i.e., continuous) flow. Data from oscillatory measurements on particle suspensions, which can measure unsteady flow (aiming for example to describe the rheological effect of seismic waves propagating through a suspension) are scarce. Sumita and Manga (2008) present a study of the oscillatory rheology of analogue suspensions of spherical particles at volume fractions of $0.2 < \Phi < 0.6$. They present data for the response of the elastic and viscous moduli as a function of oscillation frequency and find a strain dependent rheological evolution where the suspension displays three rheological regimes. The response is initially linear viscoelastic, becomes shear-thinning with increasing strain amplitude and transitions to shear-thickening at high strain amplitudes. They suggest the suspensions may be best described by combining both relaxation and retardation phenomena (i.e., a Burgers model; see Findley et al. (1977). However, experimental data remain scarce and thus no systematic description of suspension rheology in unsteady flow has been presented to date.

Mader et al. (2013) evaluate oscillatory viscometry data for particle volume fractions in the concentrated regime $\Phi > 0.25$ and report that the complex viscosity measured under forced oscillation is consistently lower than the effective viscosity measured in steady shear. While the physical origin of this behavior remains unclear, Mader et al. (2013) provide a convincing hypothesis. They suggest that the lower viscosity values measured in oscillation results from variations in the nature of particle–particle interactions between the two flow regimes. They postulate, that particles within suspensions undergoing constant shear (i.e., large total strains) experience numerous and repeated interactions, hence increasing the suspension's viscosity. Particles within suspensions subject to small amplitude oscillations may not move far enough to interact strongly with one another, hence their effect on viscosity is less pronounced. They provide a comparison of previously unpublished data and highlight that this observation appears to be independent of particle aspect ratio.

Bubble suspensions

While the importance of gas bubbles for the rheology of magmas had been evident for several decades (Einarsson 1949), experimental measurements on natural magmatic bubbly melts remained largely absent until the late 80's and early 90's (Spera et al. 1988; Bagdassarov and Dingwell 1992; Stein and Spera 1992; Bagdassarov and Dingwell 1993a; Lejeune et al. 1999). These were paralleled by systematic experimentation on bubble-bearing analogue materials (e.g., Kraynik 1988 and references therein) and theoretical approaches (Taylor 1932; Schowalter 1978; Manga et al. 1998; Manga and Loewenberg 2001). Together, the numerical and experimental evidence from both analogue and natural bubble suspensions document that the presence of bubbles can both increase and decrease the effective viscosity of a suspension depending on the force balance around the suspended bubble. The theoretical framework defining the differing flow regimes in magmatic bubble suspensions was first rigorously defined in Rust and Manga (2002) and Llewellin et al. (2002b). These studies document that under steady flow conditions the force balance around bubbles is well described by the capillary number (Eqn. 3.5).

At low capillary number, bubbles act to increase suspension viscosity since the bubbles remain spherical and thus represent an obstacle to the flow field. At constant bubble volume and increasing capillary number, this effect decreases with increasing bubble elongation. At large capillary numbers, bubbles are highly elongate and flow line distortion is small, thus bubbles act to decrease suspension viscosity as they introduce free slip surfaces in the liquid (Rust and Manga 2002). The effect is plotted for a range of Ca in Figure 6.6A, Equation 6.51.

Under changing flow conditions, the capillary number has to be described as the ratio of the bubble relaxation time λ_b to the fluid deformation timescale ($1/\dot{\varepsilon}$), thus $Ca = \lambda_b \dot{\varepsilon}$. The bubble relaxation time describes the timescale on which a deformed bubble returns to spherical shape under the action of surface tension in the absence of shear or, similarly, the timescale over which a bubble can respond to a change in its shear environment. For a single bubble in a Newtonian liquid, the bubble relaxation time is:

$$\lambda_b = K_b \frac{\eta_0 a}{\Gamma} \tag{6.40}$$

where K_b is a dimensionless constant that is a function of the bubble volume fraction. For dilute systems, $K_b = 1$, i.e., the bubble does not interact with other bubbles or particles. In non-dilute suspensions, $K_b > 1$; the bubbles interact with each other and their deformation is affected by neighboring bubbles. Theoretical and experimental investigations in this regime have found that in such systems λ_b increases with increasing gas volume fraction (Oldroyd 1953; Oosterbroek and Mellema 1981; Loewenberg and Hinch 1996; Llewellin et al. 2002b; Rust and Manga 2002).

For flow to be steady, the shear conditions must either remain constant or change slowly with respect to λ_b. A further complication arises when flow is unsteady (i.e., strain-rate varies as a

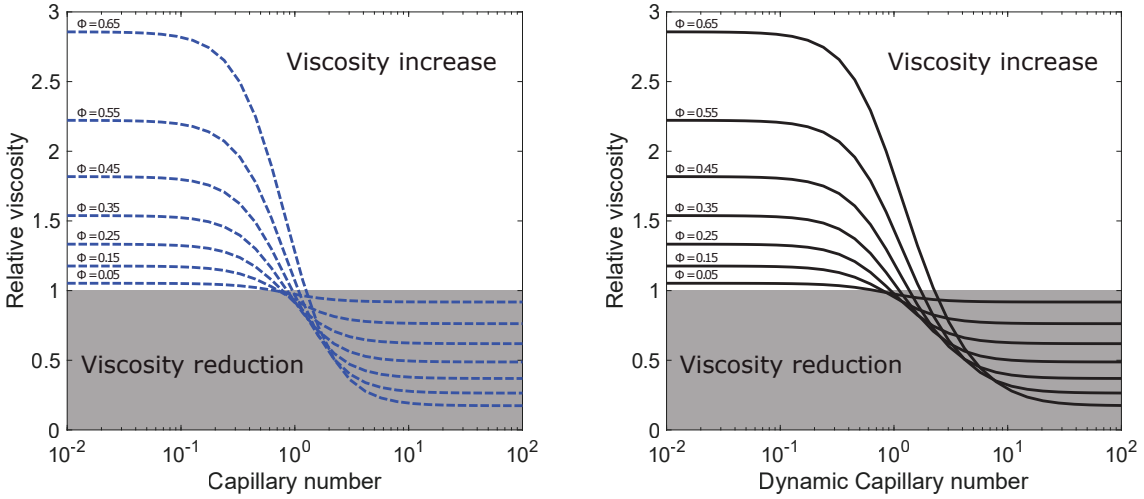

Figure 6.6. The effect of bubble relaxation on relative viscosity under **A)** steady flow conditions, where Ca is the relevant dimensionless parameter for bubble shape and **B)** unsteady flow conditions, where Cd is the relevant dimensionless parameter for bubble shape. Note that the difference in flow condition is not of drastic effect to the relative viscosity. An approximate solution for conditions where both parameters vary was proposed in Mader et al. (2013) (see Eqn. 6.52)

function of time, where the rate- of change in strain rate may vary as well). This is often the case for volcanic flows when a magma batch moves through the conduit to the surface. Unsteady flow introduces an effect of bubble elasticity resulting from the bubble surface tension and thus, in an unsteady flow, energy can be stored and released during changes in the shear conditions. The rheology thus becomes viscoelastic and requires quantification of both the viscous and elastic moduli (Bagdassarov and Dingwell 1993b; Llewellin et al. 2002a,b; Rust and Manga 2002)

Rust and Manga (2002) and Llewellin et al. (2002b) consider a characteristic timescale for the rate of change of the shear environment (λ_b) that describes the time required for the change in strain-rate ($\ddot{\varepsilon}$) to be of the same magnitude as the strain-rate itself, i.e., $\lambda_b = \frac{\dot{\varepsilon}}{\ddot{\varepsilon}}$. If $\lambda_b < \frac{\dot{\varepsilon}}{\ddot{\varepsilon}}$, the bubbles can adjust their shape sufficiently fast to maintain an equilibrium shape (corresponding to the specific strain-rate environment) and flow can be considered steady. On the other hand, if $\lambda_b > \frac{\dot{\varepsilon}}{\ddot{\varepsilon}}$, the bubbles do not manage to reach an equilibrium shape on the timescale of change in the strain rate environment and the flow is unsteady. To describe this flow steadiness Llewellin et al. (2002b) introduce the dynamic capillary number:

$$\mathrm{Cd} = \lambda_b \frac{\dddot{\varepsilon}}{\dot{\varepsilon}} \tag{6.41}$$

when $\mathrm{Cd} \ll 1$ bubble relaxation is fast with respect to the timescale of change in strain rate; the flow is approximately steady, and the viscosity of the suspension can be described by the capillary number Ca. In this regime the viscosity of the bubble suspension can increase or decrease with Φ_b depending on the bubble shape. When $\mathrm{Cd} \gg 1$, the bubbles do not relax fast enough to reach equilibrium shapes; Ca is then undefined, and the bubbles deform with the flow. Thus flow-line distortion past the bubble is reduced, inducing free-slip surfaces. The strain will then be accommodated via changes in the bubble shape and, since their viscosity is negligible with respect to the viscosity of the melt, the effective viscosity of a bubble suspension in unsteady flow is lower than the viscosity of the bubble free melt (i.e., $\eta_r < 1$). This results in a decrease in the suspension viscosity as Φ_b increases. The effect is plotted for a range of Cd in Figure 6.6B, Equation (6.52).

Early models on bubble suspension rheology, describing the relative suspension viscosity as a function of bubble volume fraction Φ_b did not incorporate this variation in deformation regime and are thus, very restricted in their applicability. The first model of this kind was presented by Taylor (1932) who extended Einstein's theory to emulsions of two liquids and derived Equation (6.42) (Table 6.4) for a suspended phase of negligible viscosity. Later experiments on bitumen emulsions by Eilers (1941) and Eilers (1943) found a more pronounced increase in relative viscosity at higher Φ_b and they presented a model with two different fitting parameters (Eqn. 6.43, Table 6.4). Both these approaches assume steady deformation (Cd $\ll$ 1) and that the bubbles' deformation from spherical is negligible (Ca $\ll$ 1). Thus, due to the distortion of flow lines around the bubbles, the relative viscosity increases with increasing Φ_b (Fig. 6.7A). Mackenzie (1950) presented a theoretical study on the mechanics of a solid containing spherical holes that takes the form of Equation 6.44, Table 6.4. Although this theory can in principle be applied to describe bubble suspensions, it neglects surface tension and thus only holds for flow conditions where the bubbles maintain their spherical shape (Ca $\ll$ 1). Later models are based on experiments within the steady regime (Cd $\ll$ 1) but at varying degrees of bubble deformation (Ca > 1). Thus, in these models, due to the reduction in distortion of flow lines around the bubbles with elongation, the relative viscosity decreases with increasing Φ_b (Fig. 6.7B).

Hashin and Shtrikman (1963) presented a modified theoretical approach for a suspension of randomly positioned spherical bubbles, describing the viscosity reducing bubble deformation regime (Eqn. 6.45, Table 6.4). Subsequently, a number of studies were presented that measured and empirically parameterized the effect of porosity on the relative viscosity of suspensions within natural and synthetic glass powder analogues during compaction (Eqns. 6.46–6.48, Table 6.4). Note that we use ϕ for models considering pore space between granular materials whereas we use Φ_b for models considering bubbles in a liquid, the important difference between these two textures is discussed in detail below.

The first parameterization of experiments on bubbly volcanic melts were presented by Bagdassarov and Dingwell (1992), who describe a marked decrease in relative viscosity with increasing bubble volume fraction (Eqn. 6.49, Table 6.4). More recently, Vona et al. (2016) performed uniaxial compression experiments on foamed rhyolites at bubble fractions up to 0.65 and documented a similarly strong decrease in relative viscosity, which they fit using a modified version of the model proposed by Ducamp and Raj (1989) that allows more flexibility in the model shape at low Φ_b and takes the form of (Eqn. 6.50, Table 6.4).

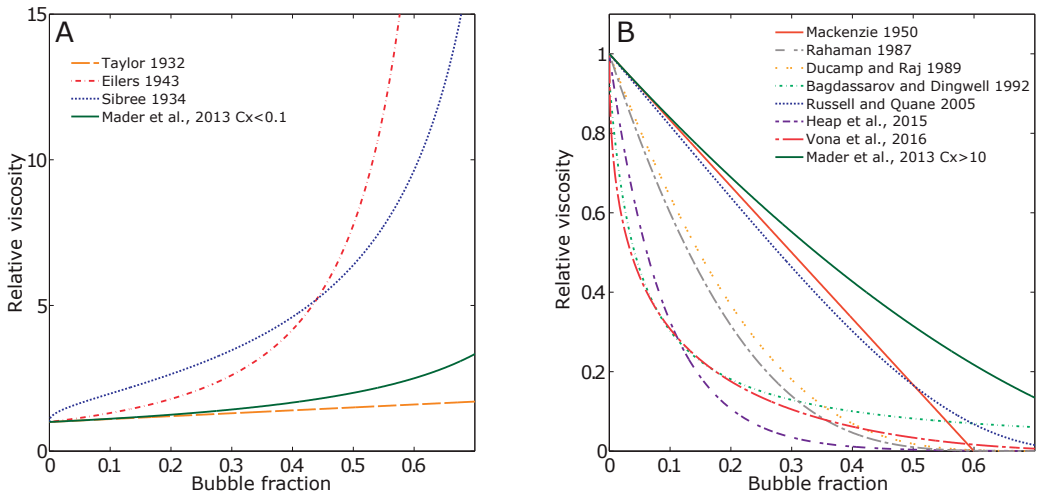

Figure 6.7. Models of relative viscosity vs.= bubble volume fraction for steady deformation (Cd $\ll$ 1) for **A)** bubble deformation from spherical is negligible (Ca $\ll$ 1) using the equations given in Table 6.4. We plot Mader et al. (2013) for Cx < 0.1 and **B)** varying degrees of bubble deformation (Ca > 1). We plot Mader et al. (2013) for Cx < 10.

The striking variation in the predicted relative viscosities plotted in Figure 6.7A,B highlight the textural complexity of the problem. It is worth noting that models derived from compaction of particulate materials presented by Rahaman et al. (1987), Ducamp and Raj (1989), Quane and Russell (2005), Quane et al. (2009) and Heap et al. (2014) predict a much more pronounced reduction on relative viscosity with increasing Φ_b than the theoretical or semi theoretical models of Mader et al. (2013) and Mackenzie (1950), which consider bubbly melts and unconnected pore space, respectively. Only the model presented in Quane and Russell (2005) shows reasonable agreement with the theoretical or semi theoretical models (Fig. 6.7B). This discrepancy between data describing bubbly liquids and those describing compacting granular material is likely because in compacting granular material the pore space is both non-spherical and highly connected. Because the pore space is highly connected, it forbids treating the pores as separate entities since gas can readily be displaced within the pore space (i.e., move within

Table 6.4. Equation for parameterization the flow of bubbly or porous melts.

Equation	Reference	Comment	Eqn.
$\eta_r = 1 + \Phi_b$	Taylor (1932) Eqn. 19		(6.42)
$\eta_r = \left(1 + \frac{1.25\Phi_b}{1 - b\Phi_b}\right)^2$	Eilers (1943) Eqn. 3	With b = 1.28–1.30.	(6.43)
$\eta_r = 1 - \frac{5}{3}\Phi_b$	Mackenzie (1950) Eqn. 24		(6.44)
$\eta_r = 1 - \frac{5\Phi_b}{3 + 2\Phi_b}$	Hashin and Shtrikman (1963) Eqn. 3.17		(6.45)
$\eta_r = e^{-b\phi}$	Rahaman et al. (1987) Eqn. 35	With b =11.2	(6.46)
$\eta_r = e^{-b\left(\frac{\phi}{1-\phi}\right)}$	Ducamp and Raj (1989) Eqn. 8	With $2.5 < b < 4$	(6.47)
$\eta_r = 10^{-\frac{\alpha\phi}{1-\phi}}$	Russell and Quane (2005) Quane et al. (2009) Heap et al. (2014) Eqn. 7	Where α is a material-dependent fitting coefficient: α = 5.3 for glass beads, α = 0.78 for Bandelier Tuff ash. α = 2 for crystal-bearing melts from Mount Meager.	(6.48)
$\eta_r = \frac{1}{1 + b\Phi_b}$	Bagdassarov and Dingwell (1992) Eqn. 5	With b = 22.4	(6.49)
$\eta_r = e^{-\alpha\left(\frac{\Phi_b}{1-\Phi_b}\right)^\beta}$	Vona et al. (2016) Eqn. 4	With α = 1.47 and β = 0.48.	(6.50)
$\eta_r = \eta_{r\infty} + \frac{\eta_{r0} - \eta_{r\infty}}{1 + (K\mathrm{Ca})^m}$	Rust and Manga (2002) Eqn. 9 Llewellin et al. (2002b)	With K = 6/5 and m = 2 η_{r0} and $\eta_{r\infty}$ represent the relative viscosity at the low and high Ca limit	(6.51)
$\eta_r = \eta_{r\infty} + \frac{\eta_{r0} - \eta_{r\infty}}{1 + Cx^m}$	Mader et al. (2013) Eqn. 32	With $Cx = \sqrt{\mathrm{Ca}^2\mathrm{Cd}^2}$, $\eta_{r0} = (1 - \Phi_b)^{-1}$, $\eta_{r\infty} = (1 - \Phi_b)^{\frac{5}{3}}$ For details please see the text in the following paragraphs	(6.52)
$\eta_r = \frac{1}{1 - (b\Phi_b)^{\frac{1}{3}}}$	Sibree (1934) Eqn. 1 optimizing Hatschek (1911)	With b = 1.2	(6.53)

or escape from the system). The flow process in such compacting materials, where gas escapes through a compacting particulate framework is very different to that of a bubbly liquid that flows as a unit and thus flow lines are affected by the presence and nature of bubbles. Nonetheless, both the data (Fig. 6.8) and derived models (Fig. 6.7) presented by Bagdassarov and Dingwell (1992), Bagdassarov and Dingwell (1993b) and Vona et al. (2016), that were developed on the basis of experiments on bubbly melts, also predict a more pronounced reduction on relative viscosity with increasing Φ_b than the theoretical or semi theoretical models of for example Mader et al. (2013), Manga and Loewenberg (2001) and Mackenzie (1950), see Figure 6.8.

Re-evaluation of the data of Vona et al. (2016); (Vona pers. comm., and Sicola et al. 2021) reveal that the measurements likely underestimate the effective viscosity of the sample. This is because the samples developed high connectivity between the bubbles due to bubble wall breakage during post foaming quench. This alteration of sample texture resulted in deformation behavior more akin to collapsing foam or compacting particle mixtures and, hence, drastically reduced effective viscosity. New experimental data by Sicola et al. (2021) that were measured immediately after foaming and without any thermal or mechanical stressing between foaming and viscosity measurement document a less pronounced viscosity reduction and better agreement with the models derived from analogue suspensions. Further, re-evaluation of the data reduction strategy of Bagdassarov and Dingwell (1992); (for details please refer to "*Experiments on high temperature silicate melt suspensions"* section) indicates that these measurements also underestimate the effective viscosity and that corrected values of relative viscosity are higher than

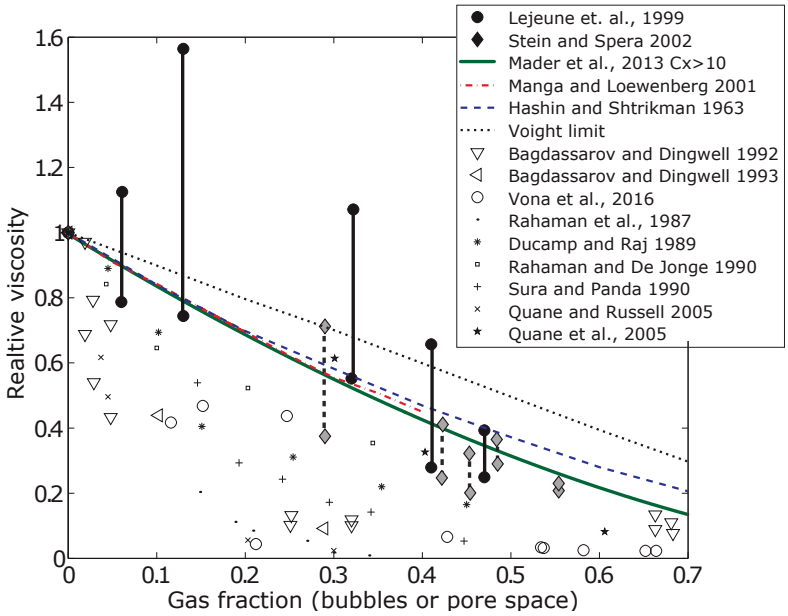

Figure 6.8. Available experimental data on porous melts and bubble suspensions. Maximum and minimum values of validated rheological data on bubble suspensions are plotted as large filled symbols and the spread at each bubble volume fraction is highlighted by the connecting bar. Note that the data from Lejeune et al. (1999) were measured at varying temperatures and thus there may be an error in bubble volume fraction due to bubble expansion/contraction when varying experimental conditions, which is the likely cause for the spread in the measured relative viscosities. Data from rheological measurements for which underestimation of the relative viscosity is likely are plotted as **large open symbols**, see main text for details. Data from experiments on compaction of a melt framework with communicating pore space are plotted as **small symbols**. Note that while these experimental data are valid for sintering and compaction of fragmental volcaniclastic materials, the presence of an interconnected pore network is not representative of bubbly magma. This compilation highlights that validated measurements on natural bubbly melts agree reasonably well with theoretical and empirical models derived from bubble suspensions of analogue materials, potentially resolving the highly debated spread in measured values and consoling measurements on natural materials with those on analogue suspensions. **Lines** represent different theoretical and semi theoretical models on bubble suspensions that are validated by measurements on analogue materials.

predicted by the respective models (Fig. 6.8). Re-processing of the data following the improved data reduction mechanism proposed in Section 4 (Eqn. 4.10) might allow to unite these data with those of analogue experiments, theoretical models and the experiments of Lejeune et al. (1999) and Stein and Spera (2002).

Nonetheless, after accounting for the parallel plate viscometry data deviating from the models derived from analogue suspensions, the low effective viscosities reported from the in oscillatory measurements presented in Bagdassarov and Dingwell (1993b) remain at odds with the remaining dataset. This is likely due to the fact that the strain in oscillatory measurements is extremely small. These measurements are advantageous for probing sample viscosity without imposing any relevant textural deformation or re-orientation, as it is the case during for example the viscous dissipation of seismic energy in magmatic bodies. However, these measurements are not directly applicable to magma migration and lava flow since the bubbles do not deform significantly or reach an equilibrium shape and, thus, their contribution to the effective shear viscosity during flow is not fully expressed. Similar strain dependent effects in oscillatory measurements have been documented for particle suspensions by Sumita and Manga (2008), who present a study of the rheology of analogue suspensions of spherical particles. They document a strain dependent rheological evolution during oscillation, where the suspension displays three rheological regimes. At low strain amplitude, the response is linear viscoelastic, becomes shear-thinning with increasing strain amplitude and transitions to shear-thickening at high strain amplitudes. Oscillatory measurements at low strain amplitude are nonetheless highly valuable for systematic development of a strain-dependent understanding of the effect of bubbles on suspension rheology, because the measurements represent the low strain endmember. Development of a complete, strain dependent, dataset would require correlation of frequency dependent data to data from methods probing higher strain regimes. To date, this remains challenging, largely due to the paucity of experimental data and because torsion experimentation following in the above reviewed studies focused chiefly on deformation in simple shear and much higher total strains.

The variation in flow process and the re-evaluation of the data of Vona et al. (2016), Bagdassarov and Dingwell (1992) and Bagdassarov and Dingwell (1993b) potentially allows to address the large spread in the models predicting a reduction on relative viscosity in Figure 6.7B, narrowing the spread of models applicable to bubbly melts. However, it does not allow reconciliation of the apparent contradiction between the theoretical and experimental studies that describe η_r increasing with Φ_b (Fig. 6.7A) and those that describe the opposite (Fig. 6.7B). Doing so requires a model that also incorporates the different flow regimes and bubble deformation timescales and thus can describe both the increase in relative viscosity for $Ca < 1$ and the decrease of the relative viscosity in the case of $Ca > 1$ as well as the dynamic changes of steady to unsteady flow regimes. To capture this broad range, both Llewellin et al. (2002b) and Rust and Manga (2002) performed experiments across a wide range of Ca and Cd. Both studies confirm that bubbles may increase or decrease the viscosity of a suspension depending on the conditions of shear.

Based on the work of Frankel and Acrivos (1970), who present a complete physical analyses of emulsion rheology and derive a constitutive equation that is restricted to dilute emulsions of high viscosity contrast and where the bubbles remain approximately spherical, Llewellin et al. (2002b) and Rust and Manga (2002) propose an expression for steady, simple-shear flow (i.e., $Cd \ll 1$; Ca variable) in the form of a Cross model (Cross 1965):

$$\eta_r = \eta_{r\infty} + \frac{\eta_{r0} - \eta_{r\infty}}{1 + \left(K\mathrm{Ca}\right)^m} \tag{6.51}$$

where $K = 6/5$ and $m = 2$, and η_{r0} and $\eta_{r\infty}$ represent the relative viscosity of the suspension at the low and high Ca limit, respectively

On the basis of the work of Pal (2003) and Llewellin and Manga (2005); Mader et al. (2013) generalize the low (η_{r0}; Ca < 0.1) and high ($\eta_{r\infty}$; Ca > 10) capillary number limits for application to non-dilute suspensions, proposing:

$$\eta_{r0} = \left(1 - \Phi_b\right)^{-1} \tag{6.52a}$$

$$\eta_{r\infty} = \left(1 - \Phi_b\right)^{\frac{5}{3}} \tag{6.52b}$$

Further, Mader et al. (2013) extend the work presented in (Llewellin et al. 2002a) to unsteady flow in simple-shear encompassing large changes in strain and strain rate (i.e., both Ca and Cd may vary simultaneously and independently). They develop a complex general expression for η_r (Ca, Cd), based on which they propose the following approximation that shows good agreement with the more complex theoretical relationships:

$$\eta_r = \eta_{r\infty} + \frac{\eta_{r0} - \eta_{r\infty}}{1 + Cx^m} \tag{6.52}$$

where $m = 2$ for a monodisperse suspension and Cx is the capillarity, defined as:

$$\mathrm{Cx} = \sqrt{\mathrm{Ca}^2 \mathrm{Cd}^2} \tag{6.52c}$$

The two end member cases for the low (η_{r0}; Ca < 0.1) and high ($\eta_{r\infty;}$ Ca > 10) capillary number limits are plotted as dotted lines in Figure 6.7A and 6.7B, respectively. Note that the parameterization proposed in Mader et al. (2013) covers the whole range of Ca and Cd and thus represents a completely new analysis that demonstrates that the dependence of viscosity on Ca and on Cd is practically indistinguishable and can be reduced to the newly introduced term Cx, the capillarity, which captures the combined effect of shear and flow steadiness, effectively reducing the dimensionality of the problem. However, as evident from the summary plot in Figures 6.7B and 6.8, the model does not reproduce the drastic decrease in relative viscosity depicted in some experimental data. This is likely owing to the fact that most experimental data derive from measurements of polydisperse suspensions, which are not described by the model as well as the variations in sample texture and pore space connectivity outlined earlier.

Figure 6.7A also shows the model deduced from high Ca experiments on bubbles in a fungicide liquid stabilised with an organic solvent by Sibree (1934) which is based on the model for foam rheology presented in Hatschek (1911):

$$\eta_r = \frac{1}{1 - \left(b\Phi_b\right)^{\frac{1}{3}}} \tag{6.53}$$

with $b = 1.2$. These experiments show an increase in relative viscosity albeit being performed at high capillary numbers. This is because the textural framework of the suspension transitions from a bubbly liquid to a polyhedral foam at $\Phi_b \gtrsim 0.5$–0.7 (depending on the nature of the bubbly liquid i.e., the maximum packing fraction for the bubble population). The rheology of a bubbly melt can change drastically across this transition due to self-stabilization of the bubble walls as they transition from curved bubble walls to more straight melt films that intersect at plateau boarders in sets of three. This structure is not stable at high strain and can thus result in rapid breakdown of the foam through bubble wall failure and gas escape (Ryan et al. 2019a). A constitutive description of flow in this regime has, however, not been published to date.

In summary, comparing available models for the relative viscosity of bubble suspensions (Fig. 6.7) with those for particle suspensions (Fig. 6.1) it is evident, that increasing the bubble volume fraction affects the relative viscosity of a suspension much less than adding the same volume fraction of solid particles. While many parameterization strategies have been proposed for

bubble bearing melts, there is no systematic agreement between them over any region of Φ_b and no single functional shape seems able to fully describe the complexity of the process. This is largely rooted in two reasons: 1) the fact that bubbles have drastically varying effects on suspension viscosity depending on the deformation regime they encounter (described by the bubble's capillary number which itself is a function of the bubble size and the properties of the suspending liquid), and 2) at elevated bubble fractions ($\Phi_b \gtrsim 0.5$–0.7) the textural framework of the suspension transitions from a bubbly liquid to a foam and its rheology can change drastically across this transition including the development of yield stress via self-stabilization of bubble walls.

The re-evaluation and of existing models presented in this section reveals that to date, the theoretical or semi theoretical models of Mader et al. (2013) and Mackenzie (1950) (black lines in Figure 6.7B) represent the most robust parameterization of the rheology of bubbly melts (with the Mader et al. (2013) model also allowing to parameterize varying Ca and Cd). Based on available measurements on magmatic suspensions it seems that for most experimentally investigated cases, flow occurs in the regime of $Ca \gg 1$ and $Cd \gg 1$ and thus bubbles in most flow scenarios relevant to magma emplacement or lava flow on the surface, will act to decrease the effective viscosity of the magmatic suspension. This review, however, also highlights that available experimental data and field measurements are scarce. Significant effort and careful and systematic experimentation on bubble suspensions of a wide range of textural makeup is needed for validation and / or expansion of these models and to make them usable to assess deformation in magmatic and volcanic environments. Further, the discrepancy between experimental data on analogue materials and natural and synthetic silicate melts remains to be addressed.

Unsteady flow in bubble suspensions. In oscillatory measurements the imposed strain is commonly small and thus, the suspended bubbles remain approximately spherical for most experimental conditions. However, the bubble relaxation timescale remains an important contributor. This was studied in Llewellin et al. (2002b), who provide a comprehensive dataset on unsteady flow in bubbly suspensions, which served as the basis to define the dynamic capillary number Cd (Fig. 6.6B). At low Cd and Ca, the bubble relaxation timescale is faster than the deformation and thus the bubbles remain spherical and act to increase the effective viscosity of the suspension. With increasing oscillation frequency (i.e., increasing Cd) bubbles remain spherical (due to the low imposed strain) but deformation is faster than the bubble relaxation timescale. Thus, the bubbles accommodate deformation through internal strain and act to decrease the effective viscosity of the suspension. Further, the specific effect of the suspended phase (for every investigated Ca and Cd regime) becomes more important with increasing strain and increasing bubble volume fraction. Combined with the existing understanding of bubble–melt–interface tension, the effect of bubbles in unsteady flow is described well by the parameterization framework reviewed earlier in this chapter.

Three-phase suspensions (crystal + bubble + melt)

Few experimental data on magmatic three phase suspensions are available (see the section on high temperature experiments). The available studies commonly observe pseudo-plastic behavior and a strong shear thinning component for all the investigated suspensions and provide empirical equations describing the effective viscosity (η_{eff}) or stress as a function of temperature and strain rate for multiphase magmas (Russell and Quane 2005; Lavallée et al. 2007; Avard and Whittington 2012; Pistone 2012; Pistone et al. 2013; Heap et al. 2014). The differences between these empirical models are small and, nonetheless, a new empirical description was proposed with almost every new experimental dataset. This highlights that, while empirical models are operationally attractive due to their simplicity and are seemingly robust in the light of the respective dataset, a single empirically derived equation for the relative viscosity of a specific lava as a function of temperature is insufficient to capture the complexity of lava dome rheology (See also Fig. 4.7). A more robust parameterization thus requires detailed characterization of the sample texture and its composition to allow application of the parameterization approaches reviewed above.

While few experimental studies have aimed to parameterize the rheology of crystal and bubble-bearing magmas in this way, several theoretical or semi theoretical approaches have employed effective medium theory to do so. Effective medium theory treats multiphase and polydisperse suspensions as incremental products of suspensions of the phase in question within a medium that is characterised by the viscosity of a suspension made of the other phase. For example, Farris (1968) proposed that bidisperse suspensions may be treated as a system where the coarse solid fraction acts as a monodisperse suspension in a separate, monodisperse fluid containing the finer particles (Eqn. 6.16). In order to apply this approach, it is crucial to clearly define the volume fractions of the respective phases in the suspension, as these are the core input parameter to any model employed in effective medium theory.

Volume fractions in three phase suspensions. Particle (crystal)- and gas volume fraction are strictly defined for any suspension when considering the entirety of the suspension. In this case, the concentration of the total suspended phases Φ_t is defined as:

$$\Phi_t = \frac{\Phi_b + \Phi_c}{\Phi_l + \Phi_b + \Phi_c} \tag{6.54}$$

where Φ_l, Φ_c and Φ_b are the volume fraction of liquid, particles and bubbles, respectively.

This strict definition, however, does not apply directly when employing effective medium theory for multi-phase suspensions and varies depending on whether one considers a bubble suspension or a particle suspension as the effective medium. Thus, it is important to clearly define what process is to be investigated when employing effective medium theory. When the bubble suspension is treated as the effective medium, the appropriate definitions are:

$$\Phi_b = \frac{\Phi_b}{\Phi_l + \Phi_b} \tag{6.55}$$

$$\Phi_c = \frac{\Phi_c}{\Phi_l + \Phi_b + \Phi_c} \tag{6.56}$$

This approach is favorable for example when investigating the crystallization of a bubbly magma at constant bubble volume fraction. Whereas if the particle (crystal) suspension is treated as the effective medium, the appropriate definitions are:

$$\Phi_b = \frac{\Phi_b}{\Phi_l + \Phi_b + \Phi_c} \tag{6.57}$$

$$\Phi_c = \frac{\Phi_c}{\Phi_l + \Phi_c} \tag{6.58}$$

This approach is favorable for example when investigating the vesiculation of a magma at constant crystal volume fraction.

Applying effective medium theory. Having defined the volume fractions relevant to the scenario of interest, effective medium theory is applied as follows:

When the bubble suspension is treated as the effective medium, the viscosity of the three-phase suspension (η_{eff}) is the product of the viscosity of the effective medium ($\eta_b\Phi_b$) and the relative viscosity of crystals ($\eta_{r,c}\Phi_c$):

$$\eta_{eff} = \eta_b\left(\Phi_b\right) \times \eta_{r,c}\left(\Phi_c\right) \tag{6.59}$$

with:

$$\eta_b\left(\Phi_b\right) = \eta_l \times \eta_{r,b}\left(\Phi_b\right) \tag{6.60}$$

where η_l is the viscosity of the liquid phase and ($\eta_{r,b}\Phi_b$) is the relative viscosity of bubble suspension and Φ_b and Φ_c are calculated with Equations (6.55) and (6.56).

This approach was applied in Truby et al. (2015), where the effect of particles ($\eta_{r,c}\Phi_c$) is calculated with the Maron and Pierce (1956) equation (Eqn. 6.6), whereas the effect of bubbles is calculated following the approach presented in Mader et al. (2013). Under their experimental conditions, bubbles form the effective medium and deform under low Ca. On this basis, Truby et al. (2015) provide an empirical parameterisation for the flow index :

$$n = 1 - 0.2\left(\frac{\Phi_c}{\Phi_m}\right)^4 - 0.334\Phi_b \tag{6.61}$$

Furthermore, this treatment allowed Truby et al. (2015) to explicitly include variations in Φ_m, including the effects of particle aspect ratio as well as surface roughness. Note that under the condition of $\Phi \sim \Phi_m$ or $\Phi_m = 1$; Equation (6.65) reduces to the Phan-Thien and Pham (1997) model (see below). This approach was applied for example in Kilgour et al. (2016) and Beckett et al. (2014) to reconstruct the rheology of multiphase magmas for the examples of Mt. Ruapehu and Stromboli, respectively.

When the particle suspension is treated as the effective medium, the viscosity of the three-phase suspension (η_{eff}) is the product of the viscosity of the effective medium ($\eta_c\Phi_c$) and the relative viscosity of bubbles ($\eta_{r,b}\Phi_b$):

$$\eta_{eff} = \eta_c\left(\Phi_c\right) \times \eta_{r,b}\left(\Phi_b\right) \tag{6.62}$$

with:

$$\eta_c\left(\Phi_c\right) = \eta_l \times \eta_{r,c}\left(\Phi_c\right) \tag{6.63}$$

where η_l is the viscosity of the liquid phase and $\eta_{r,c}(\Phi_c)$ is the relative viscosity of the crystal suspension and Φ_b and Φ_c are calculated with Equations (6.57) and (6.58). This approach was applied to estimate the viscosity of basaltic lava flows, using the crystal suspension as the effective medium (Rhéty et al. 2017; Dietterich et al. 2018; Chevrel et al. 2019b). Recently, Chevrel et al. (2018), considering the effect of deformable bubbles (Eqn. 6.62) on a crystal suspension effective medium (Eqn. 6.63), provide a robust reconstruction the viscosity of an active pāhoehoe lava that was measured independently using a field viscometer.

An earlier theoretical parameterization was proposed by Phan-Thien and Pham (1997) and later applied by Harris and Allen (2008) to study of basaltic magmas from Mauna Loa and Mount Etna. Depending on the relative size of particles and vesicles, Phan-Thien and Pham (1997) propose three separate equations to capture the multiphase flow behavior:

1. For crystals smaller than vesicles:

$$\eta_{eff} = \eta_l\left(1 - \frac{\Phi_c}{1-\Phi_b}\right)^{-\frac{5}{2}}\left(1-\Phi_b\right)^{-1} \tag{6.64}$$

2. For crystals and vesicles of equal size:

$$\eta_{eff} = \eta_l\left[1 - \Phi_c - \Phi_b\right]^{\frac{-\left(5\Phi_c + 2\Phi_b\right)}{2\left(\Phi_c + \Phi_b\right)}} \tag{6.65}$$

3. For crystals larger than vesicles:

$$\eta_{eff} = \eta_l \left(1 - \frac{\Phi_b}{1-\Phi_c}\right)^{-1} \left(1-\Phi_c\right)^{-\frac{5}{2}} \tag{6.66}$$

In these equations, Φ_c and Φ_b are the volume fraction of crystals and bubble, respectively, relative to the liquid faction (Φ_l) and $\Phi_c + \Phi_b + \Phi_l = 1$.

Note, that the treatment of Phan-Thien and Pham (1997) does not account for textural variations and is only applicable to spherical particles. Further, it does not account for strain-rate dependent effects or allow for substitution of different models for the rheology of either component of the suspension.

In summary, while effective medium theory is a promising approach, especially in the dilute regime, this method exclusively uses models for two-phase suspensions and assumes that bubbles remain unaffected by the crystal framework or *vice versa*. The resulting effective viscosity of the multiphase suspension is then simply defined as:

$$\eta_{eff} = \eta_l \times \eta_{r,c} \times \eta_{r,b} \tag{6.67}$$

where relative viscosity of crystals and bubbles can be estimated using any of the models presented in Table 6.1 (Fig. 6.1) and in Table 6.4 (Fig. 6.7), respectively, but considering the phase fraction depending on the considered effective medium, as described above.

Bubble–crystal interactions that occur in a natural magma can therefore not be captured by this simple series of two separate models. Nonetheless, until a full three-phase rheological model is developed, effective medium treatment of multiphase suspensions can be considered the most reasonable approach, for investigation of dynamic changes in suspension rheology for example in modeling applications or for the reconstruction of the rheology of a sample recovered from the field. It is however important to be aware of the assumptions and limitations tied to the selected approach and the simplifications and generalizations that need to be made when selecting and applying the appropriate equations because the individual models for multiphase rheology are very sensitive to the required input parameters.

The yield stress dilemma

The existence of a yield stress resulting from particle–particle interactions has broadly been accepted in lava and magma rheology. The formation of such interacting particle networks varies with particle concentration, size and shape. Yield stress is observed at lower particle concentrations for higher particle aspect ratios due to the more efficient particle–particle interaction. Further, yield stress tends to be larger for smaller particles as these may easily achieve high packing densities and thus generate stronger networks (Heymann et al. 2002). A numerical attempt to define the critical particle volume fraction at which touching particle networks may form in non-sheared suspension was presented by Saar et al. (2001).

However, the existence of a yield stress *sensu stricto* has been disproven for a broad variety of materials including solids, soft solids, liquids and suspensions; for details see Barnes (1999) and references therein. It has been shown that, although many materials display a dramatic change in mechanical properties over a small range of stress (i.e., an apparent yield stress), these materials, after an initial linear elastic response to the applied stress, display steady, slow deformation (i.e., Newtonian behavior) when stressed for long times below this apparent yield stress. Barnes (1999) presents a comprehensive review on this issue and highlights that this transition from very high (creep) viscosity (>10^6 Pa s) to mobile liquid (<0.1 Pa s) may take place over a single order of magnitude in applied stress. He highlighted that, when viewed on a linear plot, this extreme behavior may easily lead to the interpretation that the material possesses a yield stress. In fact, in many cases the flow curves appear to be

adequately described by a simple Bingham equation. He noted, however, that if viewed on a logarithmic basis (Fig. 6.9), a pattern of Newtonian / power-law / Newtonian flow behavior at low / transitional / and high stresses, respectively, emerges, leading him to cite the Heraclitan expression πάντα ῥεῖ (panta rhei) "everything flows".

Although Barnes (1999) shows that yield stresses do not exist as a physical property (i.e., as a critical stress below which no flow takes place), the concept of a yield stress has proved very useful with application to magma migration and lava flow emplacement (Hulme 1974). This is largely because the radical transition in flow response rate across the apparent yield stress change zone pushes the magmatic suspension in a regime where the timescales of other processes such as heat loss and crystallization act on much faster timescales than the deformation timescale and hence the material can be treated as effectively solid under those conditions. Apparent yield stress in magmas and lavas is reported in several studies (Shaw 1969; Murase and Mc Birney 1973; Pinkerton and Stevenson 1992; Pinkerton and Norton 1995; Zhou et al. 1995; Philpotts and Carroll 1996; Cashman et al. 1999; Hoover et al. 2001; Heymann et al. 2002) but no link to experimental measurements is made. Attempts to join morphology derived yield stress estimates and model-based yield stress estimates (based on the textural properties of lavas) were presented in Chevrel et al. (2013b) and Castruccio et al. (2014). Nonetheless, care has to be taken when applying the concepts derived from experiments aimed at investigating yield stress effects (Fink and Griffiths 1992; Griffiths and Fink 1992) to natural scenarios. It should be considered, that once a lava flow crust is sufficiently solidified to hinder further advance, the flow as a whole it is still capable of deformation but behaves immobile on the time scale of observation. This point (i.e., the apparent yield stress) is therefore very valuable as limiting parameter in models considering the advance of lava flows (Dragoni et al. 1986; Harris and Rowland 2001). A further complication arises when deriving apparent yield stresses from geometrical measurements of lava flows using the approaches presented in for example Hulme (1974) or Moore et al. (1978). For these approaches to be employed accurately it is crucial to constrain the lava emplacement history, as late stage inflation (a common process in lava flows) may drastically increase the recovered apparent yield stresses (Kolzenburg et al. 2018a).

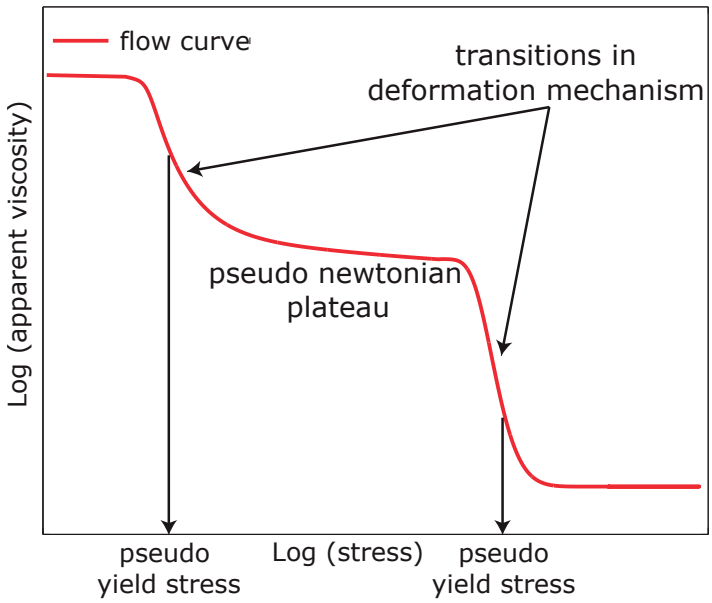

Figure 6.9. Schematic representation of an apparent viscosity measurement as a function of stress (i.e., flow curve) showing the succession of pseudo-Newtonian behavior (plateau) and transitions in deformation mechanism (increase in apparent viscosity with decreasing stress) that are frequently interpreted as pseudo yield stresses (Barnes 1999). One example would be the transition from viscous flow to crystal creep during crystallization of a sample. Since these transitions can be on the scale of up to several orders of magnitude, they frequently exceed the measurement range of a specific measurement device or geometry and are thus easily mistaken for material property limits and thus interpreted as yield strengths.

7. TECHNOLOGICAL ADVANCES

While a number of experimental methods are available for rheometry of homogenous silicate liquids, the selection becomes much more narrow for rheometry of multiphase suspensions. This is largely due to the small sample volumes or small strains that methods like fibre elongation, micro-penetration or falling body experiments, can achieve. The main technological advances for measurement of two- and three-phase suspensions have been made by enhancing the measurement capacity and accuracy of existing methods as well as by combining these measurement approaches with *in situ* imaging or sensing techniques. All these advances are rooted in the desire to better constrain the evolution of textural and thermal properties during flow and, therewith, improve the parameterization efforts reviewed earlier in this chapter.

Advances in experimental devices and methods over the past decades include:

1. High torque and high temperature concentric cylinder rheometers such as the one employed in Stein and Spera (2002). These devices allow to systematically measure the rheology of magmatic suspensions and emulsions over a wide range of viscosity and strain rate, thus generating deformation maps over a wide range of compositions and emplacement scenarios. This reduces the need for piecing together data sets from multiple methods or samples, increasing the accuracy of the results. Further, such devices permit experimentation at high total strain, which is important when considering that strain may affect the rheological response of magmatic suspensions and emulsions (Mueller et al. 2011; Ryan et al. 2019a).
2. High load and high temperature parallel plate rheometers such as the one presented in Hess et al. (2007). These devices are required for very high viscosity samples and to overcome issues of sample scaling (mainly the ratio of sample size with respect to the largest crystal or bubble). This allows for investigation of crystal sizes and size-distributions relevant to natural magmatic systems (Lavallée et al. 2007).
3. In situ thermal measurements during high temperature concentric cylinder rheometry such as developed in Kolzenburg et al. (2016). This allows simultaneous monitoring of both the rheological and thermal evolution of a crystallizing melt, expanding the capacity for measurements in thermal disequilibrium and analysis of process kinetics (Kolzenburg et al. 2018b).
4. Improved instrument capacity for in situ rheological measurements in the field (Chevrel et al. 2019a). While safe access to active lava remains difficult, enhanced (or novel) versions of field rheometers will enable increased measurement precision during three-phase rheometry of natural lavas that is required for benchmarking of analogue and high temperature laboratory experiments.

Advances in in situ imaging techniques over the past decades include high resolution X-ray computed tomography for both 3D and 4D (3D plus time) analysis of magmatic suspensions. 3D characterization has become almost a standard technique for detailed textural analyses of geologic samples, see for example Polacci et al. (2010) for a review. It has also been used for characterization of experimental samples pre- and post-deformation (Okumura et al. 2010; Shields et al. 2014; Ryan et al. 2015; Dobson et al. 2020). These have allowed investigating deformation processes recorded in natural samples at much greater detail than classic 2D petrographic methods. Wright and Weinberg (2009) for example highlight the textural heterogeneity of foamed magmas around solid particles and note profound strain localization within natural samples. They argue that strain localization may produce plug flow within ascending magmas, resulting in localized, strain-rate regime dependent fragmentation in the lead up to wholesale fragmentation of foamed magmas. 4D *in situ* textural characterization during high temperature crystallization, foaming or deformation experiments, facilitated by synchrotron tomography is a rather recent and extremely promising advancement since it allows real time monitoring of the textural evolution the investigated

samples during crystallization, foaming and deformation (Song et al. 2001; Polacci et al. 2010, 2018; Madonna et al. 2013; Arzilli et al. 2015; Pistone et al. 2015; Pleše et al. 2018; Dobson et al. 2020). Synchrotron tomography becomes especially valuable for characterization of multiphase flow since all participating components can be monitored in great spatial and temporal detail. 4D tomography is starting to be coupled with devices for rheometry, which may in the future allow for *in situ* measurement of both the crystallization kinetics and the rheological response of evolving natural systems (Dobson et al. 2020). Ohtani et al. (2005) and Raterron and Merkel (2009) presented early viscosity and density measurements of melts and glasses at high pressure and temperature in a synchrotron multi anvil apparatus. An application to natural multiphase magmatic suspensions was published by Okumura et al. (2013) who developed a new apparatus for torsion experiments at high temperature in combination with synchrotron tomography. Haboub et al. (2014) developed a new apparatus for contemporaneous synchrotron radiation tomography and high temperature deformation in compression and tension. This device was recently employed by Tripoli et al. (2019) to study the deformation dependent crystallization kinetics of basaltic melts but, unfortunately, rheological data could not be recovered since the sample was too low in viscosity. Further, a number of abstracts have been presented on 4D rheometry measurements of both natural and analogue multiphase suspensions (Dobson et al. 2016; Coats et al. 2017; Lavallée et al. 2019) but comprehensive 4D-rheological datasets have not been published to date.

8. OUTSTANDING CHALLENGES

At the end of a comprehensive review of magma rheology, McBirney and Murase (1984) noted that little is known about rates and mechanisms of flow at very low stress and over long duration and that, while the importance of thermal feedback mechanisms were identified as very important (Shaw 1969), non-isothermal data are absent. Interestingly, over 30 years later, while much has been learned about magma rheology (especially for silicate liquids) sub-liquidus rheology and the effects of disequilibrium and low stress environments remain largely uncharted. Here we can only re-iterate the concluding statement of McBirney and Murase (1984), that few fields of geological research hold greater potential for enhancing our understanding of basic magmatic and tectonic processes, an insight that was recently highlighted also with respect to the formation and dynamics of trans-crustal magma reservoirs (Sparks et al. 2019). In this chapter, we have summarized the major advances in multiphase suspension rheology of lavas, magmas and their analogues that were achieved over the past decades. Combined with advances in rheological measurement capacities, these produce a constantly growing rheological database that can be used for validation and improvement of empirical and theoretical models. However, as highlighted in the respective sections, there are a number of outstanding challenges that remain to be addressed in order to generate a holistic understanding of magma and lava flow properties. In this section we want to highlight the most notable ones.

Models for multiphase rheology

A constitutive model for bubble-bearing melts (Eqns. 6.51 and 6.52) has been developed and has been validated on a broad range of analogue suspensions. The advantage of this model is that it is based on physical theory, validated by experiments and describes both steady and unsteady flow and thus, the model parameters are directly related to physical processes. Data for magmatic bubble-bearing silicate melts are scarce. The available data have proven problematic for cross correlation with analogue measurements due to the varying nature of deformation in flowing bubble suspensions and compacting or sintering porous particulate material as well as measurement uncertainties (Fig. 6.8) and the much greater viscosity contrast between suspending liquid and the suspended gas phase. To date, few data are available that could be used to cross validate these models (specifically for magmatic suspensions) and for developing adequate experimental strategies. Consequently, providing such data remains an open challenge.

The available models for particle-bearing suspensions are almost exclusively restricted to steady flow conditions and vary widely in accuracy and applicability. Further, they are commonly restricted to narrow textural and deformational (strain and strain-rate) regimes. This is largely because the models are predominantly empirical in nature and no physical theory has been presented that links the model parameters to the physics of flow. The situation becomes worse for multiphase (bubble + crystal or polydisperse crystal-bearing) suspensions where with increasing volume fraction of bubbles or particles, the interaction between the different components becomes more important. While available models provide decent descriptions in the dilute regime (i.e., total fraction of suspended phases $\Phi_t < 0.5$), they fail at high bubble or particle fractions. For example, at $\Phi_b >$ ~0.5–0.7, bubble suspensions become foam-like, forming polyhedral cells of gas separated by thin films of liquid, which drastically changes their rheology. Equivalently, at particle contents $\Phi > \Phi_m$, the suspension transitions from viscous dominated to a range of shear localization and/or plastic deformation phenomena, which are not captured by most published models (except Costa et al. (2009) and derivate models); for details on these topics see Lavallée and Kendrick (2022, this volume). Thus, while the two-phase end-members (bubbles and particles) of suspension rheology are reasonably well-described individually, the critical future research required to form a holistic description of natural magmas and lavas needs to address the physics and disequilibrium dynamics involved in three-phase rheology, including polydisperse size-distribution and the interaction between bubbles and particles.

Reactive flow and phase dynamics

Most current parameterization efforts assume that the solid and/or bubble fraction has no physical or chemical relation to the liquid in which it is suspended. This is very clearly not the case for magmas and lavas, that are reactive materials, where both crystals and bubbles nucleate and grow during cooling and decompression. These reactions change the textural state as well as the chemical composition and the rheological behavior of the liquid. The magnitude of this effect heavily depends on the initial melt composition and the nature and phase dynamics of the growing crystals, all of which vary as a function of the environmental conditions. The viscosity changes induced by the chemical evolution of the melt may be as small as < 0.1 log units in basaltic lavas, where initially, crystallization does not increase the residual silica content by much but can be much greater than the effect of the suspended crystals once the residual melt becomes more evolved and silica rich. While the fundamental importance of disequilibrium has been recognized early on, data availability remains scarce and significant experimental effort in this field is still required to cover the most relevant compositions and to experimentally map the range of environmental parameters pertinent to flow of natural silicate melts under disequilibrium. Such a database would then allow deducing the underlying process systematics and expanding these into a theoretical description of the flow behavior of magma and lava that includes crystallization kinetics and diffusion of elements between the melt and the suspended solid and gas phases. Such a complete viscosity model of a crystallizing magma would need to include multidimensional rheologic maps (i.e., and expansion of Figs. 4.5 and 4.6 as a 4 or 5 dimensional TTT–rheology diagram that includes variations in stress and strain-rate).

Additionally, a parameter that remains entirely unexplored for natural silicate melt suspension rheology and is only scarcely touched upon for the rheology of analogue suspensions is the effect of bubble dynamics under elevated and changing pressure conditions. As outlined in this chapter, pressure changes modulate the phase dynamics of both gas and crystal phases and are thus critical to the understanding of the rheology of a crystallizing magma during its journey from source to surface. Systematic exploration of the effect of pressure will require rheological measurements during decompression to reproduce the natural dynamics of bubble and crystal nucleation and growth. This goal will, in future research, benefit greatly from the advances in tomographic methods, as these allow tracking the physical phase evolution of magma in 4D.

Filling data gaps

Analogue suspension experiments have covered the largest part of suspension textures encountered in the field. For natural magmatic suspensions at high temperature, however, the data are much more limited. Measurements on natural magmatic particle suspensions are becoming more numerous but they predominantly cover basaltic compositions and rather low viscosities (with $\eta \lesssim 10^4$ Pas). Measurements on high viscosity systems (with $\eta \gtrsim 10^8$ Pas) and bubble-bearing melts are only slowly becoming available and there is a marked gap in compositions and textures in the intermediate field (see Fig. 4.2). This limited coverage of the intermediate range largely reflects the mechanical limitations of the available rheometers and highlights that the development of advanced rheometers, able to cover a wider range of torque, is critical to cover the gap between low torque–high strain concentric cylinder and high load–low strain parallel plate measurements. The current inconsistency between these two methods is not least due to the limitations in total strain that can be imposed in uniaxial compression or in torsion.

Another major limitation to generating a complete understanding of multiphase magma rheology is that research to date largely focused on two-phase suspensions. The advances in two phase suspension rheology that were made over the past decades have now reached a point at which there is sufficiently detailed knowledge to tackle the next greater challenge, that is, the rheology of three-phase magmas (i.e., with suspended bubbles and crystals). Doing so will require an expanded experimental capacity to build a dataset capturing the additional complexities of the physics involved in the interaction between bubbles and particles. Several groups have started to tackle these challenges (Harris and Allen 2008; Caricchi et al. 2011; Pistone et al. 2012; Chevrel et al. 2013b; Shields et al. 2014; Truby et al. 2015; Vasseur et al. 2015; Pistone et al. 2016; Vona et al. 2017) but there is a vast open field of environmental parameters that remains to be explored.

Further, in order to connect the theoretical and experimental insights on multiphase magma rheology to natural flow scenarios it is important that the distinct lack of *in situ* field measurements of lava rheology is addressed. These are currently limited largely due to the logistical and technical difficulties as well as the hazards associated with collecting these data. Expansion of this slim dataset and the narrow range of measurable conditions would be a significant advancement, as these allow for combined rheological, textural and petrographic analysis. These measurements are key to understanding how crystal and bubble content and their temporal and spatial variation affect rheology during lava emplacement. Future field campaigns should, thus, focus on measuring the relevant lava properties (e.g., temperature, rheology and lava texture) as a function of distance from the vent to the front and across the flow, in order to map lava rheology in 4D through the flow. Field measurements will always be constrained by the balance between measurement machinery (Fig. 5.4) and the lava's thermal dynamics. Thus, it is necessary to develop advanced equipment for field measurement that is readily deployable while also improving the measurement uncertainty. The most suitable way to achieving this is likely a combination of rotational and penetration rheometers that allow covering the broad range of viscosities and thermal regimes encountered in nature.

Connecting magma rheology and rock mechanics

Most rheological models for multiphase suspensions break down beyond the semi-dilute regime where, at geologically relevant stresses and strain rates, a transition from the viscous to the elastic field is documented. Costa et al. (2009) and Liu et al. (2017) proposed the first models aiming to account for this transition zone but experimental data for the validation of these models across the entire range of suspended particle factions is unavailable to date. The above review of recent field and laboratory studies of the rheological properties of natural silicate melts highlights that, at present, viscosity and yield stress are treated as separate properties. However, as outlined in the section "the yield stress dilemma", these two properties are closely related and represent two components of the much broader phenomenon of deformation of

igneous rocks and melts at high temperature. An upcoming challenge therefore is to generate cross disciplinary datasets that will be able to connect the fields of rheology, rock mechanics, volcanology and numerical modeling.

Exploiting multidisciplinary datasets

While theoretical and more complex and complete descriptions of multiphase rheology are continuously being developed, their application fundamentally relies on parameters that are non-quantifiable prior to or during eruption (e.g., particle size, shape, aspect ratio, surface roughness) and that constantly evolve during transport of the magmatic suspension beneath or at the Earth's surface. Hence, their applicability to hazard forecasting or the prediction of eruption dynamics during or in preparation for volcanic crises is extremely limited. One of the large outstanding challenges is to develop rheological descriptions that robustly describe the flow of magma and lava across geologically relevant parameter space and that can be tied to data that can readily be measured during volcanic activity. For example, Coppola et al. (2013) introduced an empirical approach tying satellite derived radiant density measurements to the bulk rheology of lava. When applied at sufficiently high resolution and with high acquisition frequency (minutes to hours), this is a promising approach to inform emplacement models in near real time (Harris et al. 2019). However, to date, few attempts have been made to cross-correlate satellite, field- and laboratory measurements (Harris et al. 2019). Such a cross correlation would be very valuable in order to render the satellite derived data applicable to near real time hazard assessment and forecasting.

Further, combination of the recent laboratory developments and the growing availability of complementary datasets from a range of sub-disciplines (e.g., tomography, remote-sensing, drone technology, high-speed computation facilities) may lead to a more in depth understanding of magma and lava transport. These are beginning to be employed and tested in concert on long lasting (e.g., Chaiten, 2008–2010; Holuhraun, 2014–2015; Hawaii, 2018), or frequent, short duration (Piton de la Fournaise) lava flow eruptions, which are proving to be spectacular opportunities to perform interdisciplinary studies. Merging these interdisciplinary datasets promises to stimulate the development of new and enhanced tools for near real-time monitoring and forecasting of volcanic activity.

Characterizing nanoscale processes

In this review particle size was only mentioned when presenting the effect of polydisperse crystal size distributions. However, it has become apparent that nanolites (crystals at scales smaller than about 100 nanometers) can impact volcanic processes by affecting the viscosity of magmatic suspensions as well as by modulating gas exsolution. (Sharp et al. 1996) first identified nanometer scale crystallinity in natural volcanic glasses using transmission electron microscopy (TEM) observations. They coined the phrase "nanolites" for this previously unnoticed component of the grain size distribution in eruptive products and observed that it was a grain size distribution distinct from the commonly observed microlite size distribution. Nanolite bearing glasses frequently appear to be homogenous glasses to the naked eye and to the most common micro analysis techniques, such as scanning electron microscopes (SEM) and electron probes (EPMA). In recent years the presence of nanolites has been confirmed in a wide range of eruptive and experimental products using TEM or other nanoscale observations such as Raman spectroscopy (Barone et al. 2016; Burgess et al. 2016; Di Genova et al. 2018; Mujin and Nakamura 2014). Nanolites have been shown to affect important volcanic processes such as bubble nucleation (Cáceres et al. 2020; Di Genova et al. 2020; Kolzenburg et al. 2020) and, with that, changes in volcanic explosivity and rheological transitions due to vesiculation and/or crystal growth (Bouhifd et al. 2004; Di Genova et al. 2020; Liebske et al. 2003; Mujin et al. 2017; Villeneuve et al. 2008). While it had been suggested previously that very fine particles can have a stronger effect on suspension rheology than an equal amount of larger particles for both geological suspensions (Del Gaudio et al. 2013) and synthetic

suspensions (Rudyak 2013; Taylor et al. 2013), recent research suggests that this effect may be even stronger for nano scale particles either due to the effect of crystal growth on the melt structure (Di Genova et al. 2017) or due to physical / geometrical effects, where aggregates of a large number of fine particles act to immobilize a significantly larger volume of melt in their interstitial space than an equal volume fraction of larger particles (Di Genova et al. 2020). Little is known about the exact processes that cause these size dependent effects and we will likely see an emerging body of literature on this topic concerned with geological melts forming over the coming decade.

ACKNOWLEDGMENTS

We thank Satoshi Okumura, Grant Henderson and an anonymous reviewer for constructive comments that helped improve this chapter. We are also grateful for discussions with many friends and colleagues on the topic of magma and lava rheology that helped generate a broad overview over this topic. SK acknowledges the support of a H2020 Marie Skłodowska-Curie fellowship DYNAVOLC – No.795044. MOC acknowledges the Agence National de la Recherche through the project LAVA (Program: DS0902 2016; Project: ANR-16 CE39-0009); this is ANR-LAVA contribution no. 17 and it is Laboratory of Excellence ClerVolc contribution number 479. DBD acknowledges the support of ERC 2018 Advanced Grant 834225 (EAVESDROP).

REFERENCES

Arbaret L, Bystricky M, Champallier R (2007) Microstructures and rheology of hydrous synthetic magmatic suspensions deformed in torsion at high pressure. J Geophys Res: Solid Earth 112:B10208

Arzilli F, Carroll MR (2013) Crystallization kinetics of alkali feldspars in cooling and decompression-induced crystallization experiments in trachytic melt. Contrib Mineral Petrol 166:1011–1027

Arzilli F, Mancini L, Voltolini M, Cicconi MR, Mohammadi S, Giuli G, Mainprice D, Paris E, Barou F, Carroll MR (2015) Near-liquidus growth of feldspar spherulites in trachytic melts: 3D morphologies and implications in crystallization mechanisms. Lithos 216–217:93–105

Arzilli F, Polacci M, La Spina G, Le Gall N, Cai B, Hartley M, Di Genova D, Vo N, Bamber E, Nonni S (2018) Rapid growth of plagioclase: implications for basaltic Plinian eruption. EGU GeneralAssembly 13431

Avard G, Whittington AG (2012) Rheology of arc dacite lavas: experimental determination at low strain rates. Bull Volcanol 74:1039–1056

Bachmann O, Huber C (2016) Silicic magma reservoirs in the Earth's crust. Am Mineral 101:2377–2404

Bagdassarov N, Dingwell DB (1992) A rheological investigation of vesicular rhyolite. J Volcanol Geotherm Res:307–322

Bagdassarov N, Pinkerton H (2004) A review and investigation of the Non-Newtonian properties of lavas based on laboratory experiments with analogue materials. J Volcanol Geotherm Res 132:115–136

Bagdassarov N, Dorfman A, Dingwell DB (2000) Effect of alkalis, phosphorus, and water on the surface tension of haplogranite melt. Am Mineral 85:33–40

Bagdassarov NS, Dingwell DB (1993a) Deformation of foamed rhyolites under internal and external stresses: an experimental investigation. Bull Volcanol 55:147–154

Bagdassarov NS, Dingwell DB (1993b) Frequency dependent rheology of vesicular rhyolite. J Geophys Res: Solid Earth 98:6477–6487

Bagdassarov NS, Dingwell DB, Webb SL (1994) Viscoelasticity of crystal- and bubble-bearing rhyolite melts. Phys Earth Planet Inter 83:83–99

Barnes HA (1997) Thixotropy—a review. J Non-Newtonian Fluid Mech 70:1–33

Barnes HA (1999) The yield stress—a review or 'παντα ρει'—everything flows? J Non-Newtonian Fluid Mech 81:133–178

Barone G, Mazzoleni P, Corsaro RA, Costagliola P, Di Benedetto F, Ciliberto E, Gimeno D, Bongiorno C, Spinella C (2016) Nanoscale surface modification of Mt. Etna volcanic ashes. Geochim Cosmochim Acta 174:70–84

Beckett F, Burton M, Mader H, Phillips J, Polacci M, Rust A, Witham F (2014) Conduit convection driving persistent degassing at basaltic volcanoes. J Volcanol Geotherm Res 283:19–35

Belousov A, Belousova M (2018) Dynamics and viscosity of 'a'a and pahoehoe lava flows of the 2012–2013 eruption of Tolbachik volcano, Kamchatka (Russia). Bull Volcanol 80:6

Blundy J, Cashman K, Humphreys M (2006) Magma heating by decompression-driven crystallization beneath andesite volcanoes. Nature 443:76

Bouhifd MA, Richet P, Besson P, Roskosz M, Ingrin J (2004) Redox state, microstructure and viscosity of a partially crystallized basalt melt. Earth Planet Sci Lett 218:31–44
Burgess KD, Stroud RM, Dyar MD, McCanta MC (2016) Submicrometer-scale spatial heterogeneity in silicate glasses using aberration-corrected scanning transmission electron microscopy. Am Mineral 101:2677–2688
Cáceres F, Wadsworth FB, Scheu B, Colombier M, Madonna C, Cimarelli C, Hess K-U, Kaliwoda M, Ruthensteiner B, Dingwell DB (2020) Can nanolites enhance eruption explosivity? Geology 48:997–1001
Campagnola S, Vona A, Romano C, Giordano G (2016) Crystallization kinetics and rheology of leucite-bearing tephriphonolite magmas from the Colli Albani volcano (Italy). Chem Geol 424:12–29
Caricchi L, Burlini L, Ulmer P, Gerya T, Vassalli M, Papale P (2007) Non-Newtonian rheology of crystal-bearing magmas and implications for magma ascent dynamics. Earth Planet Sci Lett 264:402–419
Caricchi L, Pommier A, Pistone M, Castro J, Burgisser A, Perugini D (2011) Strain-induced magma degassing: insights from simple-shear experiments on bubble bearing melts. Bull Volcanol 73:1245–1257
Cashman KV, Thornber C, Kauahikaua JP (1999) Cooling and crystallization of lava in open channels, and the transition of Pāhoehoe Lava to 'a'ā. Bull Volcanol 61:306–323
Cashman KV, Sparks RSJ, Blundy JD (2017) Vertically extensive and unstable magmatic systems: A unified view of igneous processes. Science 355
Castruccio A, Rust AC, Sparks RSJ (2010) Rheology and flow of crystal-bearing lavas: Insights from analogue gravity currents. Earth Planet Sci Lett 297:471–480
Castruccio A, Rust A, Sparks R (2014) Assessing lava flow evolution from post-eruption field data using Herschel–Bulkley rheology. J Volcanol Geotherm Res 275:71–84
Champallier R, Bystricky M, Arbaret L (2008) Experimental investigation of magma rheology at 300 MPa: From pure hydrous melt to 76 vol.% of crystals. Earth Planet Sci Lett 267:571–583
Chester DK, Duncan AM, Guest JE, Kilburn C (2012) Mount Etna: the Anatomy of a Volcano. Springer Science and Business Media
Chevrel MO, Pinkerton H, Harris AJL (2019a) Measuring the viscosity of lava in the field: A review. Earth Sci Rev 196:102852
Chevrel MO, Baratoux D, Hess K-U, Dingwell DB (2014) Viscous flow behavior of tholeiitic and alkaline Fe-rich martian basalts. Geochim Cosmochim Acta 124:348–365
Chevrel MO, Giordano D, Potuzak M, Courtial P, Dingwell DB (2013a) Physical properties of $CaAl_2Si_2O_8$–$CaMgSi_2O_6$–FeO–Fe_2O_3 melts: Analogues for extra-terrestrial basalt. Chem Geol 346:93–105
Chevrel MO, Platz T, Hauber E, Baratoux D, Lavallée Y, Dingwell DB (2013b) Lava flow rheology: A comparison of morphological and petrological methods. Earth Planet Sci Lett 384:109–120
Chevrel MO, Harris AJ, James MR, Calabrò L, Gurioli L, Pinkerton H (2018) The viscosity of pāhoehoe lava: in situ syn-eruptive measurements from Kilauea, Hawaii 2. Earth Planet Sci Lett
Chevrel MO, Harris A, Ajas A, Biren J, Gurioli L, Calabrò L (2019b) Investigating physical and thermal interactions between lava and trees: the case of Kīlauea's July 1974 flow. Bull Volcanol 81:6
Chevrel MO, Cimarelli C, deBiasi L, Hanson JB, Lavallée Y, Arzilli F, Dingwell DB (2015) Viscosity measurements of crystallizing andesite from Tungurahua volcano (Ecuador). Geochem Geophys Geosystems 16:870–889
Chong J, Christiansen E, Baer A (1971) Rheology of concentrated suspensions. J Appl Polym Sci 15:2007–2021
Cimarelli C, Costa A, Mueller S, Mader HM (2011) Rheology of magmas with bimodal crystal size and shape distributions: Insights from analog experiments. Geomchem Geophys Geosyst 12:Q07024
Coats R, Kendrick JE, Wallace PA, Miwa T, Hornby AJ, Ashworth JD, Matsushima T, Lavallée Y (2018) Failure criteria for porous dome rocks and lavas: a study of Mt. Unzen, Japan. Solid Earth 9:1299–1328
Coats R, Cai B, Kendrick J, Wallace P, Hornby A, Miwa T, von Aulock F, Ashworth J, Godinho J, Atwood R (2017) Understanding the rheology of two and three-phase magmas. AGU Fall Meeting Abstracts
Coish R, Taylor LA (1979) The effects of cooling rate on texture and pyroxene chemistry in DSDP Leg 34 basalt: a microprobe study. Earth Planet Sci Lett 42:389–398
Coppola D, Laiolo M, Piscopo D, Cigolini C (2013) Rheological control on the radiant density of active lava flows and domes. J Volcanol Geotherm Res 249:39–48
Coppola D, Ripepe M, Laiolo M, Cigolini C (2017) Modelling satellite-derived magma discharge to explain caldera collapse. Geology 45:523–526
Cordonnier B, Hess KU, Lavallée Y, Dingwell DB (2009) Rheological properties of dome lavas: Case study of Unzen volcano. Earth Planet Sci Lett 279:263–272
Cordonnier B, Schmalholz S, Hess KU, Dingwell D (2012a) Viscous heating in silicate melts: An experimental and numerical comparison. J Geophys Res: Solid Earth (1978–2012) 117:B02203
Cordonnier B, Caricchi L, Pistone M, Castro J, Hess K-U, Gottschaller S, Manga M, Dingwell D, Burlini L (2012b) The viscous-brittle transition of crystal-bearing silicic melt: Direct observation of magma rupture and healing. Geology 40:611–614
Costa A (2005) Viscosity of high crystal content melts: dependence on solid fraction. Geophys Res Lett 32:L22308
Costa A, Caricchi L, Bagdassarov N (2009) A model for the rheology of particle-bearing suspensions and partially molten rocks. Geomchem Geophys Geosyst 10:Q03010

Couch S, Sparks R, Carroll M (2003) The kinetics of degassing-induced crystallization at Soufriere Hills Volcano, Montserrat. J Petrol 44:1477–1502
Coussot P, Ancey C (1999) Rheophysical classification of concentrated suspensions and granular pastes. Phys Rev E 59:4445–4457
Cross MM (1965) Rheology of non-Newtonian fluids: a new flow equation for pseudoplastic systems. J Colloid Sci 20:417–437
Cukierman M, Tutts P, Uhlmann D (1972) Viscous flow behavior of lunar compositions 14259 and 14310. Lunar Planet Sci Conf Proc 3:2619
Del Gaudio P (2014) Rheology of bimodal crystals suspensions: Results from analogue experiments and implications for magma ascent. Geomchem Geophys Geosyst 15:284–291
Del Gaudio P, Ventura G, Taddeucci J (2013) The effect of particle size on the rheology of liquid–solid mixtures with application to lava flows: Results from analogue experiments. Geomchem Geophys Geosyst 14:2661–2669
Deubelbeiss Y, Kaus BJ, Connolly JA, Caricchi L (2011) Potential causes for the non-Newtonian rheology of crystal-bearing magmas. Geomchem Geophys Geosyst 12:Q05007
Di Genova D, Kolzenburg S, Wiesmaier S, Dallanave E, Neuville DR, Hess KU, Dingwell DB (2017) A compositional tipping point governing the mobilization and eruption style of rhyolitic magma. Nature 552:235
Di Genova D, Caracciolo A and Kolzenburg S (2018) Measuring the degree of "nanotilization" of volcanic glasses: Understanding syn-eruptive processes recorded in melt inclusions. Lithos 318–319:209–218
Di Genova D, Brooker RA, Mader HM, Drewitt JWE, Longo A, Deubener J, Neuville DR, Fanara S, Shebanova O, Anzellini S, Arzilli F, Bamber EC, Hennet L, La Spina G, Miyajima N (2020) In situ observation of nanolite growth in volcanic melt: A driving force for explosive eruptions. Sci Adv 6: eabb0413
Dietterich HR, Downs DT, Stelten ME, Zahran H (2018) Reconstructing lava flow emplacement histories with rheological and morphological analyses: the Harrat Rahat volcanic field, Kingdom of Saudi Arabia. Bull Volcanol 80:85
Dingwell D (1991) Redox viscometry of some Fe-bearing silicate melts. Am Mineral 76:1560–1562
Dingwell DB (1986) Viscosity-temperature relationships in the system $Na_2Si_2O_5$–$Na_4Al_2O_5$. Geochim Cosmochim Acta 50:1261–1265
Dingwell DB, Virgo D (1987) The effect of oxidation state on the viscosity of melts in the system Na_2O–FeO–Fe_2O_3–SiO_2. Geochim Cosmochim Acta 51:195–205
Dingwell DB, Virgo D (1988) Viscosities of melts in the Na_2O–FeO–Fe_2O_3–SiO_2 system and factors controlling relative viscosities of fully polymerized silicate melts. Geochim Cosmochim Acta 52:395–403
Dingwell DB, Webb SL (1989) Structural relaxation in silicate melts and non-Newtonian melts rheology in geologic processes. Phys Chem Mineral 16:508–516
Dobson K, Wadsworth F, Di Genova D, Kolzenburg S, Vasseur J, Marone F, Dingwell D (2016) Magmas on the move: in situ 4d experimental investigation into the rheology and mobility of three-phase magmas using ultra fast X-ray tomography. AGU Fall Meeting Abstracts
Dobson KJ, Allabar A, Bretagne E, Coumans J, Cassidy M, Cimarelli C, Coats R, Connolley T, Courtois L, Dingwell DB, Di Genova D (2020) Quantifying microstructural evolution in moving magma. Front Earth Sci 8:287
Dragoni M, Tallarico A (1994) The effect of crystallization on the rheology and dynamics of lava flows. J Volcanol Geotherm Res 59:241–252
Dragoni M, Bonafede M, Boschi E (1986) Downslope flow models of a Bingham liquid: implications for lava flows. J Volcanol Geotherm Res 30:305–325
Ducamp VC, Raj R (1989) Shear and densification of glass powder compacts. J Am Ceram Soc 72:798–804
Eilers H (1943) Die viskositäts-konzentrationsabhängigkeit kolloider Systeme in organischen Lösungsmitteln. Kolloid-Z 102:154–169
Eilers vH (1941) Die viskosität von Emulsionen hochviskoser Stoffe als Funktion der Konzentration. Kolloid Z 97:313–321
Einarsson T (1949) Studies of the Pleistocene in Eyjafjörður, Middle Northern Iceland. Prentsmiðjan Leiftur
Einarsson T (1966) Studies of temperature, viscosity, density and some types of materials produced in the Surtsey eruption. Surtsey Res Progr Rep 1:163–179
Einstein A (1906) Eine neue Bestimmung der Moleküldimensionen. Ann Phys 324:289–306
Evans K, Gibson A (1986) Prediction of the maximum packing fraction achievable in randomly oriented short-fibre composites. Compos Sci Technol 25:149–162
Faroughi SA, Huber C (2015) A generalized equation for rheology of emulsions and suspensions of deformable particles subjected to simple shear at low Reynolds number. Rheol Acta 54:85–108
Farris R (1968) Prediction of the viscosity of multimodal suspensions from unimodal viscosity data. Trans Soc Rheol 12:281–301
Findley WN, Lai JS, Onaran K, Christensen R (1977) Creep and Relaxation of nonlinear viscoelastic materials with an introduction to linear viscoelasticity. American Society of Mechanical Engineers Digital Collection
Fink JH, Zimbelman JR (1986) Rheology of the 1983 Royal Gardens basalt flows, Kilauea volcano, Hawaii. Bull Volcanol 48:87–96
Fink JH, Griffiths RW (1992) A laboratory analog study of the surface morphology of lava flows extruded from point and line sources. J Volcanol Geotherm Res 54:19–32
Flynn LP, Mouginis-Mark PJ (1992) Cooling rate of an active Hawaiian lava flow from nighttime spectroradiometer measurements. Geophys Res Lett 19:1783–1786
Frankel N, Acrivos A (1970) The constitutive equation for a dilute emulsion. J Fluid Mech 44:65–78

Gamble RP, Taylor LA (1980) Crystal/liquid partitioning in augite: effects of cooling rate. Earth Planet Sci Lett 47:21–33
Gan M, Gopinathan N, Jia X, Williams RA (2004) Predicting packing characteristics of particles of arbitrary shapes. KONA Powder Part J 22:82–93
Gauthier F (1971) Etude comparative des caractéristiques rhéologiques de laves basaltiques en laboratoire et dur le terrain (Doctoral dissertation).
Gauthier F, Guest JE, Skelhorn RR (1973) Mount Etna and the 1971 eruption - Field and laboratory studies of the rheology of Mount Etna lava. Phil Trans R Soc London Ser A 274:83–98
Gay E, Nelson P, Armstrong W (1969) Flow properties of suspensions with high solids concentration. AIChE J 15:815–822
Gent A (1960) Theory of the parallel plate viscometer. Br J Appl Phys 11:85
Giordano D, Nichols ARL, Dingwell DB (2005) Glass transition temperatures of natural hydrous melts: a relationship with shear viscosity and implications for the welding process. J Volcanol Geotherm Res 142:105–118
Giordano D, Russell JK, Dingwell DB (2008a) Viscosity of magmatic liquids: A model. Earth Planet Sci Lett 271:123–134
Giordano D, Potuzak M, Romano C, Dingwell DB, Nowak M (2008b) Viscosity and glass transition temperature of hydrous melts in the system CaAl2Si2O8–CaMgSi2O6. Chem Geol 256:203–215
Giordano D, Polacci M, Longo A, Papale P, Dingwell DB, Boschi E, Kasereka M (2007) Thermo-rheological magma control on the impact of highly fluid lava flows at Mt. Nyiragongo. Geophys Res Lett 34:L06301
Gottsmann J, Giordano D, Dingwell DB (2002) Predicting shear viscosity during volcanic processes at the glass transition: a calorimetric calibration. Earth Planet Sci Lett 198:417–427
Griffiths RW, Fink JH (1992) The morphology of lava flows in planetary environments: Predictions from analog experiments. J Geophys Res 97(B13):19739–19748
Gualda GA, Ghiorso MS, Lemons RV, Carley TL (2012) Rhyolite-MELTS: a modified calibration of MELTS optimized for silica-rich, fluid-bearing magmatic systems. J Petrol 53:875–890
Guth E, Gold O (1938) Viscosity and electroviscous effect of the AgI sol. II. Influence of the concentration of AgI and of electrolyte on the viscosity. Phys Rev 53:322
Haboub A, Bale HA, Nasiatka JR, Cox BN, Marshall DB, Ritchie RO, MacDowell AA (2014) Tensile testing of materials at high temperatures above 1700 °C with in situ synchrotron X-ray micro-tomography. Rev Sci Instrum 85:083702
Hamilton D, Burnham CW, Osborn E (1964) The solubility of water and effects of oxygen fugacity and water content on crystallization in mafic magmas. J Petrol 5:21–39
Hammer JE (2004) Crystal nucleation in hydrous rhyolite: Experimental data applied to classical theory. Am Mineral 89:1673–1679
Hammer JE (2006) Influence of fO_2 and cooling rate on the kinetics and energetics of Fe-rich basalt crystallization. Earth Planet Sci Lett 248:618–637
Hammer JE (2008) Experimental studies of the kinetics and energetics of magma crystallization. Rev Mineral Geochem 69:9–59
Hammer JE, Rutherford MJ (2002) An experimental study of the kinetics of decompression-induced crystallization in silicic melt. J Geophys Res: Solid Earth 107:ECV 8-1:8–24
Harris A, Rowland S (2009) Effusion rate controls on lava flow length and the role of heat loss: a review. Studies in volcanology: the legacy of George Walker Special Publications of IAVCEI 2:33–51
Harris AJ, Rowland S (2001) FLOWGO: a kinematic thermo-rheological model for lava flowing in a channel. Bull Volcanol 63:20–44
Harris AJ, Chevrel MO, Coppola D, Ramsey M, Hrysiewicz A, Thivet S, Villeneuve N, Favalli M, Peltier A, Kowalski P (2019) Validation of an integrated satellite-data-driven response to an effusive crisis: the April–May 2018 eruption of Piton de la Fournaise. Ann Geophys, Istituto Nazionale di Geofisica e Volcanologia 61: 10.4401/ag-7972
Harris AJL, Flynn LP, Matias O, Rose WI, Cornejo J (2004) The evolution of an active silicic lava flow field: an ETM+ perspective. J Volcanol GeothermRes 135:147–168
Hashin Z, Shtrikman S (1963) A variational approach to the theory of the elastic behaviour of multiphase materials. J Mech Phys Solids 11:127–140
Hatschek E (1911) Die Viskosität der Dispersoide. Colloid Polym Sci 8:34–39
Heap MJ, Kolzenburg S, Russell JK, Campbell ME, Welles J, Farquharson JI, Ryan A (2014) Conditions and timescales for welding block-and-ash flow deposits. J Volcanol Geotherm Res 289:202–209
Herd CD (2003) The oxygen fugacity of olivine-phyric martian basalts and the components within the mantle and crust of Mars. Meteorit Planet Sci 38:1793–1805
Herschel W, Bulkley R (1926) Measurement of consistency as applied to rubber-benzene solutions. *In:* Measurement of Consistency as Applied to Rubber–Benzene Solutions. Vol 26, p 621–633
Hess K, Dingwell D (1996) Viscosities of hydrous leucogranitic melts: A non-Arrhenian model. Am Mineral 81:1297–1300
Hess K-U, Cordonnier B, Lavallée Y, Dingwell DB (2007) High-load, high-temperature deformation apparatus for synthetic and natural silicate melts. Rev Sci Instrum 78:075102.
Hess K-U, Cordonnier B, Lavallée Y, Dingwell DB (2008) Viscous heating in rhyolite: An in situ experimental determination. Earth Planet Sci Lett 275:121–126
Heymann L, Peukert S, Aksel N (2002) On the solid–liquid transition of concentrated suspensions in transient shear flow. Rheol Acta 41:307–315

Hobiger M, Sonder I, Büttner R, Zimanowski B (2011) Viscosity characteristics of selected volcanic rock melts. J Volcanol Geotherm Res 200:27–34
Hon K, Kauahikaua J, Denlinger R, Mackay K (1994) Emplacement and inflation of pahoehoe sheet flows: Observations and measurements of active lava flows on Kilauea Volcano, Hawaii. Geol Soc Am Bull 106:351–370
Hoover SR, Cashman KV, Manga M (2001) The yield strength of subliquidus basalts—experimental results. J Volcanol Geotherm Res 107:1–18
Hulme G (1974) The Interpretation of Lava Flow Morphology. Geophy J Inter 39:361–383
Humphreys MCS, Menand T, Blundy JD, Klimm K (2008) Magma ascent rates in explosive eruptions: Constraints from H_2O diffusion in melt inclusions. Earth Planet Sci Lett 270:25–40
Huppert HE, Sparks RSJ, Turner JS, Arndt NT (1984) Emplacement and cooling of komatiite lavas. Nature 309:19–22
Hurwitz S, Navon O (1994) Bubble nucleation in rhyolitic melts: Experiments at high pressure, temperature, and water content. Earth Planet Sci Lett 122:267–280
Ishibashi H (2009) Non-Newtonian behavior of plagioclase-bearing basaltic magma: Subliquidus viscosity measurement of the 1707 basalt of Fuji volcano, Japan. J Volcanol Geotherm Res 181:78–88
Ishibashi H, Sato H (2007) Viscosity measurements of subliquidus magmas: Alkali olivine basalt from the Higashi-Matsuura district, Southwest Japan. J Volcanol Geotherm Res 160:223–238
Ishibashi H, Sato H (2010) Bingham fluid behavior of plagioclase-bearing basaltic magma: Reanalyses of laboratory viscosity measurements for Fuji 1707 basalt. J Mineral Petrol Sci 105:334–339
James MR, Pinkerton H, Robson S (2007) Image-based measurement of flux variation in distal regions of active lava flows. Geomchem Geophys Geosyst 8:Q03006
James MR, Bagdassarov N, Müller K, Pinkerton H (2004) Viscoelastic behaviour of basaltic lavas. J Volcanol Geotherm Res 132:99–113
Jamieson RA, Unsworth MJ, Harris NB, Rosenberg CL, Schulmann K (2011) Crustal melting and the flow of mountains. Elements 7:253–260
Jellinek AM, Bercovici D (2011) Seismic tremors and magma wagging during explosive volcanism. Nature 470:522–525
Jones TJ, Llewellin EW (2021) Convective tipping point initiates localization of basaltic fissure eruptions. Earth Planet Sci Lett 553:116637
Kavanagh JL, Engwell SL, Martin SA (2018) A review of laboratory and numerical modelling in volcanology. Solid Earth 9:531–571
Kendrick J, Lavallée Y, Mariani E, Dingwell D, Wheeler J, Varley N (2017) Crystal plasticity as an indicator of the viscous–brittle transition in magmas. Nature Commun 8:1–12
Kilburn CR, Lopes RM (1991) General patterns of flow field growth: Aa and blocky lavas. J Geophys Res: Solid Earth 96:19721–19732
Kilgour G, Mader H, Blundy J, Brooker R (2016) Rheological controls on the eruption potential and style of an andesite volcano: A case study from Mt. Ruapehu, New Zealand. J Volcanol Geotherm Res 327:273–287
Klein J, Mueller SP, Castro JM (2017) The influence of crystal size distributions on the rheology of magmas: New insights from analog experiments. Geomchem Geophys Geosyst 18:4055–4073
Klein J, Mueller SP, Helo C, Schweitzer S, Gurioli L, Castro JM (2018) An expanded model and application of the combined effect of crystal-size distribution and crystal shape on the relative viscosity of magmas. J Volcanol Geotherm Res 357:128–133
Kohlstedt DL, Zimmerman ME (1996) Rheology of partially molten mantle rocks. Ann Rev Earth Planet Sci 24:41–62
Kolzenburg S, Giordano D, Cimarelli C, Dingwell DB (2016) In Situ thermal characterization of cooling/crystallizing lavas during rheology measurements and implications for lava flow emplacement. Geochim Cosmochim Acta:244–258
Kolzenburg S, Jaenicke J, Münzer U, Dingwell DB (2018a) The effect of inflation on the morphology-derived rheological parameters of lava flows and its implications for interpreting remote sensing data —A case study on the 2014/2015 eruption at Holuhraun, Iceland. J Volcanol Geotherm Res 357:200–212
Kolzenburg S, Giodano D, Hess KU, Dingwell DB (2018b) Shear rate-dependent disequilibrium rheology and dynamics of basalt solidification. Geophys Res Lett 45:6466–6475
Kolzenburg S, Giordano D, Di Muro A, Dingwell DB (2019) Equilibrium viscosity and disequilibrium rheology of a high magnesium basalt from piton De La Fournaise volcano, La Reunion, Indian Ocean, France. Ann Geophys 62:218
Kolzenburg S, Hess K-U, Berlo K, Dingwell DB (2020) Disequilibrium rheology and crystallization kinetics of basalts and implications for the Phlegrean volcanic district. Front Earth Sci 8:187
Kolzenburg S, Berlo K, Dingweil DB (2020) Vesiculation kinetics of variably crystalline rhyolites, Goldschmidt. Geochemical Society of America, Hawaii
Kolzenburg S, Giordano D, Thordarson T, Höskuldsson A, Dingwell DB (2017) The rheological evolution of the 2014/2015 eruption at Holuhraun, central Iceland. Bull Volcanol 79:45
Kolzenburg S, Di Genova D, Giordano D, Hess KU, Dingwell DB (2018c) The effect of oxygen fugacity on the rheological evolution of crystallizing basaltic melts. Earth Planet Sci Lett 487:21–32
Kouchi A, Tsuchiyama A, Sunagawa I (1986) Effect of stirring on crystallization kinetics of basalt: texture and element partitioning. Contrib Mineral Petrol 93:429–438
Krauskopf KB (1948) Lava movement at Paricutin volcano, Mexico. Geol Soc Am Bull 59:1267–1284
Kraynik AM (1988) Foam flows. Annu Rev Fluid Mec 20:325–357

Krieger IM, Dougherty TJ (1959) A mechanism for non-Newtonian flow in suspensions of rigid spheres. Trans Soc Rheol 3:137–152
Kushiro I, Yoder Jr H, Mysen B (1976) Viscosities of basalt and andesite melts at high pressures. J Geophys Res 81:6351–6356
Kushnir ARL, Martel C, Champallier R, Arbaret L (2017) In situ confirmation of permeability development in shearing bubble-bearing melts and implications for volcanic outgassing. Earth Planet Sci Lett 458:315–326
La Spina, Burton M, Vitturi MdM (2015) Temperature evolution during magma ascent in basaltic effusive eruptions: A numerical application to Stromboli volcano. Earth Planet Sci Lett 426:89–100
La Spina, Burton M, Vitturi MdM, Arzilli F (2016) Role of syn-eruptive plagioclase disequilibrium crystallization in basaltic magma ascent dynamics. Nat Commun 7:13402
Lange RA, Cashman KV, Navrotsky A (1994) Direct measurements of latent heat during crystallization and melting of a ugandite and an olivine basalt. Contrib Mineral Petrol 118:169–181
Lavallée Y, Hess K-U, Cordonnier B, Bruce Dingwell D (2007) Non-Newtonian rheological law for highly crystalline dome lavas. Geology 35:843–846
Lavallée Y, Meredith P, Dingwell D, Hess K-U, Wassermann J, Cordonnier B, Gerik A, Kruhl J (2008) Seismogenic lavas and explosive eruption forecasting. Nature 453:507–510
Lavallée Y, Benson PM, Heap MJ, Hess K-U, Flaws A, Schillinger B, Meredith PG, Dingwell DB (2013) Reconstructing magma failure and the degassing network of dome-building eruptions. Geology 41:515–518
Lavallée Y, Varley N, Alatorre-Ibargüengoitia M, Hess K-U, Kueppers U, Mueller S, Richard D, Scheu B, Spieler O, Dingwell D (2012) Magmatic architecture of dome-building eruptions at Volcán de Colima, Mexico. Bull Volcanol 74:249–260
Lavallée Y, Cai B, Kendrick JE, Dobson K, Von Aulock FW, Kaus B, Godinho J, Atwood R, Courtois L, Azeem M, Holness M, Lee DP (2019) Illuminating shear-induced vesiculation in magma via synchrotron imaging. IUGG 2019, Montreal.
Lavallée Y, Kendrick JE (2022) Strain localization in magmas. Rev Mineral Geochem 87:721-765
Lejeune A, Bottinga Y, Trull T, Richet P (1999) Rheology of bubble-bearing magmas. Earth Planet Sci Lett 166:71–84
Lejeune AM, Richet P (1995) Rheology of crystal-bearing silicate melts: An experimental study at high viscosities. J Geophys Res: Solid Earth 100:4215–4229
Lenk R (1967) A generalized flow theory. J Appl Polym Sci 11:1033–1042
Lev E, Spiegelman M, Wysocki RJ, Karson JA (2012) Investigating lava flow rheology using video analysis and numerical flow models. J Volcanol Geotherm Res 247–248:62–73
Li J, Uhlmann DR (1970) The flow of glass at high stress levels: I. Non-Newtonian behavior of homogeneous 0.08 $Rb_2O\cdot$ 0.92 SiO_2 glasses. J Non-Cryst Solids 3:127–147
Liebske C, Behrens H, Holtz F, Lange RA (2003) The influence of pressure and composition on the viscosity of andesitic melts. Geochim Cosmochim Acta 67:473–485
Liu Z, Pandelaers L, Blanpain B, Guo M (2017) Viscosity of heterogeneous silicate melts: assessment of the measured data and modeling. ISIJ Inter 57:1895–1901
Llewellin E, Manga M (2005) Bubble suspension rheology and implications for conduit flow. J Volcanol Geotherm Res 143:205–217
Llewellin E, Mader H, Wilson S (2002a) The constitutive equation and flow dynamics of bubbly magmas. Geophys Res Lett 29:23-21–23-24
Llewellin E, Mader H, Wilson S (2002b) The rheology of a bubbly liquid. Proc R Soc London. Ser A 458:987–1016
Loewenberg M, Hinch E (1996) Numerical simulation of a concentrated emulsion in shear flow. J Fluid Mech 321:395–419
Lofgren G (1980) Experimental studies on the dynamic crystallization of silicate melts. Phys Magmatic Process 487:551
Long PE, Wood BJ (1986) Structures, textures, and cooling histories of Columbia River basalt flows. Geol Soc Am Bull 97:1144–1155
Mackenzie J (1950) The elastic constants of a solid containing spherical holes. Proc Phys Soc Sec B 63:2–11
Mackenzie J (1956) Simultaneous measurements of density, viscosity, and electric conductivity of melts. Rev Sci Instrum 27:297–299
Mader HM, Llewellin EW, Mueller SP (2013) The rheology of two-phase magmas: A review and analysis. J Volcanol Geotherm Res 257:135–158
Madonna C, Quintal B, Frehner M, Almqvist BSG, Tisato N, Pistone M, Marone F, Saenger EH (2013) Synchrotron-based X-ray tomographic microscopy for rock physics investigations: Synchrotron-based rock images. Geophysics 78:D53-D64
Mandler BE, Elkins–Tanton LT (2013) The origin of eucrites, diogenites, and olivine diogenites: Magma ocean crystallization and shallow magma chamber processes on Vesta. Meteorit Planet Sci 48:2333–2349
Manga M, Loewenberg M (2001) Viscosity of magmas containing highly deformable bubbles. J Volcanol Geotherm Res 105:19–24
Manga M, Castro J, Cashman KV, Loewenberg M (1998) Rheology of bubble-bearing magmas. J Volcanol Geotherm Res 87:15–28
Mangan M, Sisson T (2005) Evolution of melt–vapor surface tension in silicic volcanic systems: Experiments with hydrous melts. J Geophys Res: Solid Earth 110:B01202
Markl G, Marks MA, Frost BR (2010) On the controls of oxygen fugacity in the generation and crystallization of peralkaline melts. J Petrol 51:1831–1847

Maron SH, Levy-Pascal AE (1955) Rheology of synthetic latex: VI. The flow behavior of neoprene latex. J Colloid Sci 10:494–503
Maron SH, Pierce PE (1956) Application of Ree–Eyring generalized flow theory to suspensions of spherical particles. J Colloid Sci 11:80–95
Marsh B (1981) On the crystallinity, probability of occurrence, and rheology of lava and magma. Contrib Mineral Petrol 78:85–98
McBirney AR, Murase T (1984) Rheological properties of magmas. Ann Rev Earth Planet Sci 12:337–357
McIntosh IM, Llewellin EW, Humphreys MCS, Nichols ARL, Burgisser A, Schipper CI, Larsen JF (2014) Distribution of dissolved water in magmatic glass records growth and resorption of bubbles. Earth Planet Sci Lett 401:1–11
Moitra P, Gonnermann HM (2015) Effects of crystal shape- and size-modality on magma rheology. Geomchem Geophys Geosyst16:1–26
Moore H (1987) Preliminary estimates of the rheological properties of 1984 Mauna Loa lava. US Geol Surv Prof Pap 1350:1569–1588
Moore H, Arthur D, Schaber G (1978) Yield strengths of flows on the Earth, Mars, and Moon. Lunar Planet Sci Conf 9:3351–3378
Morgavi D, Petrelli M, Vetere F, González-García D, Perugini D (2015) High-temperature apparatus for chaotic mixing of natural silicate melts. Rev Sci Instrum 86:105108
Morrison AA, Whittington A, Smets B, Kervyn M, Sehlke A (2020) The Rheology of Crystallizing basaltic lavas from Nyiragongo and Nyamuragira volcanoes, DRC. Volcanica 3:1–28
Mueller S, Llewellin EW, Mader HM (2010) The rheology of suspensions of solid particles. Proceedings of the Royal Society A: Mathematical, Phys Eng Sci 466:1201–1228
Mueller S, Llewellin EW, Mader HM (2011) The effect of particle shape on suspension viscosity and implications for magmatic flows. Geophys Res Lett 38:L13316
Mujin M, Nakamura M (2014) A nanolite record of eruption style transition. Geology 42:611–614
Mujin M, Nakamura M, Miyake A (2017) Eruption style and crystal size distributions: Crystallization of groundmass nanolites in the 2011 Shinmoedake eruption. Am Mineral 102:2367–2380
Murase T, Mc Birney AR (1973) Properties of some common igneous rocks and their melts at high temperatures. Geol Soc Am Bull 84:3563–3592
Murase T, McBirney AR, Melson WG (1985) Viscosity of the dome of Mount St. Helens. J Volcanol Geotherm Res 24:193–204
Mysen BO, Virgo D (1978) Influence of pressure, temperature, and bulk composition on melt structures in the system $NaAlSi_2O_6$–$NaFe^{3+}Si_2O_6$. Am J Sci 278:1307–1322
Mysen BO, Virgo D, Seifert FA (1984) Redox equilibria of iron in alkaline earth silicate melts; relationships between melt structure, oxygen fugacity, temperature and properties of iron-bearing silicate liquids. Am Mineral 69:834–847
Nichols RL (1939) Viscosity of lava. J Geol 47:290–302
Nicolas A, Ildefonse B (1996) Flow mechanism and viscosity in basaltic magma chambers. Geophys Res Lett 23:2013–2016
Ohtani E, Suzuki A, Ando R, Urakawa S, Funakoshi K, Katayama Y (2005) Viscosity and density measurements of melts and glasses at high pressure and temperature by using the multi-anvil apparatus and synchrotron X-ray radiation. *In*: Advances in High-Pressure Technology for Geophysical Applications. Elsevier, p 195–209
Okumura S, Nakamura M, Nakano T, Uesugi K, Tsuchiyama A (2010) Shear deformation experiments on vesicular rhyolite: Implications for brittle fracturing, degassing, and compaction of magmas in volcanic conduits. J Geophys Res: Solid Earth 115:B06201
Okumura S, Nakamura M, Uesugi K, Nakano T, Fujioka T (2013) Coupled effect of magma degassing and rheology on silicic volcanism. Earth Planet Sci Lett 362:163–170
Okumura S, Kushnir ARL, Martel C, Champallier R, Thibault Q, Takeuchi S (2016) Rheology of crystal-bearing natural magmas: Torsional deformation experiments at 800 °C and 100MPa. J Volcanol Geotherm Res 328:237–246
Oldroyd J (1953) The elastic and viscous properties of emulsions and suspensions. Proc R Soc London Ser A Math Phys Sci 218:122–132
Oosterbroek M, Mellema J (1981) Linear viscoelasticity of emulsions: I. The effect of an interfacial film on the dynamic viscosity of nondilute emulsions. J Colloid Interfac Sci 84:14–26
Pal R (2003) Rheological behavior of bubble-bearing magmas. Earth Planet Sci Lett 207:165–179
Panov VK, Slezin YB, Storcheus AV (1988) Mechanical properties of lava extruded in the 1983 Predskazanny eruption (Klyuchevskoi volcano). J Volcanol Seismol 7:25–37
Papale P (1999) Strain-induced magma fragmentation in explosive eruptions. Nature 397:425–428
Paterson MS, Olgaard DL (2000) Rock deformation tests to large shear strains in torsion. J Structur Geol 22:1341–1358
Petford N (2003) Rheology of granitic magmas during ascent and emplacement. Annu Rev Earth Planet Sci 31:399–427
Petford N (2009) Which effective viscosity? Mineral Mag 73:167–191
Phan-Thien N, Pham D (1997) Differential multiphase models for polydispersed suspensions and particulate solids. J Non-Newtonian Fluid Mech 72:305–318
Philpotts AR, Carroll M (1996) Physical properties of partly melted tholeiitic basalt. Geology 24:1029–1032
Pichavant M, Brugier Y, Di Muro A (2016) Petrological and experimental constraints on the evolution of Piton de la Fournaise magmas. *In:* Active Volcanoes of the Southwest Indian Ocean. Springer, p 171–184

Pinkerton H (1994) Rheological and related properties of lavas. Etna: Magma and lava flow modeling and volcanic system definition aimed at hazard assessment:76–89
Pinkerton H, Sparks RSJ (1978) Field measurements of the rheology of lava. Nature 276:383–385
Pinkerton H, Stevenson RJ (1992) Methods of determining the rheological properties of magmas at sub-liquidus temperatures. J Volcanol Geotherm Res 53:47–66
Pinkerton H, Norton G (1995) Rheological properties of basaltic lavas at sub-liquidus temperatures: laboratory and field measurements on lavas from Mount Etna. J Volcanol Geotherm Res 68:307–323
Pinkerton H, Norton G, Dawson J, Pyle D (1995a) Field observations and measurements of the physical properties of Oldoinyo Lengai alkali carbonatite lavas, November 1988. *In:* Carbonatite Volcanism. Springer, p 23–36
Pinkerton H, Herd R, Kent R, Wilson L (1995b) Field measurements of the rheological properties of basaltic lavas. Lunar Planet Sci Conf Vol 26
Pistone M (2012) Physical Properties of Crystal- and Bubble -Bearing Magmas. PhD ETH Zuerich, Zuerich
Pistone M, Cordonnier B, Ulmer P, Caricchi L (2016) Rheological flow laws for multiphase magmas: An empirical approach. J Volcanol Geotherm Res 321:158–170
Pistone M, Whittington AG, Andrews B, Cottrell E (2017) Crystal-rich lava dome extrusion during vesiculation: An experimental study. J Volcanol Geotherm Res 347:1–4
Pistone M, Caricchi L, Ulmer P, Reusser E, Ardia P (2013) Rheology of volatile-bearing crystal mushes: mobilization vs. viscous death. Chem Geol 345:16–39
Pistone M, Caricchi L, Ulmer P, Burlini L, Ardia P, Reusser E, Marone F, Arbaret L (2012) Deformation experiments of bubble- and crystal-bearing magmas: Rheological and microstructural analysis. J Geophys Res: Solid Earth (1978–2012) 117:B05208
Pistone M, Arzilli F, Dobson KJ, Cordonnier B, Reusser E, Ulmer P, Marone F, Whittington AG, Mancini L, Fife JL (2015) Gas-driven filter pressing in magmas: Insights into in-situ melt segregation from crystal mushes. Geology 43:699–702
Pleše P, Higgins M, Mancini L, Lanzafame G, Brun F, Fife J, Casselman J, Baker D (2018) Dynamic observations of vesiculation reveal the role of silicate crystals in bubble nucleation and growth in andesitic magmas. Lithos 296:532–546
Polacci M, Mancini L, Baker DR (2010) The contribution of synchrotron X-ray computed microtomography to understanding volcanic processes. J Synchrotron Radiat 17:215–221
Polacci M, Arzilli F, La Spina G, et al. (2018) Crystallisation in basaltic magmas revealed via in situ 4D synchrotron X-ray microtomography. Sci Rep 8:8377
Quane SL, Russell JK (2005) Welding; insights from high-temperature analogue experiments. J Volcanol Geotherm Res 142:67–87
Quane SL, Russell JK (2006) Bulk and particle strain analysis in high-temperature deformation experiments. J Volcanol Geotherm Res 154:63–73
Quane SL, Russell JKR, Kennedy L (2004) A low-load, high-temperature deformation apparatus for volcanological studies. Am Mineral 89:873–877
Quane SL, Russell JK, Friedlander EA (2009) Time scales of compaction in volcanic systems. Geology 37:471–474
Rahaman MN, De Jonghe LC, Scherer GW, Brook RJ (1987) Creep and densification during sintering of glass powder compacts. J Am Ceram Soc 70:766–774
Raterron P, Merkel S (2009) In situ rheological measurements at extreme pressure and temperature using synchrotron X-ray diffraction and radiography. J Synchrotron Radiat 16:748–756
Rhéty M, Harris A, Villeneuve N, Gurioli L, Médard E, Chevrel O, Bachélery P (2017) A comparison of cooling- and volume-limited flow systems: Examples from channels in the Piton de la Fournaise April 2007 lava flow field. Geomchem Geophys Geosyst 18:3270–3291
Robert G, Russell JK, Giordano D, Romano C (2008) High-temperature deformation of volcanic materials in the presence of water. Am Min 93:74–80
Roeder PL, Dixon JM (1977) A centrifuge furnace for separating phases at high temperature in experimental petrology. Can J Earth Sci 14:1077–1084
Roscoe R (1952) The viscosity of suspensions of rigid spheres. Br J Appl Phys 3:267
Rose WI (1973) Pattern and mechanism of volcanic activity at the Santiaguito volcanic dome, Guatemala. Bull Volcanol 37:73
Rowlatt MA (1956) Compression plastimeter. United States patent US 2,754,675
Rudyak VY (2013) Viscosity of nanofluids. Why it is not described by the classical theories. Adv Nanoparticles 2:266
Rusiecka MK, Bilodeau M, Baker DR (2020) Quantification of nucleation delay in magmatic systems: experimental and theoretical approach. Contrib Mineral Petrol 175:47
Russell JK, Quane SL (2005) Rheology of welding; inversion of field constraints. J Volcanol Geotherm Res 142:173–191
Russell JK, Hess K-U, Dingwell DB (2022) Models for viscosity of geological melts. Rev Mineral Geochem 87:841-885
Rust AC, Manga M (2002) Effects of bubble deformation on the viscosity of dilute suspensions. J Non-Newtonian Fluid Mech 104:53–63
Rutter EH, Brodie KH, Irving DH (2006) Flow of synthetic, wet, partially molten "granite" under undrained conditions: An experimental study. J Geophys Res: Solid Earth 111
Ryan A, Russell J, Heap M, Kolzenburg S, Vona A, Kushnir A (2019a) Strain-dependent rheology of silicate melt foams: importance for outgassing of silicic lavas. J Geophys Res: Solid Earth 124:8167–8186

Ryan AG, Russell JK, Nichols AR, Hess K-U, Porritt LA (2015) Experiments and models on H_2O retrograde solubility in volcanic systems. Am Mineral 100:774–786
Ryan AG, Kolzenburg S, Vona A, Heap MJ, Russell JK, Badger S (2019b) A proxy for magmatic foams: FOAMGLAS®, a closed-cell glass insulation. J Non-Cryst Solids: X 1:100001
Ryerson F, Weed H, Piwinskii A (1988) Rheology of subliquidus magmas: 1. Picritic compositions. J Geophys Res: Solid Earth 93:3421–3436
Saar MO, Manga M, Cashman KV, Fremouw S (2001) Numerical models of the onset of yield strength in crystal–melt suspensions. Earth Planet Sci Lett 187:367–379
Sato H (2005) Viscosity measurement of subliquidus magmas:1707 basalt of Fuji volcano. J Mineral Petrol Sci 100:133–142
Sato M (1978) Oxygen fugacity of basaltic magmas and the role of gas-forming elements. Geophys Res Lett 5:447–449
Schowalter WR (1978) Mechanics of Non-Newtonian Fluid. Pergamon
Sehlke A, Whittington AG (2015) Rheology of lava flows on Mercury: An analog experimental study. J Geophys Res: Planets 120:1924–1955
Sehlke A, Whittington A, Robert B, Harris A, Gurioli L, Médard E (2014) Pahoehoe to `a`a transition of Hawaiian lavas: an experimental study. Bull Volcanol 76:1–20
Settle M (1979) Lava rheology: Thermal buffering produced by the latent heat of crystallization. Lunar Planet Sci Conf 10:1107–1109
Shapiro AP, Probstein RF (1992) Random packings of spheres and fluidity limits of monodisperse and bidisperse suspensions. Phys Rev Lett 68:1422
Sharp TG, Stevenson RJ, Dingwell DB (1996) Microlites and" nanolites" in rhyolitic glass: Microstructural and chemical characterization. Bull Volcanol 57:631–640
Shaw H, Wright T, Peck D, Okamura R (1968) The viscosity of basaltic magma; an analysis of field measurements in Makaopuhi lava lake, Hawaii. Am J Sci 266:225–264
Shaw HR (1965) Comments on viscosity, crystal settling, and convection in granitic magmas. Am J Sci 263:120–152
Shaw HR (1969) Rheology of basalt in the melting range. J Petrol 10:510–535
Shields JK, Mader HM, Pistone M, Caricchi L, Floess D, Putlitz B (2014) Strain-induced outgassing of three-phase magmas during simple shear. J Geophys Res: Solid Earth 119:6936–6957
Sibree J (1934) The viscosity of froth. Trans Faraday Soc 30:325–331
Sicola S, Vona A, Ryan AG, Russell JK, Romano C (2021) The effect of pores (fluid-filled vs. drained) on magma rheology. Chem Geol 569:120147
Soldati A, Sehlke A, Chigna G, Whittington A (2016) Field and experimental constraints on the rheology of arc basaltic lavas: the January 2014 Eruption of Pacaya (Guatemala). Bull Volcanol 78:1–19
Soldati A, Beem J, Gomez F, Huntley JW, Robertson T, Whittington A (2017) Emplacement dynamics and timescale of a Holocene flow from the Cima Volcanic Field (CA): Insights from rheology and morphology. J Volcanol Geotherm Res 347:91–111
Sonder I, Zimanowski B, Büttner R (2006) Non-newtonian viscosity of basaltic magma. Geophys Res Lett 33
Song S-R, Jones KW, Lindquist BW, Dowd BA, Sahagian DL (2001) Synchrotron X-ray computed microtomography: studies on vesiculated basaltic rocks. Bull Volcanol 63:252–263
Soule SA, Cashman KV (2005) Shear rate dependence of the pāhoehoe-to-ʻa ʻā transition: analog experiments. Geology 33:361–364
Sparks RSJ, Annen C, Blundy JD, Cashman KV, Rust AC, Jackson MD (2019) Formation and dynamics of magma reservoirs. Philos Trans R Soc A 377:20180019
Spera FJ, Borgia A, Strimple J, Feigenson M (1988) Rheology of melts and magmatic suspensions: 1. Design and calibration of concentric cylinder viscometer with application to rhyolitic magma. J Geophys Res: Solid Earth 93:10273–10294
Spina L, Cimarelli C, Scheu B, Di Genova D, Dingwell DB (2016) On the slow decompressive response of volatile- and crystal-bearing magmas: An analogue experimental investigation. Earth Planet Sci Lett 433:44–53
Stein DJ, Spera FJ (1992) Rheology and microstructure of magmatic emulsions: theory and experiments. J Volcanol Geotherm Res 49:157–174
Stein D, Spera F (1998) New high-temperature rotational rheometer for silicate melts, magmatic suspensions, and emulsions. Rev Sci Instrum 69:3398–3402
Stein DJ, Spera FJ (2002) Shear viscosity of rhyolite-vapor emulsions at magmatic temperatures by concentric cylinder rheometry. J Volcanol Geotherm Res 113:243–258
Stevenson RJ, Dingwell DB, Webb S, Bagdassarov N (1995) The equivalence of enthalpy and shear stress relaxation in rhyolitic obsidians and quantification of the liquid-glass transition in volcanic processes. J Volcanol GeothermRes 68:297–306
Stevenson RJ, Dingwell DB, Webb SL, Sharp TG (1996) Viscosity of microlite-bearing rhyolitic obsidians: an experimental study. Bull Volcanol 58:298–309
Stevenson RJ, Dingwell DB, Bagdassarov NS, Manley CR (2001) Measurement and implication of “effective” viscosity for rhyolite flow emplacement. Bull Volcanol 63:227–237
Stickel JJ, Powell RL (2005) Fluid mechanics and rheology of dense suspensions. Annu Rev Fluid Mech 37:129–149

Sumita I, Manga M (2008) Suspension rheology under oscillatory shear and its geophysical implications. Earth Planet Sci Lett 269:468–477
Swanson SE (1977) Relation of nucleation and crystal-growth rate to the development of granitic textures. Am Mineral 62:966–978
Taisne B, Jaupart C (2008) Magma degassing and intermittent lava dome growth. Geophys Res Lett 35
Takeuchi S, Nakashima S, Tomiya A (2008) Permeability measurements of natural and experimental volcanic materials with a simple permeameter: toward an understanding of magmatic degassing processes. J Volcanol Geotherm Res 177:329–339
Takeuchi S, Tomiya A, Shinohara H (2009) Degassing conditions for permeable silicic magmas: Implications from decompression experiments with constant rates. Earth Planet Sci Lett 283:101–110
Tammann G, Hesse W (1926) Die Abhängigkeit der Viscosität von der Temperatur bie unterkühlten Flüssigkeiten. Z Anorg Allg Chem 156:245–257
Taylor GI (1932) The viscosity of a fluid containing small drops of another fluid. Proc R Soc London Ser A 138:41–48
Taylor R, Coulombe S, Otanicar T, Phelan P, Gunawan A, Lv W, Rosengarten G, Prasher R, Tyagi H, (2013) Small particles, big impacts: A review of the diverse applications of nanofluids. J Appl Physics 113:1
Toplis M, Carroll M (1995) An experimental study of the influence of oxygen fugacity on Fe-Ti oxide stability, phase relations, and mineral—melt equilibria in ferro-basaltic systems. J Petrol 36:1137–1170
Torquato S (2013) Random Heterogeneous Materials: Microstructure and Macroscopic Properties. Springer Science and Business Media
Tripoli B, Manga M, Mayeux J, Barnard H (2019) The effects of deformation on the early crystallization kinetics of basaltic magmas. Front Earth Sci 7:250
Truby J, Mueller S, Llewellin E, Mader H (2015) The rheology of three-phase suspensions at low bubble capillary number. Proc R Soc A 471:20140557
Ulusay R, Hudson JA (2006) The complete ISRM suggested methods for rock characterization, testing and monitoring:1974–2006. The International Society for Rock Mechanics and Rock Engineering, Ankara, Turkey
Vand V (1948) Viscosity of solutions and suspensions. I. Theory. J Phys Chem 52:277–299
Vasseur J, Wadsworth FB, Lavallée Y, Bell AF, Main IG, Dingwell DB (2015) Heterogeneity: the key to failure forecasting. Sci Rep 5:13259
Vetere F, Sato H, Ishibashi H, De Rosa R, Donato P (2013) Viscosity changes during crystallization of a shoshonitic magma: new insights on lava flow emplacement. J Mineral Petrol Sci 108:144–160
Vetere F, Behrens H, Schuessler JA, Holtz F, Misiti V, Borchers L (2008) Viscosity of andesite melts and its implication for magma mixing prior to Unzen 1991–1995 eruption. J Volcanol Geotherm Res 175:208–217
Vetere F, Murri M, Alvaro M, Domeneghetti MC, Rossi S, Pisello A, Perugini D, Holtz F (2019) Viscosity of pyroxenite melt and its evolution during cooling. J Geophys Res: Planets 124:1451–1469
Vetere F, Iezzi G, Behrens H, Holtz F, Ventura G, Misiti V, Cavallo A, Mollo S, Dietrich M (2015) Glass forming ability and crystallisation behaviour of sub-alkaline silicate melts. Earth Sci Rev 150:25–44
Vetere F, Rossi S, Namur O, Morgavi D, Misiti V, Mancinelli P, Petrelli M, Pauselli C, Perugini D (2017) Experimental constraints on the rheology, eruption and emplacement dynamics of analog lavas comparable to Mercury's northern volcanic plains. J Geophys Res: Planets 122:1522–1538
Villeneuve N, Neuville DR, Boivin P, Bachèlery P, Richet P (2008) Magma crystallization and viscosity: a study of molten basalts from the Piton de la Fournaise volcano (La Réunion island). Chem Geol 256:242–251
Von Aulock FW, Kennedy BM, Maksimenko A, Wadsworth FB, Lavallée Y (2017) Outgassing from Open and Closed Magma Foams. Front Earth Sci 5:46
Vona A, Romano C (2013) The effects of undercooling and deformation rates on the crystallization kinetics of Stromboli and Etna basalts. Contrib Mineral Petrol 166:491–509
Vona A, Romano C, Dingwell DB, Giordano D (2011) The rheology of crystal-bearing basaltic magmas from Stromboli and Etna. Geochim Cosmochim Acta 75:3214–3236
Vona A, Ryan AG, Russell JK, Romano C (2016) Models for viscosity and shear localization in bubble-rich magmas. Earth Planet Sci Lett 449:26–38
Vona A, Di Piazza A, Nicotra E, Romano C, Viccaro M, Giordano G (2017) The complex rheology of megacryst-rich magmas: The case of the mugearitic "cicirara" lavas of Mt. Etna volcano. Chem Geol 458:48–67
Wadsworth FB, Vasseur J, Llewellin EW, Dingwell DB (2022) Hot sintering of melts, glasses and magmas. Rev Mineral Geochem 87:801-840
Walker D, Mullins O (1981) Surface tension of natural silicate melts from 1,200–1,500 C and implications for melt structure. Contrib Mineral Petrol 76:455–462
Walker D, Kirkpatrick R, Longhi J, Hays J (1976) Crystallization history of lunar picritic basalt sample 12002: phase-equilibria and cooling-rate studies. Geol Soc Am Bull 87:646–656
Walker G, Huntingdon A, Sanders A, Dinsdale J (1973) Lengths of lava flows [and discussion]. Phil Trans R Soc London A 74:107–118
Ward S, Whitmore R (1950) Studies of the viscosity and sedimentation of suspensions Part 1. The viscosity of suspension of spherical particles. Br J Appl Phys 1:286–290

Webb SL, Dingwell DB (1990a) Non-Newtonian rheology of igneous melts at high stresses and strain rates: experimental results for rhyolite, andesite, basalt, and nephelinite. J Geophys Res 95:15695–15701
Webb SL, Dingwell DB (1990b) The onset of non-Newtonian rheology of silicate melts. Phys Chem Mineral 17:125–132
Wildemuth C, Williams M (1984) Viscosity of suspensions modeled with a shear-dependent maximum packing fraction. Rheol Acta 23:627–635
Wildemuth C, Williams M (1985) A new interpretation of viscosity and yield stress in dense slurries: coal and other irregular particles. Rheol Acta 24:75–91
Wilson L, Head JW (1994) Mars: Review and analysis of volcanic eruption theory and relationships to observed landforms. Rev Geophys 32:221–263
Witter JB, Harris AJ (2007) Field measurements of heat loss from skylights and lava tube systems. J Geophys Res: Solid Earth (1978–2012) 112:B01203
Wright HMN, Weinberg RF (2009) Strain localization in vesicular magma: Implications for rheology and fragmentation. Geology 37:1023–1026
Zhou JZ, Uhlherr PH, Luo FT (1995) Yield stress and maximum packing fraction of concentrated suspensions. Rheol Acta 34:544–561